Comparative areal and modular architecture of the cerebral cortex

DISSERTATION

zur Erlangung des akademischen Grades

d o c t o r r e r u m n a t u r a l i u m

Dr. rer. nat.

im Fach Biologie

eingereicht an der

Mathematisch-Naturwissenschaftlichen Fakultät I

der Humboldt-Universität zu Berlin

von

Diplom-Biologe

Robert Konrad Naumann

Präsident der Humboldt-Universität zu Berlin

Prof. Dr. Jan-Hendrik Olbertz

Dekan der Mathematisch-Naturwissenschaftlichen Fakultät I

Prof. Stefan Hecht, PhD

Gutachter/innen:

1. Prof. Dr. Michael Brecht
2. Prof. Dr. Imre Vida
3. Prof. Dr. Dietmar Schmitz

Tag der mündlichen Prüfung: .....27.06.2014.....

Comparative areal and modular architecture of the cerebral cortex

Doctoral candidate:

Robert Konrad Naumann

Supervisor:

Prof. Dr. Michael Brecht

November 2013

Bernstein Center for Computational Neuroscience

Animal Physiology / Systems Neurobiology and Neural Computation

Humboldt University Berlin, Berlin, Germany

Contents

List of Figures

List of Tables

Chapter 1

General Introduction

1.1 Overview

Chapter 1 contains a brief outline of the structure of the mammalian cerebral cortex and an overview of different types of cortical modules. The entorhinal cortex is used as an example to illustrate principles of cortical organization. Chapter 2 reviews the behaviour and neurobiology of the Etruscan shrew and in Chapter 3 the cerebral cortex of the Etruscan shrew is studied using qualitative and quantitative anatomical techniques. Chapter 4 focuses on a group of principal cells in the entorhinal cortex of the rat that is organized in discrete cell clusters. These modules are studied in relation to cholinergic innervation and a functional correlate is suggested. Chapter 5 explores differences in spatial distribution of principal cell types in layer 2 of rat medial entorhinal cortex. Modular distribution of cholinergic input is contrasted with other modular structures in the medial entorhinal cortex and adjacent cortical regions. Chapter 6 concludes this thesis with a brief discussion of the main findings.

1.2 Cortical regions and areas

The cerebral cortex is the brain structure that changed most dramatically in the course of evolution. It expanded faster than all other brain regions and together with the overall trend towards increasing brain size led to the enormous cortical expansion in humans, elephants and whales. Fossil evidence indicates that ancestral mammals were probably small with little cerebral cortex and over time spread to more diverse ecological niches. But some mammals withstood the trend of general cortical enlargement and even decreased significantly in size from their evolutionary ancestor (Kaas, 2013). In Chapter 2 and 3 of this thesis I study the Etruscan shrew, Suncus etruscus, arguably the smallest

mammal with a body weight of ≈ 2 g, a body length of ≈ 35 mm (Merritt, 2010) and one of the smallest mammalian brains with a brain weight of only 60 mg. The size range of mammals spans eight orders of magnitude, from 2 g to 200 tonnes of the blue whale. Mammals have large brain to body weight ratios and this also holds for the Etruscan shrew. However, maintaining a large brain incurs a metabolic cost and in Chapter 2 we review how metabolic demands impact the behavior and neural structure in the Etruscan shrew.

The defining structural characteristic of the cortex is its subdivision into layers. The general layout consists of a single pyramidal cell layer, a layer of diverse and scattered interneurons and a largely acellular input layer. This structure is preserved in the hippocampus but elaborated into six layers in the mammalian isocortex (Brodmann, 1909). Overall, cortical thickness varies only seven-fold from the Etruscan shrew to man (Nieuwenhuys et al., 1998) and most of the 100.000-fold difference in size is due the expansion of cortical surface area. The cortical sheet is not homogeneous but subdivided into regions areas, the "organs of the brain" (Brodmann, 1909). The cerebral cortex can be roughly subdivided into a lateral olfactory region, a medial region related to spatial navigation, learning and memory, and a dorsal region responding to sensory inputs such as visual stimulation. The lateral, medial and dorsal regions are recognized as homologous in reptiles, birds and mammals, yet possibly, the ancestry of the cerebral cortex can be traced back even further (Tomer et al., 2010). The lateral region, the paleocortex, and the medial region, the archicortex, are collectively referred to as allocortex. The remaining cortex can now be thought of as forming concentric layers around the allocortex towards a central dorsal cap - the isocortex (Sanides, 1970). Thus, the most simple classification recognizes only two types of cortical structures, isocortex and allocortex as shown in Fig. 1. However, due to the large differences in laminar structure between e.g. entorhinal cortex and hippocampus, periallocortex and proisocortex are often designated as an intermediate type of cortex or mesocortex (Filimonoff, 1947; Stephan, 1975).

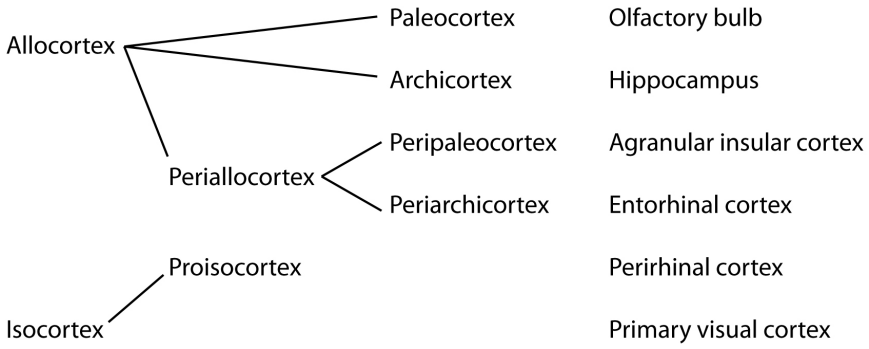

FIGURE 1.1: Hierarchical organization of the cerebral cortex.

Different methods have been developed to distinguish cortical rergions and areas. Classic cytoarchitectonic localisation is based on differences in histological appearance of cellular elements, laminar structure and topographic arrangement (Brodmann, 1909; Krieg, 1946). Together with experiments based on electrical stimulation, lesions, responses to sensory stimuli and afferent connections a consensus about the localisation of a few major areas has emerged (Fritzsch & Hitzig, 1870; Munk, 1881; Rose & Woolsey, 1949; Blackstad, 1956). Still, there are few anatomical markers identifying areas beyond the primary sensory regions and maps obtained using electrophysiological methods depend strongly on the type of mapping procedure adopted (Graziano, 2006; Brecht, 2011). Recent experiments challenged the classical view that larger brains have considerably more cortical areas and proposed that large numbers of areas emerge early in evolution (Wang & Burkhalter, 2007). Comparative studies of the largest and the smallest mammalian brains may allow to answer these questions. Thus, in Chapter 3 we investigate the regional and areal structure of the Etruscan shrew cerebral cortex.

1.3 Entorhinal cortex

Here, we give an overview of the subdivisions of the parahippocampal region. Chapters 4 and 5 provide a more detailed anatomical description of these areas and attempt to relate cortical function to cellular architecture. Figure 1.2A shows the location of the entorhinal cortex (MEC - medial entorhinal cortex, LEC - lateral entorhinal cortex) in a caudal view of the left hemisphere of a rat brain. Entorhinal, perirhinal (Per) and postrhinal cortex (Por) combined form the parahippocampal region (Burwell, 2000). Most investigations of the rodent entorhinal region have used sagittal (Fig. 1.2B) or horizontal (Fig. 1.2C) sections. The sections in Fig. 1.2B and 1.2C were stained for acetylcholinesterase activity which reveals chemoarchitectonic characteristics of the entorhinal cortex and neighbouring regions (Mathisen & Blackstad 1964). In brief, medial entorhinal cortex can be defined by its lattice-like staining for acetylcholinesterase activity in layer 3 as opposed to the more homogeneous staining pattern seen across superficial layers in lateral entorhinal cortex. Also, variably sized islands of acetylcholinesterase staining are present in layer 2 of medial entorhinal cortex (black arrows in Figs. 1.2B, 1.2C). The parasubiculum (PaS) and presubiculum (PrS) are part of the retrohippocampal region (Köhler, 1986). They enclose a triangular region marked by an asterisk (Fig. 1C) which has been variably classified (Blackstad, 56; Haug, 1973; Honda & Ishizuka, 2004; Wang & Burkhalter 2007; Ding, 2013). To better understand the topography of modular structures in the entorhinal cortex we use tangential sections of the entorhinal region as shown in (Fig. 1.2D). A section through layer 3 of medial entorhinal cortex cut from the tangential preparation in Figure 1.2D is shown in Figure 1.2E. This section was stained

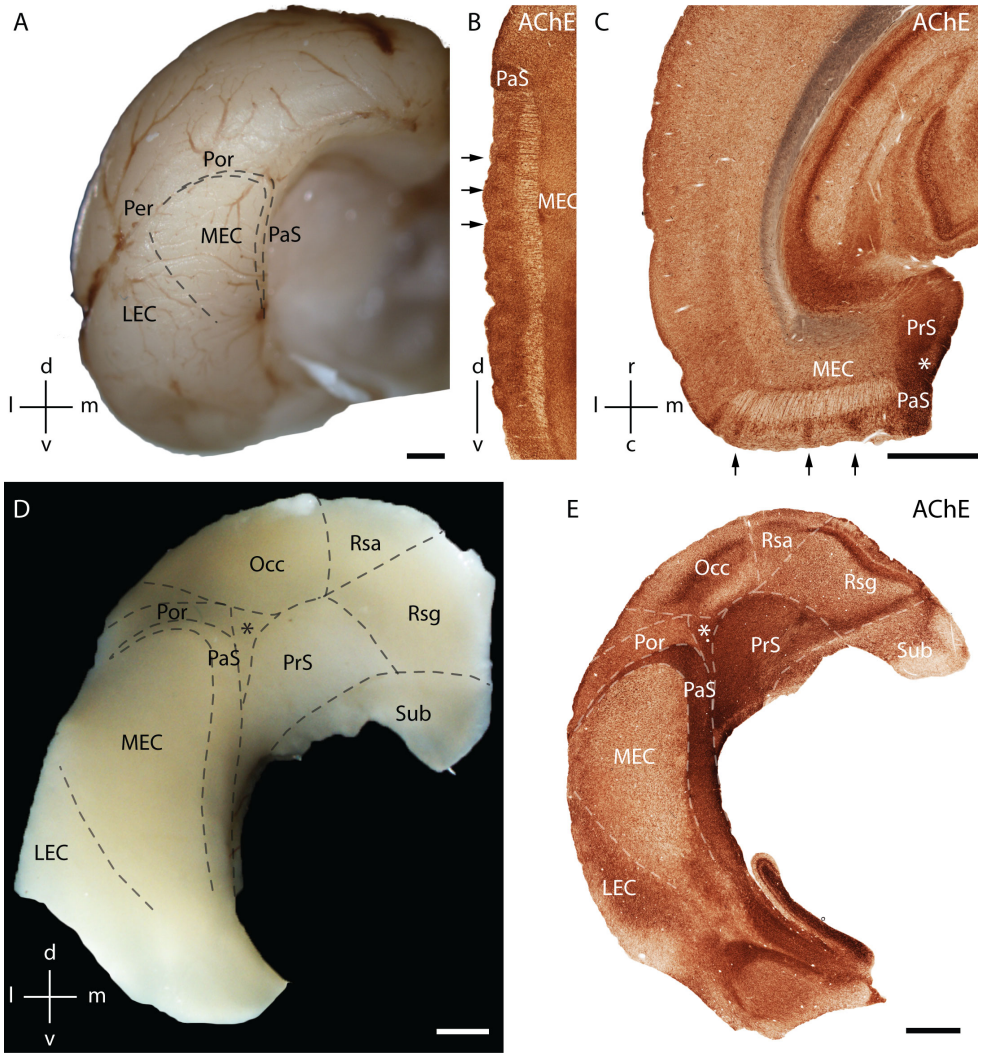

FIGURE 1.2: An overview of the rat parahippocampal region in sagittal, horizontal and tangential sections. A, Posterior view of the left cortical hemisphere of a rat brain with medial entorhinal cortex (MEC), lateral entorhinal cortex (LEC), parasubiculum (PaS), perirhinal cortex (Per) and postrhinal cortex (Por) indicated. B, Caudal part of a sagittal section stained for acetylcholinesterase activity. Almost the entire dorso-ventral length of this section is taken up by medial entorhinal cortex with parasubiculum and posthinal cortex dorsal to medial entorhinal cortex. Medial entorhinal cortex is characterized by palisade-like staining in layer 3 and increased staining activity in modules in layer 1/2. C, Caudal part of a horizontal section stained for acetylcholinesterase activity. Medial entorhinal cortex is defined as in B. Medial to the medial entorhinal cortex are the parasubiculum, the triangular region (asterisk) and the presubiculum (PrS). D, Brain slice prepared by a tangential cut through entorhinal cortex and adjacent regions, unfolded and flattened. Entorhinal cortex and presubiculum are myelin dense compared with neighboring areas and therefore reflect more light in unstained tangential sections. Surrounding the presubiculum are the subiculum (Sub), retrosplenial granular cortex (Rsg), retrosplenial agranular cortex (Rsa), occipital cortex (Occ). E, Tangential section through the brain slice shown in D. In the medial entorhinal cortex the section passes through layer 3, largely parallel to the surface. In retrosplenial and occipital cortex the section passes through several layers highlighting areal differences. Scale bars: A = 1 mm; C = 1 mm (also for B); D, E = 1 mm. d = dorsal, l = lateral, m = medial, v = ventral, r = rostral, c = caudal. For abbreviations see Table 5.1.

for acetylcholinesterase activity and reveals clear architectonic borders of several cortical areas (Eckenstein et al., 1988). The lattice-like arrangement of acetylcholinesterase positive fibres seen in sagittal or horizontal sections (Figs. 1.2B, 1.2C) in layer 3 of medial entorhinal cortex appears as an array of dots in tangential sections (Fig. 1.2E). This allows for an easy delineation of the medial entorhinal area against the lateral entorhinal area and the parasubiculum.

1.4 Modular structure of the cerebral cortex

Cortical areas have been subdivided into smaller subunits called minicolumns, columns, patches, blobs, domains or modules (Kaas, 2012). In the most general sense, modules can be defined as a set of structural features that repeats in a more or less regular fashion in a plane parallel to the surface of the cortex. Modules are not necessarily cylindrical in shape but can also take the form of bands or stripes and they are present in variable sizes from 30 um to more than 1 mm (smallest diameter). Modular structures have been found in many different cortical areas and in almost all cortical layers; but also in other regions of the mammalian (Roney et al., 1979) and non-mammalian brain (Leise, 1990). A general feature of modules is that they scale allometrically with brain size or cortex size. While mammalian brain size varies by a factor of 100.000 (Nieuwenhuys et al., 1998), module size varies at most by a factor of about 10 (Manger et al., 1998). Modular anatomical structures may be formed during cortical development, they can be recognized by dendritic bundling or cellular clustering or they may be imposed upon cortical architecture by topographic or overlapping afferents. In the following paragraphs we describe a few examples of modular structures and possible functional correlates.

The smallest modules are 30 - 50 um wide vertical cell columns (von Economo & Koskinas, 1925; Jones, 2000; Buxhoeveden & Casanova, 2002). Such columns may be a reflection of the radial migration of clonally related excitatory cells in cortical development (Kornack & Rakic, 1995). These clonally related cells are preferentially connected (Yu et al., 2009; Yu et al., 2012) and have similar sensory response properties (Li et al., 2012; Ohtsuki et al., 2012). Also, neurons are more densely connected vertically across layers than horizontally within layers (Lund & Boothe, 1975). Together, these results may form the basis for the similarity of response properties encountered in vertical electrode penetrations through the cerebral cortex (Mountcastle, 1957; Hubel & Wiesel, 1962; Mountcastle, 2003).

Dendritic bundles are prominent elements of the neuropil in between the cellular columns (Fleischhauer et al., 1972; Peters & Walsh, 1972). The spacing of dendritic bundles is about 40-50 um, similar to the cell columns, however any individual dendrite may overlap

with several cell columns. Thus, dendritic bundling allows for an alternative definition of minicolumns: all neurons contributing to the dendritic bundle are considered an anatomical unit. The dendrites of groups of neurons in layer 5 bundle together and ascend through layer 4 where they may be joined by dendrites of layer 2 and 3 neurons (Peters, 2010). So far, there is no evidence for increased connectivity or more common synaptic input among layer 5 neurons contributing to a dendritic bundle (Krieger et al., 2007). Dendritic bundling is also widespread in layer 2 pyramidal cells (Rockland & Ichinhohe, 2004). Consequently, inputs to layer 1 and 2 often segregate and target specific sets of dendritic bundles. For example, in rat visual cortex, thalamic and cortico-cortical afferents form an interdigitating set of terminations at the layer 1/2 border (Ichinohe et al., 2003).

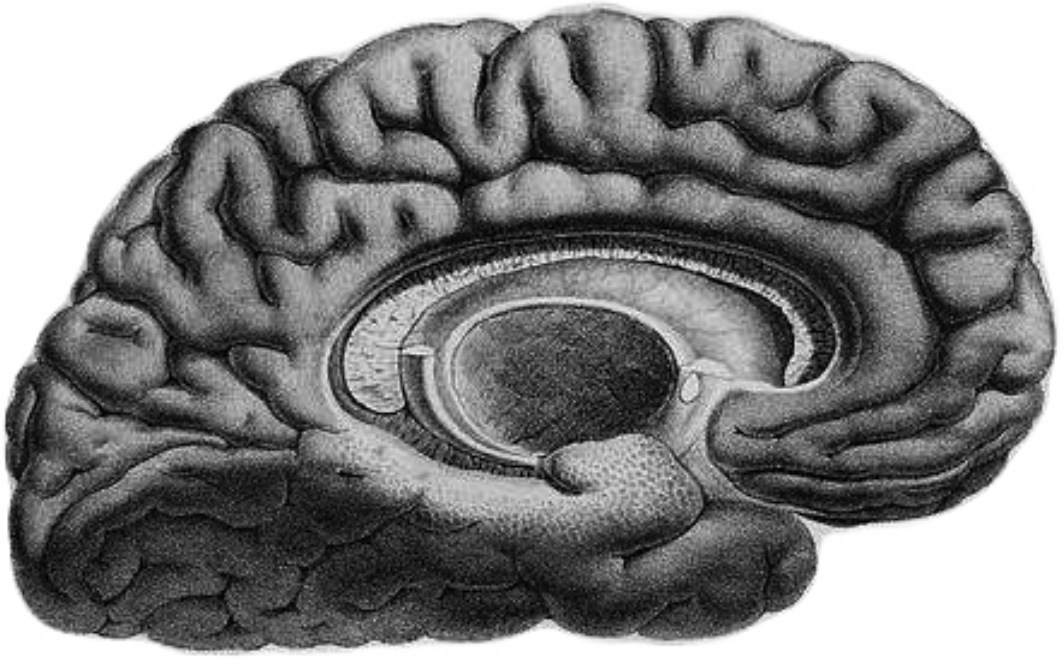

FIGURE 1.3: The white reticular substance of Arnold in the medial aspect of the human temporal lobe. Adapted from Arnold (1838).

Body surfaces are represented topographically in the brain. In cases where the body surface is segregated into adjacent elements such as the fingers of the hand or the nose appendages of the star-nosed mole, these are visible as modular elements in the cerebral cortex (Catania et al., 1993; Jain et al., 1998), thalamus (Liao et al., 2013) and brainstem (Catania et al., 2011). The most famous example for this type of modules is the barrel cortex of rodents (Woolsey and Van der Loos, 1970; Lorente de No, 1992). This clear structure/function relationship has made the barrel cortex an elegant model for studying

layer specific functional properties (Brecht & Sakmann, 2002) and quantitative anatomy (Meyer et al., 2010).

The types of columns described above all have definite anatomical boundaries yet orientation preference maps in visual cortex show a nearly continuous mapping of stimulus properties across the cortical surface (Kaas, 2012; Kaschube et al., 2010). A possible anatomical basis for this type of module, first described in the entorhinal cortex, may be afferent fibers that ramify in the form of overlapping, vertical cylinders in the cortex (Lorente de No, 1933).

1.5 Modular structures in the entorhinal cortex

Probably the first type of modular structure was described in freshly dissected human brains in the temporal lobe. The medial part of this lobe shows a distinct surface structure - the white reticular substance of Arnold (Fig. 1.3; Arnold, 1838) and in between, prominent elevations visible to the naked eye termed "verrucae" (Retzius, 1896). These features correspond to a network of myelinated fibers and cellular islands in the entorhinal cortex and presubiculum (Klingler, 1948). While the modular structure of the primate and human entorhinal region has been studied in great detail (Braak, 1972; Beall & Lewis, 1992; Hevner & Wong-Riley, 1992; Solodkin & van Hoesen, 1996; Mikkonen et al, 1997; van Hoesen et al, 2000; Suzuki & Porteros, 2002), much less is known about rodent entorhinal modular architecture (Mathisen & Blackstad, 1964; Slomianka, 1992; Fujimaru & Kosaka, 1996; Witter & Moser, 2006). Thus, in Chapters 4 and 5 we study the modular structure of medial entorhinal cortex and try to interrelate different types of modules.

1.6 References

Arnold, Friedrich. 1838. Tabulae anatomicae: quas ad naturam accurate descriptas in lucem edidit (Band 1): Icones cerebri et medullae spinalis: decem tabulae elaboratae et totidem adumbratae. Orell, Fuesslin. Zürich, 1838. Digital version provided by: Universitätsbibliothek Heidelberg.
http://digi.ub.uni-heidelberg.de/diglit/arnold1838bd1?
sid=f706797cdf382a2ae8eb30f3ad72f923

Beall, M. J., & Lewis, D. A. (1992). Heterogeneity of layer II neurons in human entorhinal cortex. Journal of Comparative Neurology, 321(2), 241-266.

Blackstad, T. W. (1956). Commissural connections of the hippocampal region in the rat, with special reference to their mode of termination. Journal of Comparative Neurology, 105(3), 417-537.

Braak, H. (1972). Zur Pigmentarchitektonik der Grohirnrinde des Menschen. Zeitschrift für Zellforschung und Mikroskopische Anatomie, 127(3), 407-438.

Brecht, M. (2011). Movement, confusion, and orienting in frontal cortices. Neuron, 72(2), 193-196.

Brecht, M., & Sakmann, B. (2002). Dynamic representation of whisker deflection by synaptic potentials in spiny stellate and pyramidal cells in the barrels and septa of layer 4 rat somatosensory cortex. The Journal of physiology, 543(1), 49-70.

Brodmann, K. (1909). Vergleichende Lokalisationslehre der Grosshirnrinde: in ihren Prinzipien dargestellt auf Grund des Zellenbaues. Ja Barth.

Burwell, R. D. (2000). The parahippocampal region: corticocortical connectivity. Annals of the New York Academy of Sciences, 911(1), 25-42.

Buxhoeveden, D. P., & Casanova, M. F. (2002). The minicolumn hypothesis in neuroscience. Brain, 125(5), 935-951.

Catania, K. C., Leitch, D. B., & Gauthier, D. (2011). A star in the brainstem reveals the first step of cortical magnification. PloS one, 6(7), e22406.

Catania, K. C., Northcutt, R. G., Kaas, J. H., & Beck, P. D. (1993). Nose stars and brain stripes. Nature, 364(6437), 493.

Ding, S. L. (2013). Comparative anatomy of the prosubiculum, subiculum, presubiculum, postsubiculum, and parasubiculum in human, monkey, and rodent. Journal of Comparative Neurology, 521(18), 4145-4162.

Eckenstein, F. P., Baughman, R. W., & Quinn, J. (1988). An anatomical study of cholinergic innervation in rat cerebral cortex. Neuroscience, 25(2), 457-474.

Filimonoff, I. N. (1947). A rational subdivision of the cerebral cortex. Archives of neurology and psychiatry, 58(3), 296-311.

Fleischhauer, K., Petsche, H., & Wittkowski, W. (1972). Vertical bundles of dendrites in the neocortex. Zeitschrift für Anatomie und Entwicklungsgeschichte, 136(2), 213-223.

Fritsch, G., & Hitzig, E. (1870). Ueber die elektrische Erregbarkeit des Grosshirns. Arch. Anat. Physiol, 300-332.

Fujimaru, Y. & Kosaka, T. 1996 The distribution of two calcium binding proteins, calbindin D-28K and parvalbumin, in the entorhinal cortex of the adult mouse. Neurosci Res. 24, 329-43.

Graziano, M. (2006). The organization of behavioral repertoire in motor cortex. Annu. Rev. Neurosci., 29, 105-134.

Haug, F.M.S. (1973). Heavy metals in the brain. A light microscope study of the rat with Timm's sulphide silver method. Methodological considerations and cytological and regional staining patterns. Advances in anatomy, embryology, and cell biology, 47(4), 1-71.

Hevner, R.F. & Wong-Riley, M.T. 1992 Entorhinal cortex of the human, monkey, and rat: metabolic map as revealed by cytochrome oxidase. J. Comp. Neurol. 326, 451-69.

Honda, Y., & Ishizuka, N. (2004). Organization of connectivity of the rat presubiculum: I. Efferent projections to the medial entorhinal cortex. Journal of Comparative Neurology, 473(4), 463-484.

Hubel, D. H., & Wiesel, T. N. (1962). Receptive fields, binocular interaction and functional architecture in the cat's visual cortex. The Journal of physiology, 160(1), 106.

Ichinohe, N., Fujiyama, F., Kaneko, T., & Rockland, K. S. (2003). Honeycomb-like mosaic at the border of layers 1 and 2 in the cerebral cortex. The Journal of neuroscience, 23(4), 1372-1382.

Jain, N., Catania, K. C., & Kaas, J. H. (1998). A histologically visible representation of the fingers and palm in primate area 3b and its immutability following long-term deafferentations. Cerebral Cortex, 8(3), 227-236.

Jones, E. G. (2000). Microcolumns in the cerebral cortex. Proceedings of the National Academy of Sciences, 97(10), 5019-5021.

Kaas, J. H. (2012). Evolution of columns, modules, and domains in the neocortex of primates. Proceedings of the National Academy of Sciences, 109(Supplement 1), 10655-10660.

Kaas, J. H. (2013). The evolution of brains from early mammals to humans. Wiley Interdisciplinary Reviews: Cognitive Science, 4(1), 33-45.

Kaschube, M., Schnabel, M., Löwel, S., Coppola, D. M., White, L. E., & Wolf, F. (2010). Universality in the evolution of orientation columns in the visual cortex. science, 330(6007), 1113-1116.

Klingler, J. (1948). Die makroskopische Anatomie der Ammonsformation: Denkschriften der schweizerischen naturforschenden Gesellschaft, Band LXVIII. Abh. l , Gebrüder Fretz Ag., Zürich.

Köhler, C. (1986). Cytochemical architecture of the entorhinal area. Excitatory Amino Acids and Epilepsy. Advances in Experimental Medicine and Biology Volume 203, 1986, pp 83-98 Springer.

Kornack, D. R., & Rakic, P. (1995). Radial and horizontal deployment of clonally related cells in the primate neocortex: relationship to distinct mitotic lineages. Neuron, 15(2), 311-321.

Krieg, W. J. (1946). Connections of the cerebral cortex. I. The albino rat. B. Structure of the cortical areas. Journal of Comparative Neurology, 84(3), 277-323.

Krieger, P., Kuner, T., & Sakmann, B. (2007). Synaptic connections between layer 5B pyramidal neurons in mouse somatosensory cortex are independent of apical dendrite bundling. The Journal of Neuroscience, 27(43), 11473-11482.

Leise, E. M. (1990). Modular construction of nervous systems: a basic principle of design for invertebrates and vertebrates. Brain Research Reviews, 15(1), 1-23.

Li, Y., Lu, H., Cheng, P. L., Ge, S., Xu, H., Shi, S. H., & Dan, Y. (2012). Clonally related visual cortical neurons show similar stimulus feature selectivity. Nature, 486(7401), 118-121.

Liao, C. C., Gharbawie, O. A., Qi, H., & Kaas, J. H. (2013). Cortical connections to single digit representations in area 3b of somatosensory cortex in squirrel monkeys and prosimian galagos. Journal of Comparative Neurology.

Lorente de No, R., Studies on the structure of the cerebral cortex. I. The area entorhinalis, J. Psychol. Neurol., 45 (1933) 381-438.

Lorente de No, R., Fairen, A., Regidor, J., & Kruger, L. (1992). The cerebral cortex of the mouse: (A first contribution - The 'acoustic' cortex).

Lund, J. S., & Boothe, R. G. (1975). Interlaminar connections and pyramidal neuron organisation in the visual cortex, area 17, of the macaque monkey. Journal of Comparative Neurology, 159(3), 305-334.

Manger, P., Sum, M., Szymanski, M., Ridgway, S., & Krubitzer, L. (1998). Modular subdivisions of dolphin insular cortex: does evolutionary history repeat itself?. Journal of cognitive neuroscience, 10(2), 153-166.

Mathisen, J. S. Blackstad Th.W. (1964). Cholinesterase in the hippocampal region. Cells Tissues Organs, 56(3), 216-253.

Merritt, J. F. (2010). The biology of small mammals. JHU Press.

Meyer, H. S., Wimmer, V. C., Oberlaender, M., de Kock, C. P., Sakmann, B., & Helmstaedter, M. (2010). Number and laminar distribution of neurons in a thalamocortical projection column of rat vibrissal cortex. Cerebral Cortex, 20(10), 2277-2286.

Mikkonen, M., Soininen, H., & Pitkänen, A. (1997). Distribution of parvalbumin-, calretinin-, and calbindin-D28k-immunoreactive neurons and fibers in the human entorhinal cortex. Journal of Comparative Neurology, 388(1), 64-88.

Mountcastle, V. B. (1957). Modality and topographic properties of single neurons of cat's somatic sensory cortex. J. neurophysiol, 20(4), 408-434.

Mountcastle, V. B. (2003). Introduction. Cerebral Cortex, 13(1), 2-4.

Munk, H. (1881). Ueber die Functionen der Grosshirnrinde: gesammelte Mittheilungen aus den Jahren 1877-80. Verlag von August Hirschwald.

Nieuwenhuyis, R., ten Donkelaar, H. J., & Nicholson, C. (1998). The Central Nervous System of Vertebrates. Springer.

Ohtsuki, G., Nishiyama, M., Yoshida, T., Murakami, T., Histed, M., Lois, C., & Ohki, K. (2012). Similarity of visual selectivity among clonally related neurons in visual cortex. Neuron, 75(1), 65-72.

Peters, A. (2010). The morphology of minicolumns. In The Neurochemical Basis of Autism (pp. 45-68). Springer US.

Peters, A., & Walsh, T. M. (1972). A study of the organization of apical dendrites in the somatic sensory cortex of the rat. Journal of Comparative Neurology, 144(3), 253-268.

Retzius, G. (1896). Das Menschenhirn. Königliche Buchdruckerei, PA Norstedt & Söner.

Rockland, K. S., & Ichinohe, N. (2004). Some thoughts on cortical minicolumns. Experimental Brain Research, 158(3), 265-277.

Roney, K. J., Scheibel, A. B., & Shaw, G. L. (1979). Dendritic bundles: survey of anatomical experiments and physiological theories. Brain Research Reviews, 1(2), 225-271.

Rose, J. E., & Woolsey, C. N. (1949). The relations of thalamic connections, cellular structure and evocable electrical activity in the auditory region of the cat. Journal of Comparative Neurology, 91(3), 441-466.

Sanides, F. (1970). Functional architecture of motor and sensory cortices in primates in the light of a new concept of neocortex evolution. The primate brain: Advances in primatology, 1, 137-201.

Slomianka, L. (1992). Neurons of origin of zinc-containing pathways and the distribution of zinc-containing boutons in the hippocampal region of the rat. Neuroscience, 48(2), 325-352.

Solodkin, A., & Van Hoesen, G. W. (1996). Entorhinal cortex modules of the human brain. Journal of Comparative Neurology, 365(4), 610-627.

Stephan, H. (1975). Handbuch der mikroskopischen Anatomie des Menschen. Band 4, Teil 9 Allocortex.

Suzuki, W. A., & Porteros, A. (2002). Distribution of calbindin D?28k in the entorhinal, perirhinal, and parahippocampal cortices of the macaque monkey. Journal of Comparative Neurology, 451(4), 392-412.

Tomer, R., Denes, A. S., Tessmar-Raible, K., & Arendt, D. (2010). Profiling by image registration reveals common origin of annelid mushroom bodies and vertebrate pallium. Cell, 142(5), 800-809.

van Hoesen, G. W., Augustinack, J. C., Dierking, J., Redman, S. J., & Thangavel, R. (2000). The parahippocampal gyrus in Alzheimer's disease: clinical and preclinical neuroanatomical correlates. Annals of the New York Academy of Sciences, 911(1), 254-274.

von Economo, C. F., & Koskinas, G. N. (1925). Die Cytoarchitektonik der Hirnrinde des erwachsenen Menschen. Springer Verlag.

Wang, Q., & Burkhalter, A. (2007). Area map of mouse visual cortex. Journal of Comparative Neurology, 502(3), 339-357.

Witter, M. P., & Moser, E. I. (2006). Spatial representation and the architecture of the entorhinal cortex. Trends in neurosciences, 29(12), 671-678.

Woolsey, T. A., & Van der Loos, H. (1970). The structural organization of layer IV in the somatosensory region (SI) of mouse cerebral cortex: the description of a cortical field composed of discrete cytoarchitectonic units. Brain research, 17(2), 205-242.

Yu, Y. C., Bultje, R. S., Wang, X., & Shi, S. H. (2009). Specific synapses develop preferentially among sister excitatory neurons in the neocortex. Nature, 458(7237), 501-504.

Yu, Y. C., He, S., Chen, S., Fu, Y., Brown, K. N., Yao, X. H., ... & Shi, S. H. (2012). Preferential electrical coupling regulates neocortical lineage-dependent microcircuit assembly. Nature, 486(7401), 113-117.

Chapter 2

The Neurobiology of Etruscan Shrew Active Touch

Published as:
Brecht, M., Naumann, R., Anjum, F., Wolfe, J., Munz, M., Mende, C., & Roth-Alpermann, C. (2011). The neurobiology of Etruscan shrew active touch. Philosophical Transactions of the Royal Society B: Biological Sciences, 366(1581), 3026-3036.

Abstract

The Etruscan shrew, *Suncus etruscus*, is not only the smallest terrestrial mammal, but also one of the fastest and most tactile hunters described to date. The shrew's skeletal muscle consists entirely of fast-twitch types and lacks slow fibres. Etruscan shrews detect, overwhelm, and kill insect prey in large numbers in darkness. The cricket prey is exquisitely mechanosensitive and fast-moving, and is as big as the shrew itself. Experiments with prey replica show that shape cues are both necessary and sufficient for evoking attacks. Shrew attacks are whisker guided by motion- and size-invariant Gestalt-like prey representations. Shrews often attack their prey prior to any signs of evasive manoeuvres. Shrews whisk at frequencies of approximately 14 Hz and can react with latencies as short as 25-30 ms to prey movement. The speed of attacks suggests that shrews identify and classify prey with a single touch. Large parts of the shrew's brain respond to vibrissal touch, which is represented in at least four cortical areas comprising collectively about a third of the cortical volume. Etruscan shrews can enter a torpid state and reduce their body temperature; we observed that cortical response latencies become two to three times longer when body temperature drops from 36 °C to 24 °C, suggesting that endothermy contributes to the animal's high-speed sensorimotor performance. We argue that small size, high-speed behaviour and extreme dependence on touch are not coincidental, but reflect an evolutionary strategy, in which the metabolic costs of small body size are outweighed by the advantages of being a short-range high-speed touch and kill predator.

2.1 Introduction

2.1.1 (a) Purpose of the review: neurobiology of shrew active touch

The purpose of this review is to summarize our advances on Etruscan shrew active touch and put them in perspective with other findings on the tactile behaviour of other mammals. We believe that touch is very much an active sense and while responses to passive touch have been recorded frequently, they may not reveal all components of tactile processing. Specifically, we will portray the Etruscan shrew as short-range high-speed hunter. Shrews tackle a complex task: in darkness they detect, overwhelm and kill their insect prey, a fast moving target that is almost as big as the shrew itself (figure 2.1a). Crickets are abundant in shrew natural habitats [2] and are nocturnal, highly mobile animals endowed with a variety of mechanosensitive organs that mediate escape behaviours [3]. Thus, the behavioural ecology of shrews and crickets predisposes them towards interacting via sophisticated tactile behaviours.

2.1.2 (b) Sensory implications of small body size

The Etruscan shrew, *Suncus etruscus*, is not only the smallest shrew, but presumably also the smallest terrestrial mammal. The adult body mass of individuals caught from their natural environment ranges from 1.6 to 2.4 g [4]. While many authors have focused on the metabolic implications of small body size in mammals, few have considered the sensory implications of body size. Here we argue, however, that such scaling relationships have important implications for vibrissal touch. Etruscan shrews have a prominent vibrissae array (figure 2.1b-d). In figure 2.1e, we highlight the scaling relationship of body and vibrissa length for diverse mammals, which are all thought to be vibrissal experts. It is obvious that whiskers are relatively longer in smaller mammals; i.e. small animals have a relatively larger vibrissal sensing volume [1]. It may thus not be surprising that Etruscan shrews, like rodents, depend primarily on their well-developed array of mystacial vibrissae for tactile information [5-7]. If whiskers are protracted, the tips of the whiskers precede the snout by up to 1 cm, which is around a fifth to a third of the total body length. Etruscan shrew whiskers thus sense a longer distance ahead than in the rat or mouse. This may be necessary to avoid obstacles as the shrew locomotes very rapidly [8]. Furthermore, a longer whiskertip to mouth distance may be advantageous both in the spatial and temporal domain for successful shrew corrective manoeuvres observed in response to fast prey escape attempts [6,7]. The relatively large sensing volume scanned by the vibrissae allows the Etruscan shrew to sample more of its direct surround, which may partly explain why shrews act so fast during prey capture.

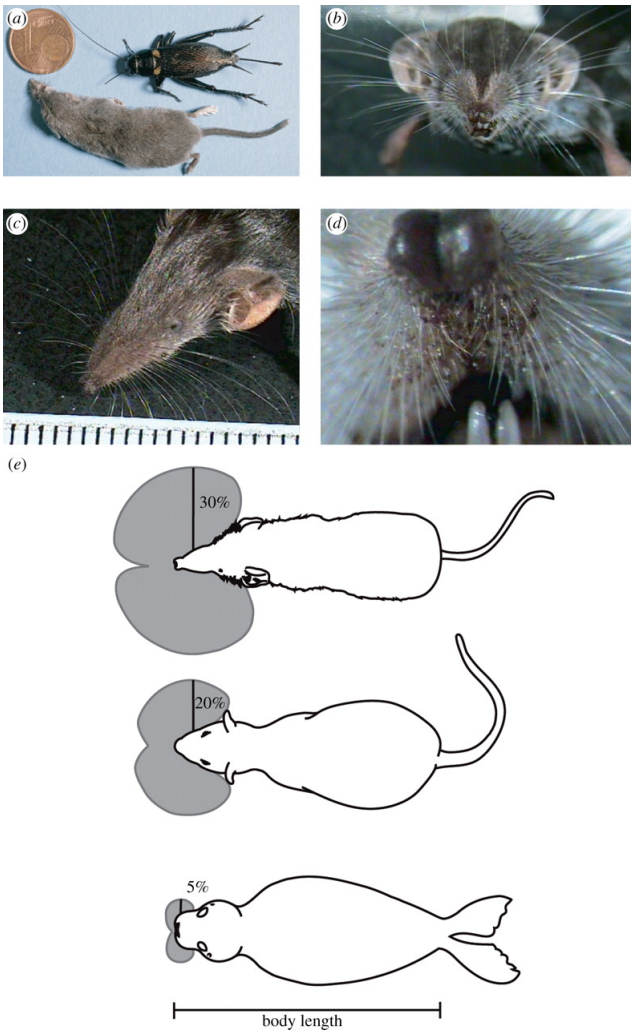

FIGURE 2.1: The Etruscan shrew and its vibrissal system. (a) An Etruscan shrew and a field cricket. The cent coin is 16.25 mm in diameter. (b) Frontal view of the head of a shrew. (c) Etruscan shrew whisker array; the longest shrew macrovibrissae are ca 12 mm long. The scale shows millimetres. (d) High magnification view of the microvibrissae surrounding the mouth. (e) Schematics of vibrissal sensing volumes [1] (grey) and body size in the Etruscan shrew, the rat (middle) and the harbour seal (bottom). The percentage value refers to the length the longest facial vibrissa and states the percentage of body length that this whisker reaches.

Shrews have very small eyes [9,10]. It has been suggested that owing to poor development of the eyes and visual system vision functions merely to discriminate light intensity [11-13], although in our hands, visual cues appeared to trigger defensive reactions. However, we never observed any evidence that visual stimuli (i.e. crickets behind a glass screen) trigger hunting behaviours.

Shrews have very small cochleas with only about 300 sensory hair cells in the smallest shrews investigated so far [14] and correspondingly small brain areas involved in auditory sensation [14-16]. As a result of reduced visual and auditory capacities in most shrews,

olfactory and somatosensory modalities have become a highly-developed and important part of their sensory repertoire [5,17-19].

Sensory organs and the brain claim high energetic costs (for a review see Niven & Laughlin [20]). Many sensory modalities such as active whisker touch require muscular movements, which further increase the energetic costs. Hence, sensory and nervous systems are subject to two conflicting selective pressures: the need to minimize energy consumption and to generate adaptive behaviour under changing environmental conditions. More specifically, in sensory systems, there will be a trade-off between the energetic costs of a sensory structure encoding a particular modality and the amount of reliable information obtained. Trade-offs may also occur between sensory systems: animals with a subterranean lifestyle such as the star-nosed mole have a highly developed mechanosensory modality with sensory specializations and expanded cortical areas at the expense of reduced vision with minute eyes and a small visual cortical region [21]. Similar trade-offs have been documented in the naked mole rat, which has been shown to be completely blind and possesses specialized sensory hairs along the body that might guide its movement within tunnels [22,23].

2.1.3 (c) Metabolic selection pressure for efficient sensorimotor performance

Small body size does not only directly impact on vibrotactile sensing, but it also results in unique selection pressures on the Etruscan shrew's hunting behaviour. Because of their small size and their large surface to volume ratio, Etruscan shrews have an extraordinarily high energy turnover. This presents an extreme challenge to all functions of the body, including respiration, oxygen transport, muscle parameters, but most importantly here the sensory and neural systems. Only because Etruscan shrews are highly efficient hunters, are they able to meet these extreme metabolic demands.

Etruscan shrews are usually homoeothermic with a normal body temperature between 34 °C and 38 °C [4,24]. Etruscan shrews resting at an ambient temperature of 20 °C have a mean body temperature of 34.7±0.5 °C [24]. During activity, the mean body temperature is 2 °C - 3 °C higher than at rest [24,25]. However, in case of food restriction and at low ambient temperature, they can reduce their body temperature and enter a torpid state to cut down their resting energy expenditure. Torpor is defined as a state of decreased physiological activity, usually characterized by a reduced body temperature and reduced metabolism. In laboratory conditions, daily torpor cycles were observed with body temperatures lowered to about 12 °C, in extreme cases even to 6 °C [26,27]. Shrews can warm up from torpor very rapidly at a rate of around 1 °C per minute by

muscle shivering and heat generation from brown adipose tissue [27]. Under normothermic resting conditions, the specific oxygen consumption rate of S. etruscus is 67 times higher than in humans. A maximal heart rate of up to 1500 beats per minute exceeds all values reported for other endothermic animals [4]. This species has the highest mass-specific metabolic rate of all mammals [28] and thus there is an immense pressure to obtain prey. Shrews as small as S. etruscus need to ingest food at least every hour and have to consume up to six times their own body weight of insects every day [29].

Muscles play a major role in the capture and chewing of prey, but S. etruscus requires fast skeletal muscles not only for locomotion but also for effective heat production and for an extremely high ventilation rate [28]. Skeletal muscles can contract at up to 780 min^{-1} for running, up to 3500 min^{-1} for shivering and up to 900 min^{-1} for respiration. Both structural and functional properties demonstrate that the Etruscan shrew's skeletal muscles are well adapted to fit the needs of this animal's extreme metabolism; they lack slow-twitch type I fibres and consist only of fast-twitch IID fibres. The enzymatic characteristics of these fibres make them optimally equipped for an almost purely oxidative metabolism [30].

With a brain mass of about 60 mg, the Etruscan shrew has the smallest mammalian brain known [31]. In such small brains, axons are typically densely packed, small in diameter and mostly unmyelinated. Unmyelinated axons have high capacitance per unit length and are energetically more expensive than myelinated axons [32]. In the tiny shrew, the estimated metabolic cost for generating an action potential for all white matter fibres averaged is an order of magnitude higher than in the macaque and 97 per cent of this cost is accounted for by the unmyelinated axons.

In summary, surface to volume considerations imply that a homoeothermic body temperature is metabolically highly costly. The musculature of Etruscan shrews is specialized for fast movement, and an increased body temperature might also offer massive advantages in terms of processing speed (see below).

2.1.4 (d) Sensory ecology: Etruscan shrews specialize in a hidden life in slits

There are more than 300 species of shrews and they share common features, such as a small body size and prominent whiskers on a pointed snout. Shrews belong to the order Soricomorpha. Fossil evidence suggests that the earliest mammals were shrew-like in body size. Their brains were similarly small as those of extant shrews and possibly afforded similar behavioural capabilities [33,34].

In Europe, the Etruscan shrew is mainly found in the Mediterranean lowlands and in Asia in a belt extending between 10 ° N and 30 ° N [30]. Their habitat includes forest, shrub and grassland environments [35]. As for many other species in the genus Suncus, the Etruscan shrew is most likely solitary and territorial, except during the breeding season [36,37]. Being hunted by predator birds such as owls [38], shrews try to avoid moving uncovered in the open field, but rather seek shelter under piles of rock, pieces of bark or other organic material and in tunnels that they dig in loose soil. Often they are found resting in old dry stone walls, where they also build nests for bringing up their young. Strikingly agile animals, shrews squeeze their body through tiny holes and they are able to enter and capture prey in slits as thin as 7 mm.

Shrews are opportunist insectivores and all species consume a wide range of prey. Studies of the feeding habits of shrews and their prey availability demonstrate that small size brings benefits as well as costs [39]. The greatest advantages for small shrews are their lower absolute food requirements and the ability to subsist on small, numerous and accessible arthropods with high encounter rates, available in different seasons and low-productivity habitats. Major costs of small size are a reduction in food niche breadth and prey biomass resulting from restrictions on the type and size of prey eaten, and large territory requirements with a consequential increase in the energetic cost of foraging and territory maintenance. Owing to their constant food requirement, shrews have polyphasic circadian activity patterns with frequent activity bouts distributed evenly over a period of 24 h [9,35,40-43]. This means that shrews have to be able to successfully hunt in twilight as well as in darkness. Vision can be furthermore limited in typical shrew habitats, such as dense brush vegetation or tunnels in stone walls or the soil [9] and indeed, sight only seems to play a minor role for navigation and prey capture [6,7,13,44].

When exploring new environments, shrews frequently emit faint, high-pitched laryngeal calls (twittering) of unclear function [9]. While a few authors claimed that shrews make use of echolocation [45-48], others found no evidence for this ability [8,19]. A recent study proposed that shrew-like calls can yield echo scenes useful for habitat assessment at close range, beyond the range of the shrews' vibrissae. At the same time, it seems unlikely that they can make bat-like use of echolocation to search for prey [49]. In summary, we suggest that the secret life of Etruscan shrews in slits, where they hunt large and diverse prey, might predispose them to rely on proximal tactile cues.

2.2 Tactile prey capture behaviour

2.2.1 (a) Tactile hunting of highly mechanosensitive cricket prey

Since the pioneering work of von Uexküll, it is clear that understanding sensory performance of predators requires analysis of the sensory characteristics of their prey [50]. Crickets are found in abundance in the natural habitat of the Etruscan shrew and therefore are thought to be an important prey [2]. A cricket can measure up to 35 mm (body of the Etruscan shrew measures between 35 and 50 mm) and has very long antennae and prominent jumping legs (figure 2.1a). Crickets are fast moving prey and very capable of evading attacks. A variety of mechanoreceptors, different kinds of receptors and mechano sensory sensilla are found in and on the cricket body and appendages, just as in other insects (e.g. cockroaches, locusts). A cricket shows a range of behavioural responses to stimulation of its mechanoreceptors, extending from ignoring the stimulus to altering complex behavioural sequences such as avoidance manoeuvres, orientation and approach or fighting (see [51,52]). Furthermore, the input from mechanoreceptors is known to inhibit ongoing behavioural activity, e.g. singing or walking stops when a predator approaches [53]. While the antennae are versatile head appendages with the ability to sense the environment up to twice its body length, cerci, the two caudal antenna-like appendages are mainly known to guard the rear of the insect [54-57]. Any defensive or escape behaviour guided by cercal mechanoreceptors depends on their stimulation [58].

Mechanisms of escape behaviour have been studied intensely [3,59,60]. Wind and touch stimuli have been used to study defensive (kicking) and escape responses. When a digger wasp makes contact with the cricket, it first leads to a head stand (sudden raising of the abdomen), followed by a stilt stand with the further raising and tilted posture, which is followed by a rapid kick with one hind leg casting the wasp several centimetres away. The kick is completed in 100 ms after the touch and can also be followed by a second kick [52,61]. We observed that Etruscan shrews quickly retracted their snout after placing attacks on crickets, probably to avoid being kicked. The escape response can be a turn, a jump or both and often is followed by running.

2.2.2 (b) Tactile guidance of prey capture

Anjum et al. [6] studied the hunting behaviour of Etruscan shrews in a laboratory setting. In these experiments, the spatio-temporal analysis of numerous attacks was combined with whisker removal and prey manipulation experiments. Etruscan shrews direct their attacks selectively to the cricket's thorax and manage to keep this precision

regardless of the size of the prey (figure 2.2a,b). They attack crickets from the side with a narrow distribution of attack angles around 90 ° relative to the cricket's body axis. Although most attacks are directed straight ahead, there is a slight lateralization in the hunting behaviour towards rightward attacks.

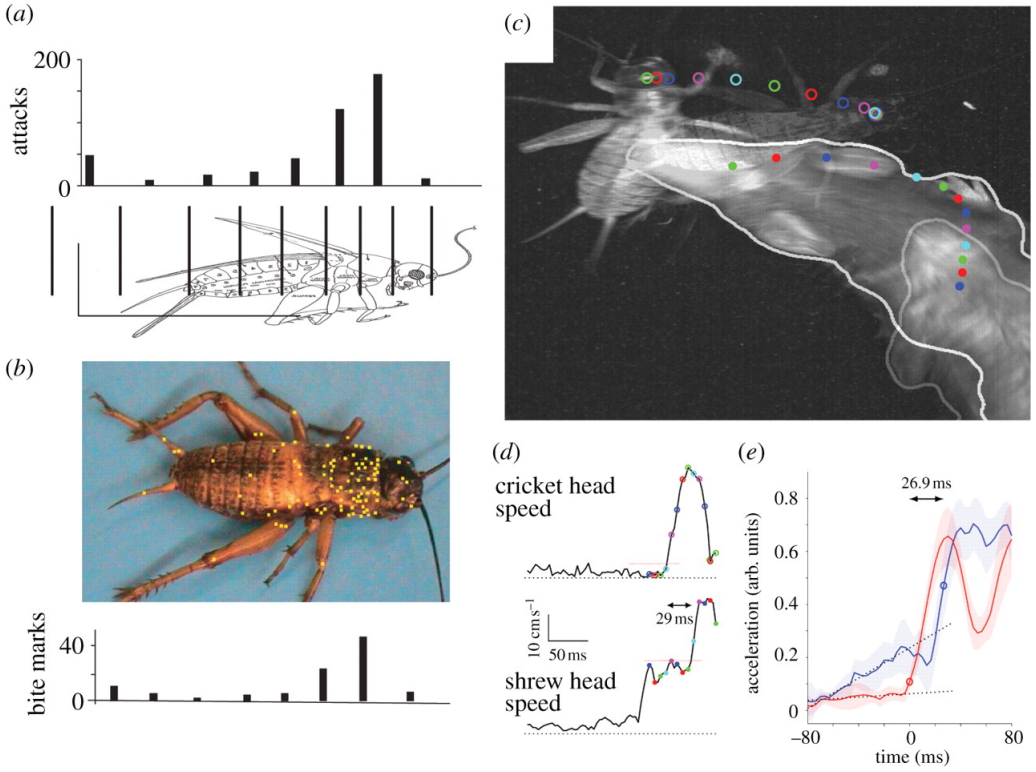

FIGURE 2.2: Precision and speed of shrew attacks. (a,b) Shrew attacks are selectively placed on the thorax of crickets. Modified from Anjum et al. [6]. (a) Attack histogram derived by analysing video sequences (n = 450 shrew attacks on approx. 130 crickets). (b) Bite mark positions (yellow squares superimposed on a cricket photograph (n = 94 bite marks on 25 freshly killed, immobilized or injured crickets)) and bite mark histogram. (c-e) Mid-attack change of direction. Modified from Munz et al. [7]. (c) Still frames from before and at the end of the attack (time lapse between images = 0.23 s) are overlaid. Dots and circles are the head positions of the shrew and cricket, respectively. Dots and circles are colour-coded for simultaneous head positions of the shrew and cricket. (d) Head speed of the cricket (top) and shrew (bottom). Note the 29 ms lapse between the cricket's speed increase and the shrew's speed increase. Black dotted lines represent 0 cm s^{-1}, red-dotted lines represent the thresholds used to determine the time of speed increase. (e) Average of six such attacks. Black dashed lines are linear fits to the baseline acceleration prior to the sudden increase in cricket acceleration (t = 0 ms). Shaded regions represent 1 s.e. The difference in time between the cricket and the shrew acceleration increase was 27 ms. (e) Brown curve, cricket; blue curve, shrew.

2.2.2.1 (i) High speed of prey capture

Prey capture occurs very quickly, i.e. in 80-200 ms per attack, with short inter-attack intervals. While first attacks were distributed relatively broadly over the cricket's body,

subsequent attacks were directed more and more precisely to the thorax.

2.2.2.2 (ii) Whisker-dependent shape recognition

Removal experiments showed that both macro- and microvibrissae are required for hunting [6]. Experiments with dummy prey objects showed that shrews attacked a plastic replica of a cricket but not other plastic objects of similar size. Altering the shape of crickets by gluing on additional body parts from donor animals revealed that the jumping legs but not the head are key features in prey recognition. Addition of such ectopic jumping legs is highly confusing for shrews and leads to dramatic changes in attack patterns. Thus, tactile shape cues are both necessary and sufficient for evoking attacks. Both the generalized effects of cricket shape manipulation experiments and characteristics of corrective manoeuvres indicate that shrew behaviour is guided by Gestalt-like prey descriptions [6].

2.2.3 (c) Shrew whisking and active touch in prey capture

We recently characterized Etruscan shrew whisking and tactile behaviour during prey capture [7]. To this end, we combined staged shrew-cricket encounters with whisker tagging and high-speed videography.

2.2.3.1 (i) Basic characteristics of Etruscan shrew whisking

Like other mammals, such as mice and rats, Etruscan shrews engage in rhythmic back and forth whisker movements, i.e. whisking. The average power spectrum shows a very clear peak in the shrew whisking at approximately 14 Hz. This is a considerably higher whisking frequency than that of rats (approx. 8 Hz), but is similar to mice [62]. Clearly, shrews employ periodic whisking during their hunting behaviour and the shrew whiskers are under active muscle control. Compared with rats, shrews had lower amplitude whisking (approx. 30 ° versus approx. 50 ° in rats). Interestingly, as in rats, retraction velocity was almost double protraction velocity.

2.2.3.2 (ii) Whisking during hunting

Etruscan shrew whisking during hunting can be divided into phases: (i) immobile resting prior to hunting. Prior to hunting shrews often showed very little head or whisker movement. (ii) Search phase. The search phase is likely induced by the detection of

prey odors, which can be sensed over longer distances. The beginning of the search phase was determined by an increase in the head velocity. Concurrent with increased head motion the whisker set angle increased and whisker motion increased. During the search phase we often observed highly regular periodic whisking. (iii) Contact phase. The first whisker-to-cricket contact defined the transition from the search to the contact phase. This phase was kept very short by the shrew, as crickets tried to escape before the shrew was able to strike. Following contact, whisking amplitude decreased and there was a small increase in the whisker set angle. (iv) Attack phase. Attack was defined by a sudden increase in head acceleration directed towards the cricket. This is a brief behavioural event with a sharp increase in head acceleration. The shrew's trunk dramatically bent during the strike and assumed the shape of a parrot beak.

2.2.3.3 (iii) Mid-flight changes in attack direction indicate short reaction times

As illustrated in figure 2.2c-e, we found that shrews were able to react to cricket movements during the short duration of the attack. In figure 2.2c, we overlaid video images taken just before and at the end of an attack. The dots and circles show the head positions of the cricket and shrew, respectively, during the attack. The dots and circles are colour coded to show simultaneous shrew and cricket head positions (note that the first four cricket head positions are nearly identical). In this example, the shrew is initially moving upward in the video and the cricket is still. When the cricket suddenly jumps backward, the shrew reacts by adjusting its trajectory. It was found that shrews have a preferred side when attacking, however the neural basis for this form of "handedness" is not known [6]. We estimated the reaction time of the shrew by looking at the time delay between the cricket's sudden speed increase, corresponding to its attempted flight, and the shrew's increase in head speed as it adjusts its attack. In this example, we found that it took the shrew only 29 ms to react to the cricket's escape attempt (figure 2.2d). On average, the shrew's increased head acceleration followed the cricket's sudden acceleration by 27 ms (figure 2.2e). It was previously reported that shrews react to underwater stimuli with a latency on the order of 20 ms, in good agreement with the values reported here [19]. Overall, the observations from high-speed videography strongly support the idea that shrews out-manoeuvre their very large prey by high-speed performance. Indeed, about 40 per cent of shrew attacks target stationary prey and the first strike often occurs prior to any evasive manoeuvre [6]. Both short reaction times and short attack intervals suggest that shrews identify and target their prey with a single touch.

2.2.4 The shrew somatosensory system

2.2.5 (a) Periphery

The Etruscan shrew's prominent whisker fan has already been introduced in figure 2.1. Selective whisker removal experiments demonstrated a functional differentiation of shrew whiskers in prey capture [6]. The large macrovibrissae (figure 2.1c) were required for prey targeting, whereas the small microvibrissae around the shrew's mouth (figure 2.1d) were necessary for initiating the final strike/bite in attacks. Figure 2.3a shows the left whiskerpad with the vibrissal follicles clearly visible. The whiskers on each side of an Etruscan shrew's snout are arranged in a grid made up of six rows (A to F) and several arcs. Each row contains six to nine whiskers. In addition, there are three whiskers not contained in a row or an arc, labelled X, Y and Z. In total, there are more than hundred vibrissae extending like a fan from the snout of the Etruscan shrew. In larger shrews, even higher numbers of vibrissae have been described [60,63,64]. Differences between shrew and rodent vibrissal follicles have been described [63,65,66].

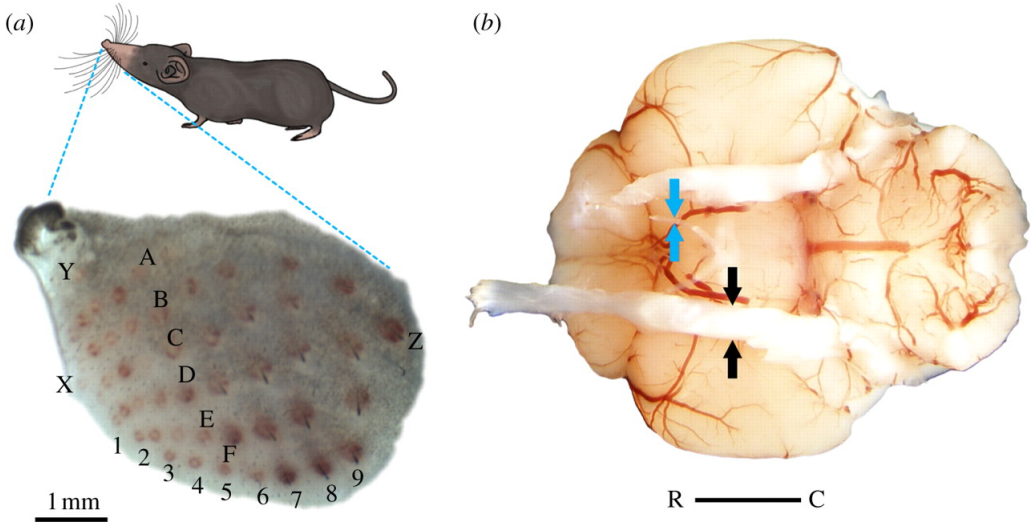

FIGURE 2.3: Periphery of the Etruscan shrew vibrissal system. (a) Pattern of vibrissal follicles shown in a flattened preparation showing six rows (A-F). Each row contains six to nine whiskers. In addition, there are three whiskers not contained in a row or an arc and labelled X, Y and Z. Scale bar applies to (a) and (b). (b) Ventral view of the shrew's brain. The trigeminal nerve is indicated as black arrows and optic nerve as blue arrows. R, rostral; C, caudal.

Touch signals from the follicles are relayed to the brainstem via the trigeminal nerve. In the long-clawed shrew (Sorex unguiculatus), which is about 10 times larger than the Etruscan shrew, each sinus hair follicle is innervated by 60-100 myelinated fibres [61]. The fibres from the sinus hair follicles join to form the maxillary branch of the trigeminal nerve. The thick trigeminal nerve compared with the much thinner other cranial nerves gives a stunning impression of the significance of touch information from the facial

region for the Etruscan shrew. Figure 2.3b shows the trigeminal nerve framed by black arrows and the optic nerve framed by blue arrows for comparison. The differences in macromorphology of the sensory cranial nerves are mirrored by the number of sensory fibres contained in those nerves. In the northern short-tailed shrew (*Blarina brevicauda*), there are about 15 000 fibres in the infraorbital part of the trigeminal nerve compared with less than 500 fibres in the optic nerve [67]. More recently, differences in fibre distribution were reported for the similarly sized American water shrew (*Sorex palustris*), which has about 30 000 axons in the trigeminal nerves, less than 6000 in the optic nerves and 6000-7000 in the auditory nerves [68]. The most extreme of the small mammals is probably the star-nosed mole (*Condylura cristata*)-its touch sensitive appendages are innervated by about 100 000 myelinated nerve fibres [69].

2.2.6 (b) Cortical organization: anatomy

The Etruscan shrew has the smallest brain of all mammals. Its cerebral cortex is very thin, only 400 to 500 μm on average [16,70]. As in other mammals, the cortex of the Etruscan shrew is a cytoarchitectonically heterogeneous sheet of tissue. The presence of distinct cortical areas is suggested by the fact that different staining methods (Nissl, cytochrome oxidase activity, myelin) indicate the same areal borders. Sensory neocortical areas could be clearly identified by cytochrome oxidase and myelin staining in coronal and tangential brain sections. In total, there are about 10-15 cortical areas-a relatively large number given the small size of the Etruscan shrew cerebral cortex [Chapter 3, Figure 3.10; 71,72].

We compared volumes of cortical areas of the Etruscan shrew with data for the cerebral cortex of the rat, which is 100 times larger than in the shrew. We included all areas of the neocortex, as well as entorhinal and piriform cortex [72,73]. The most striking difference is that entorhinal cortex and piriform cortex comprise a much larger part of the cortical mantle in the Etruscan shrew (approx. 42%) than in the rat (approx. 17%). We recorded neuronal responses to touch stimuli in somatosensory cortex, insular cortex and perirhinal cortex of the Etruscan shrew (see §2.3c), these areas combined take up about one-third of the total cortical volume in the Etruscan shrew as well as in the rat. In the Etruscan shrew auditory and visual cortex comprise only about 2-3% of the cortical volume, whereas it is four to five times more in the rat. The differences in relative cortical volumes are mirrored by findings in relative cortical area sizes [74] and neuron numbers [72]. In summary, the Etruscan shrew devotes a large cortical volume to somatosensation, whereas visual and auditory processing takes up only small fractions. The superb tactile capacities are reflected in the anatomy of the shrew cortex.

2.2.7 (c) Cortical organization: physiology

The neurophysiology of the Etruscan shrew is of interest both because of their small brain size and their remarkable behavioural capacities. Work on related northern American shrew species showed that these shrews have fewer sensory cortical areas than many mammals with larger brains, which include a large primary and secondary somatosensory cortical area and a primary visual and auditory cortex [15], a pattern in line with the numerous specializations of insectivores for somatosensation [21]. This means that, while shrews are likely to have sensory areas for each sensory modality, they have fewer areas than other species for specific sensory modalities such as vision.

We investigated cortical organization in Etruscan shrews by electrophysiological mapping in combination with histological verification of recording sites [16]. We characterized cortical multi-unit responses to auditory, visual and somatosensory stimuli. We found that large parts of shrew cortex (7.3 mm^2 of approx. 12 mm^2 total neocortical surface, i.e. approx. 60%) responded to such stimuli (figure 2.4a). The true fraction of sensory cortex in Etruscan shrews is probably substantially higher, because we did not test for olfactory and gustatory responses and we could only map three-quarters of the cortical sheet.

Auditory and visual stimuli activated only small parts of Etruscan shrew cortex (figure 2.4a). Tactile processing, however, appears to occur in multiple cortical regions. Large fractions of these somatosensory areas responded to macrovibrissae stimulation. We identified two topographically organized somatosensory areas with small receptive fields referred to as putative primary somatosensory cortex (S1) and putative secondary somatosensory cortex (S2). A third tactile region was located posterior-laterally, where we observed large somatosensory receptive fields and often polysensory responses. Furthermore, we identified an anterior-lateral region with large unimodal somatosensory receptive fields. The latter two regions partially overlapped with piriform cortex. Putative S1 and S2 have relatively small receptive fields. The receptive field size of about 10 whiskers per multi-unit recording site was similar or slightly larger than what has been measured in other shrew species [15] and larger than most of the receptive field sizes reported in rodent S1 [75]. It appears probable that putative areas S1 and S2 of the Etruscan shrew are homologous to these respective areas described in other shrews and to areas S1 and S2 in rodents. If one compares the Etruscan shrew cortex to that of other mammals studied thus far, it is clear that this animal is one of the most extreme tactile specialists studied to date. Only a few animals such as the star-nosed mole [69] and the naked mole-rat [76] devote a similar fraction of their neocortex to somatosensory representations.

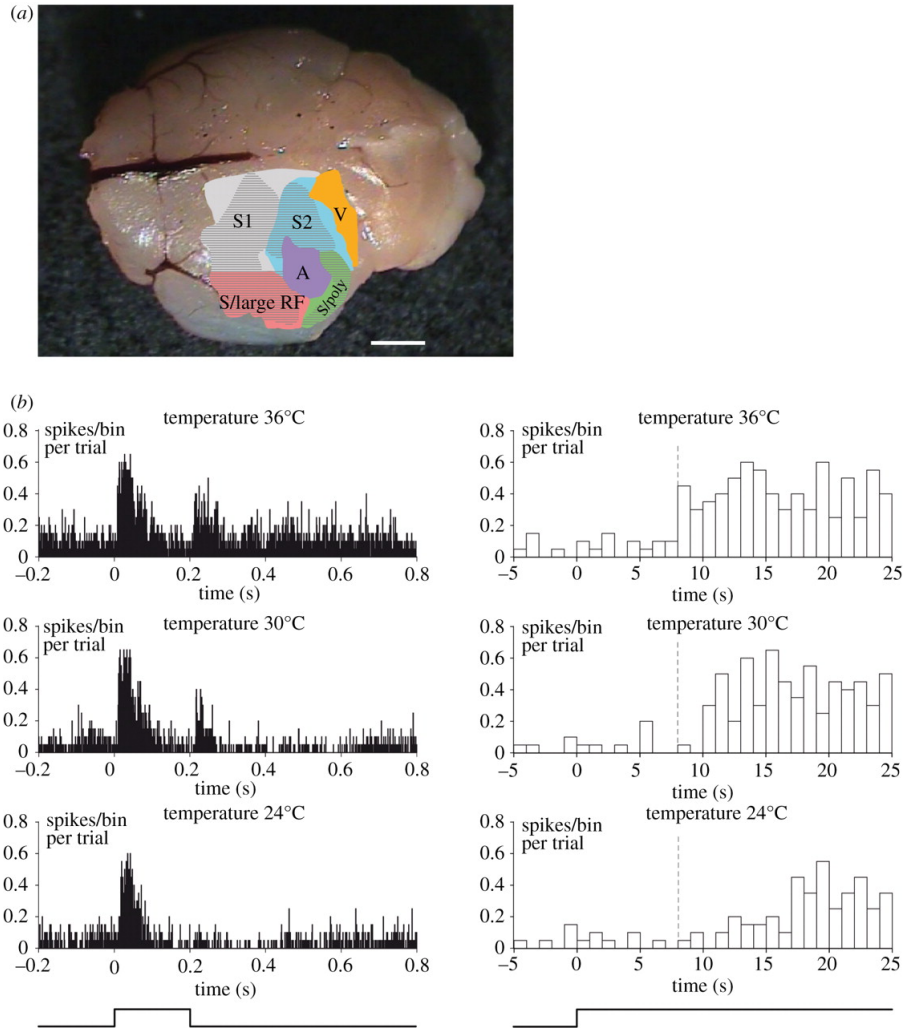

FIGURE 2.4: Etruscan shrew neurophysiology. (a) Physiologically derived map of the Etruscan shrew cortex. An average map of cortical regions was delineated by electrophysiological mapping experiments. Dotted areas indicate macrovibrissae responses. S1, primary somatosensory cortex; S2, secondary somatosensory cortex; V, visual cortex; A, auditory cortex; S, somatosensory; RF, receptive field. (b) Whisker responses at different shrew body temperatures. Peristimulus time histograms (1 ms bin size) of multi-unit responses to piezoelectric stimulation (approx. 10 ° deflection and approx. 1 ms rise time) of a single whisker (n = 20 trials per temperature). Neuronal responses were obtained at the same recording site in putative area S1 while the body temperature of the shrew varied from 36 °C (top) to 24 °C (bottom). Stimulus onset at time point 0, duration of the stimulus 200 ms, as indicated below. Right: same data as left, but zoomed into the time of stimulus onset. Dashed line indicates the time of first response at 36 °C. Note the latency changes with temperatures.

We also investigated the effects of body temperature on cortical processing. These experiments were carried out under urethane anaesthesia. In order to minimize the stress associated with the intraperitoneal urethane injection, animals were first lightly anaesthetized by isoflurane inhalation. We then injected approx. 45 μl of 4 per cent urethane solution in water for an adult approximately 2.5 g shrew (a dose of approx. 0.7 mg urethane g^{-1} body weight). To this end, we made use of the fact that shrews easily withstand passive cooling during anaesthesia. Their resistance to cooling might be related to their physiological ability to reduce body temperature and enter a torpid state (see §2.1c; [26,27]). At a low body temperature of 24 °C neuronal response, latencies to whisker stimulation with a piezoeletric device were long and responses to stimulus offset were absent (figure 2.4b). With increasing body temperatures, latencies became faster and the off-response was more prominent (figure 2.4b). Thus, even in a torpid state with low body temperature, the cortex responds reliably to sensory stimulation, albeit with longer latencies. The exact reason for the massive increase in response latency is not yet clear. Both neural (decreased axonal transduction velocity and delays in synaptic transmission) and biomechanical (changes in tissue/whisker biomechanics through altered viscous damping or slack) factors could play a role. The available data suggest that transduction of force is mediated directly by force gated channels in rodents and occurs at very short latencies (down to 300 μs) [77,78]. Furthermore, the speed of mechanotransduction appears to be relatively insensitive to temperature [79]. These considerations point to a neural origin of the increase in response latency.

With their specialized musculature and their extraordinarily high content in brown adipose tissue, Etruscan shrews possess effective mechanisms for thermogenesis, which allow them to heat up very quickly. During activity, body temperature can climb to 38 °C. For a non-mammalian insect-hunting species, the diurnal basking lizard Lacerta vivipara, it was shown that maintaining high body temperatures of 30 °C-36 °C increased predatory efficiency [80]. Thus, homeothermy might offer the shrew considerable temporal advantage over its poikilothermic prey, which operates at lower temperatures.

2.3 Discussion

Comparing shrew touch to tactile sensing in other mammals, we find both similarities and striking differences. Human haptic sensing (reviewed in this volume by Klatzky & Lederman [81]) is similar in that it also extracts shape information from touch. A striking difference is the speed of performance, which is slow (compared with vision) in the human haptic system, because it relies on the serial/gradual scanning of objects with fingertips [81]. This is very different from vibrissal touch, in which global stimulus features appear to be extracted in a single whisker sweep. Shrew whisker touch is breathtakingly fast such that prey capture movies need to be slowed down several-fold to be accessible for visual analysis. Two factors might contribute to this difference in speed. First, sensing volume [1] is-compared to body size-large for shrew whiskers, but relatively small for fingertips. Second ecological constraints on tactile sensing are very different in shrews and humans. Shrews use whiskers to hunt fast moving prey, which is not the case for human finger use. The Etruscan shrew's tactile prey recognition shares characteristics of human visual object recognition [6]: (i) it is size invariant, (ii) motion-invariant, (iii) it is based on Gestalt-like prey descriptions. We refer to prey sensing in shrews as Gestalt-like, because they do seem to analyse prey not in a piecewise fashion, but instead seem to form a global construct of what a cricket is like. As a consequence, 'local' manipulations of prey shape such as the addition of another pair of jumping legs can have 'global' effects and result in changes of most shrew attacks on such manipulated prey. It is not yet known why shrews rely on such Gestalt-like prey descriptions. We argue that Gestalt-like prey descriptions help them in directing prey capture manoeuvres, where local information, such as a contact with the abdomen can be used to steer an attack towards the thorax. Furthermore, Gestalt-like prey descriptions might help in generalizing across prey shapes and sizes, an obvious advantage given the diverse prey that shrews hunt in their habitats.

Touch in the star-nosed mole, another highly tactile insectivore species, is reviewed by Catania [82]. Similar to shrews, star-nosed moles appear to be specialized to handle prey very quickly. Different from Etruscan shrews, however, the star-nosed mole touch seems to be specialized for handling a large number of small (simple) prey items rather than to focus on sophisticated attack manoeuvres and the capturing and sensing of large prey [76].

Overall, we find that the Etruscan shrew is not only one of the smallest mammals, but also one of the fastest and most tactile mammalian hunters. These three features (small size, high-speed and extreme dependence on touch) of prey capture are hardly coincidental. Instead, we argue that the shrew has responded to the strong selection pressures associated with the metabolic costs of being a small mammal by taking full

advantage of the added speed that endothermy permits. It also takes advantage of the fact that the relative vibrissal sensing volumes seem to be inversely related to body size and the very fast transduction via mechano-gated channels [77,78] in the somatosensory system.

2.4 References

1 Nelson, M. E. & MacIver, M. A. 2006 Sensory acquisition in active sensing systems. J. Comp. Physiol. A Neuroethol. Sens. Neural. Behav. Physiol. 192, 573586. (doi:10.1007/s00359-006-0099-4)

2 Spitzenberger, F. 1990 Suncus etruscus (Savi, 1822)- Etruskerspitzmaus. In Handbuch der Säugetiere Europas:-Bd (eds J. Niethammer & F. Krapp), pp. 375392. Wiesbaden: Aula Verlag.

3 Tauber, E. & Camhi, J. 1995 The wind-evoked escape behavior of the cricket Gryllus bimaculatus: integration of behavioral elements. J. Exp. Biol. 198, 18951907.

4 Jürgens, K. D., Fons, R., Peters, T. & Sender, S. 1996 Heart and respiratory rates and their significance for convective oxygen transport rates in the smallest mammal, the Etruscan shrew Suncus etruscus. J. Exp. Biol. 199, 25792584.

5 Catania, K. C. 2000 Epidermal sensory organs of moles, shrew moles, and desmans: a study of the family Talpidae with comments on the function and evolution of Eimers organ. Brain Behav. Evol. 56, 146174. (doi:10.1159/000047201)

6 Anjum, F., Turni, H., Mulder, P. G. H., van der Burg, J. & Brecht, M. 2006 Tactile guidance of prey capture in Etruscan shrews. Proc. Natl Acad. Sci. USA 103, 16 54416 549. (doi:10.1073/pnas.0605573103)

7 Munz, M., Brecht, M. & Wolfe, J. 2010 Active touch during shrew prey capture. Front. Behav. Neurosci. 4, 191. (doi:10.3389/fnbeh.2010.00191)

8 Grünwald, A. 1969 Untersuchungen zur Orientierung der Weisszahnspitzmäuse (SoricidaeCrocidurinae). Z. Vergl. Physiol. 65, 191217. (doi:10.1007/BF00297683)

9 Churchfield, S. 1990 The natural history of shrews. CA, USA: Comstock.

10 Stephan, H., Baron, G. & Frahm, H. D. 1991 Insectivora: with a stereotaxic atlas of the hedgehog brain. Berlin, Germany: Springer.

11 Merriam, C. 1884 Blarina brevicauda. The mammals of the Adirnondack region, northeastern New York. New York, NY: L. S. Foster Press.

12 Seton, E. T. 1909 Life-histories of northern animals: an account of the mammals of Manitoba/by Ernest Thompson Seton, naturalist to the Government of Manitoba; with 68 maps and 560 drawings by the author.
New York, NY: Scribner. See http://www.biodiversitylibrary.org/bibliography/8824.

13 Branis, M. & Burda, H. 1994 Visual and hearing biology of shrews. In Advances in the biology of shrews (eds J. F. Merritt, G. L. Kirkland & R. K. Rose), pp. 189200. Pittsburgh, PA: Carnegie Museum of Natural History Press.

14 Burda, H. 1979 Morphology of the middle and inner ear in some species of shrews (Insectivora, Soricidae). Acta Sci. Nat. Brno 13, 148.

15 Catania, K. C.,Lyon,D. C.,Mock,O. B.&Kaas, J.H. 1999 Cortical organization in shrews: evidence from five species. J. Comp. Neurol. 410, 5572. (doi:10.1002/(SICI)1096-9861(19990719)410:1,55::AID-CNE6.3.0.CO;2-2)

16 Roth-Alpermann, C., Anjum, F., Naumann, R. & Brecht, M. 2010 Cortical organization in the Etruscan shrew (Suncus etruscus). J. Neurophysiol. 104, 23892406. (doi:10.1152/jn.00762.2009)

17 Schmidt, U. 1979 Die Lokalisation vergrabenen Futters bei der Hausspitzmaus Crocidura russula Hermann. Z. f. Säugetierkunde 44, 5960.

18 Schmidt, U. & Nadolski, A. 1979 Die Verteilung von olfaktorischem und respiratorischem Epithel in der Nasenhöhle der Hausspitzmaus, Crocidura russula Hermann. Z. f. Säugetierkunde 44, 1825.

19 Catania, K. C., Hare, J. F. & Campbell, K. L. 2008 Water shrews detect movement, shape, and smell to find prey underwater. Proc. Natl Acad. Sci. USA 105, 571576. (doi:10.1073/pnas.0709534104)

20 Niven, J. E. & Laughlin, S. B. 2008 Energy limitation as a selective pressure on the evolution of sensory systems. J. Exp. Biol. 211, 17921804. (doi:10.1242/jeb.017574)

21 Catania, K. C. 2005 Evolution of sensory specializations in insectivores. Anat. Rec. Discov. Mol. Cell Evol. Biol. 287, 10381050. (doi:10.1002/ar.a.20265)

22 Crish, S. D., Rice, F. L., Park, T. J. & Comer, C. M. 2003 Somatosensory organization and behavior in naked mole-rats I: vibrissa-like body hairs comprise a sensory array that mediates orientation to tactile stimuli. Brain Behav. Evol. 62, 141151. (doi:10.1159/0000 72723)

23 Hetling, J. R., Baig-Silva, M. S., Comer, C.M., Pardue,M. T., Samaan, D. Y., Qtaishat, N. M., Pepperberg, D. R. & Park, T. J. 2005 Features of visual function in the naked mole-rat Heterocephalus glaber. J. Comp. Physiol. A Neuroethol. Sens. Neural Behav. Physiol. 191, 317330. (doi:10.1007/s00359-004-0584-6)

24 Frey, H. 1979 La temperature corporelle de Suncus etruscus (Soricidae, Insectivora) au cours de lactivite, du repos normothermique et de la torpeur. Rev. Suisse Zool. 86, 653662.

25 Ishii, K., Uchino, M., Kuwahara, M., Tsubone, H. & Ebukuro, S. 2002 Diurnal fluctuations of heart rate, body temperature and locomotor activity in the house musk shrew (Suncus murinus). Exp. Anim. 51, 5762. (doi:10.1538/expanim.51.57)

26 Frey, H. & Vogel, P. 1979 Etude de la torpeur chez Suncus etruscus (Savi, 1822) (Soricidae, Insectivora) en captivite. Rev. Suisse Zool. 81, 2336.

27 Fons, R., Sender, S., Peters, T. & Jürgens, K. D. 1997 Rates of rewarming, heart and respiratory rates and their significance for oxygen transport during arousal from torpor in the smallest mammal, the Etruscan shrew Suncus etruscus. J. Exp. Biol. 200, 14511458.

28 Peters, T., Kubis, H. P., Wetzel, P., Sender, S., Asmussen, G., Fons, R. & Jürgens, K. D. 1999 Contraction parameters, myosin composition and metabolic enzymes of the skeletal muscles of the Etruscan shrew Suncus etruscus and of the common European whitetoothed shrew Crocidura russula (Insectivora: Soricidae). J. Exp. Biol. 202, 24612473.

29 Morrison, P., Ryser, F. A. & Dawe, A. R. 1959 Studies on the physiology of the masked shrew Sorex cinereus. Physiol. Zool. 32, 256271.

30 Jürgens, K. D. 2002 Etruscan shrew muscle: the consequences of being small. J. Exp. Biol. 205, 21612166.

31 Fons, R., Stephan, H. & Baron, G. 1984 Brains of Soricidae. I. Encephalization and macromorphology, with special reference to Suncus etruscus. Z. Zool. Syst. Evol.-forsch. 22, 145158. (doi:10.1111/j.1439-0469. 1984.tb00653.x)

32 Wang, S. S., Shultz, J. R., Burish, M. J., Harrison, K. H., Hof, P. R., Towns, L. C., Wagers, M. W. & Wyatt, K. D. 2008 Functional trade-offs in white matter axonal scaling. J. Neurosci. 28, 40474056. (doi:10.1523/JNEUROSCI.5559-05.2008)

33 Kielan-Jaworowska, Z. 2004 Mammals from the age of dinosaurs: origins, evolution, and structure. New York, NY: Columbia University Press.

34 Catania, K. C. & Henry, E. C. 2006 Touching on somatosensory specializations in mammals. Curr. Opin. Neurobiol. 16, 467473. (doi:10.1016/j.conb.2006.06.010)

35 Vogel, P. 1970 Biologische Betrachtungen an Etruskerspitzmäusen (Suncus etruscus Savi, 1822). Z. f. Säugetierkunde 33, 173185.

36 Davison, G. 1979 Some notes on Savis pygmy shrew. Malay. Nat. J. 32, 227231.

37 Nowak, R. M. 1999 Walkers mammals of the world. Baltimore, MD: JHU Press.

38 Hutterer, R. & Kock, D. 2002 Recent and ancient records of shrews from Syria, with notes on Crocidura katinka Bate, 1937 (Mammalia: Soricidae). Bonner zool.Beitr. 50, 249258.

39 Churchfield, S. 2002 Why are shrews so small? The costs and benefits of small size in northern temperate Sorex species in the context of foraging habits and prey supply. Acta Theriol. 47, 169184. (doi:10.1007/BF03192486)

40 Saint Girons, M. C. 1957 Contribution a‘ la connaissance de la Pachyure ètrusque en captivité. Mammalia 21, 6976. (doi:10.1515/mamm.1957.21.1.69)

41 Geraets, A. 1972 Aktivitätsmuster und Nahrungsbedarf bei Suncus etruscus. Bonn. zool. Beitr. 23, 181196.

42 Vogel, P. 1974 Kälteresistenz und reversible Hypothermie der Etruskerspitzmaus (Suncus etruscus Soricidae, Insectivora). Z. f. Säugetierkunde 35, 173185.

43 Halle, S. 2006 Polyphasic activity patterns in small mammals. Folia Primatol. 77, 1526. (doi:10.1159/000089693)

44 Haberl, W. 1993 Ecology of Austrian shrews in a wetland of the Waldviertel region (Lower Austria) and experimental studies on their behaviour. PhD thesis, University of Vienna.

45 Gould, E., Negus, N. C. & Novick, A. 1964 Evidence for echolocation in shrews. J. Exp. Zool. 156, 1937. (doi:10. 1002/jez.1401560103)

46 Buchler, E. 1976 The use of echolocation by the wandering shrew (Sorex vagrans). Anim. Behav. 24, 858873. (doi:10.1016/S0003-3472(76)80016-4)

47 Tomasi, T. E. 1979 Echolocation by the short-tailed shrew Blarina brevicauda. J. Mammal. 60, 751759. (doi:10.2307/1380190).

48 Thomas, J. A. & Jalili, M. S. 2004 Review of echolocation in insectivores and rodents. In Echolocation in bats and dolphins (eds J. A. Thomas, C. F. Moss & M. Vater). Chicago, IL: University of Chicago Press.

49 Siemers, B. M., Schauermann, G., Turni, H. & von Merten, S. 2009 Why do shrews twitter? Communication or simple echo-based orientation. Biol. Lett 5, 593596. (doi:10.1098/rsbl.2009.0378)

50 von Uexküll, J. 1957 A stroll through the worlds of animals and men: a picture book of invisible worlds. Instinctive behavior: the development of a modern concept (ed. C. H. Schiller), pp. 580. New York, NY: International Universities Press.

51 Comer, C. & Yoshichika, B. 2011 Active touch in orthopteroid insects: behaviours, multisensory substrates and evolution. Phil. Trans. R. Soc. B 366, 30063015. (doi:10.1098/rstb.2011.0149)

52 Gnatzy, W. & Heusslein, R. 1986 Digger wasp against crickets. Naturwissenschaften 73, 212215. (doi:10.1007/BF00417728)

53 Gnatzy, W. & Hustert, R. 1989 Mechanoreceptors in behavior. In Cricket behavior and neurobiology (eds F. Huber, T. E. Moore & W. Loher), pp. 198226. Ithaca, NY: Cornel University Press.

54 Edwards, J. S. & Palka, J. 1974 The cerci and abdominal giant fibres of the house cricket, Acheta domesticus. I. Anatomy and physiology of normal adults. Proc. R. Soc. Lond. B 185, 83103. (doi:10.1098/rspb.1974.0007)

55 Walthall, W. W. & Murphey, R. K. 1986 Positional information, compartments, and the cercal sensory system of crickets. Dev. Biol. 113, 182200. (doi:10.1016/0012-1606(86)90121-1)

56 Miller, J. P., Jacobs, G. A. & Theunissen, F. E. 1991 Representation of sensory information in the cricket cercal sensory system. I. Response properties of the primary interneurons. J. Neurophysiol. 66, 16801689.

57 Theunissen, F. E. & Miller, J. P. 1991 Representation of sensory information in the cricket cercal sensory system. II. Information theoretic calculation of system accuracy and optimal tuning-curve widths of four primary interneurons. J. Neurophysiol. 66, 16901703.

58 Jacobs, G. A., Miller, J. P. & Aldworth, Z. 2008 Computational mechanisms of mechanosensory processing in the cricket. J. Exp. Biol. 211, 18191828. (doi:10.1242/jeb.016402).

59 Gras, H. & Hörner, M. 1992 Wind-evoked escape running of the cricket Gryllus bimaculatus. I. Behavioural analysis. J. Exp. Biol. 171, 189214.

60 Baba, Y. & Shimozawa, T. 1997 Diversity of motor responses initiated by a wind stimulus in the freelymoving cricket, Gryllus bimaculatus. Zool. Sci. 14, 587594. (doi:10.2108/zsj.14.587)

61 Hustert, R. & Gnatzy, W. 1995 The motor program for defensive kicking in crickets: performance and neural control. J. Exp. Biol. 198, 12751283.

62 Jin, T., Witzemann, V. & Brecht, M. 2004 Fiber types of the intrinsic whisker muscle and whisking behavior. J. Neurosci. 24, 33863393. (doi:10.1523/JNEUROS CI.5151-03.2004)

63 Yohro, T. 1977 Structure of the sinus hair follicle in the big-clawed shrew, Sorex unguiculatus. J. Morphol. 153, 333353. (doi:10.1002/jmor.1051530211)

64 Muchlinski, M. N. 2010 A comparative analysis of vibrissa count and infraorbital foramen area in primates and other mammals. J. Hum. Evol. 58, 447473. (doi:10.1016/j.jhevol.2010.01.012)

65 Hyvärinen, H. 1972 On the histology and histochemistry of the snout and vibrissae of the common shrew (Sorex araneus L.). Z. Zellforsch. 124, 445453. (doi:10.1007/BF00335250)

66 Goldschmidt-Lange, U. 1975 Über die morphologischenUnterschiede im Aufbau der facialen Vibrissen einiger Säugetierarten. Zool. Anzeiger 5, 417427.

67 Hyde, J. B. 1957 A comparative study of certain trigeminal components in two soricid shrews, Blarina brevicauda and Sorex cinereus. J. Comp. Neurol. 107, 339351. (doi:10.1002/cne.901070303)

68 Leitch, D. B., Sarko, D. K. & Catania, K. C. 2008 Cortical organization and sensory pathways in the water shrew. Presentation abstract 78.10/OO15. Washington, DC: Society for Neuroscience.

69 Catania, K. C. & Kaas, J. H. 1997 Somatosensory fovea in the star-nosed mole: behavioral use of the star in relation to innervation patterns and cortical representation. J. Comp. Neurol. 387, 215233. (doi:10.1002/(SICI)1096-9861(19971020)387:2,215::AID-CNE4.3.0.CO;2-3)

70 Stolzenburg, J. U., Reichenbach, A. & Neumann, M. 1989 Size and density of glial and neuronal cells within the cerebral neocortex of various insectivorian species. Glia 2, 7884. (doi:10.1002/glia.440020203)

71 Naumann, R. K., Anjum, F., Roth-Alpermann, C. & Brecht, M. 2008 Cytoarchitectonic mapping and quantitative anatomy of the Etruscan shrew cortex. Presentation abstract 370.18/LL24. Washington, DC: Society for Neuroscience.

72 Naumann, R. K., Anjum, F., Roth-Alpermann, C., Brecht, M. 2012 Cytoarchitecture, areas, and neuron numbers of the etruscan shrew cortex. Journal of Comparative Neurology, 520(11), 2512-2530.

73 Wree, A., Lutz, B. & Thole, U. 1992 Volumes of the cytoarchitectonic areas in the rat cerebral cortex. J. Hirnforsch. 33, 545548.

74 Campi, K. L. & Krubitzer, L. 2010 Comparative studies of diurnal and nocturnal rodents: differences in lifestyle result in alterations in cortical field size and number. J. Comp. Neurol. 518, 44914512. (doi:10.1002/cne.22466)

75 Simons, D. J. 1978 Response properties of vibrissa units in rat SI somatosensory neocortex. J. Neurophysiol. 41, 798820.

76 Catania, K. C. & Remple, M. S. 2002 Somatosensory cortex dominated by the representation of teeth in the naked mole-rat brain. Proc. Natl Acad. Sci. USA 99, 56925697. (doi:10.1073/pnas.072097999)

77 Hu, J. & Lewin, G. R. 2006 Mechanosensitive currents in the neurites of cultured mouse sensory neurones. J. Physiol. 577, 815828. (doi:10.1113/jphysiol.2006.117648)

78 Hu, J., Chiang, L. Y., Koch, M. & Lewin, G. R. 2010 Evidence for a protein tether involved in somatic touch. EMBO J. 29, 855867. (doi:10.1038/emboj. 2009.398)

79 Milenkovic, N., Wetzel, C., Moshourab, R. & Lewin, G. R. 2008 Speed and temperature dependences of mechanotransduction in afferent fibers recorded from the mouse saphenous nerve. J. Neurophysiol. 100, 27712783. (doi:10.1152/jn.90799.2008)

80 Avery, R. A., Bedford, J. D. & Newcombe, C. P. 1982 The role of thermoregulation in lizard biology: predatory efficiency in a temperate diurnal basker. Behav. Ecol. Sociobiol. 11, 261267. (doi:10.1007/BF00299303)

81 Klatzky, R. L. & Lederman, S. J. 2011 Haptic object perception: spatial dimensionality and relation to vision. Phil. Trans. R. Soc. B 366, 30973105. (doi:10.1098/rstb.2011.0153)

82 Catania, K. C. 2011 The sense of touch in the star-nosed mole: from mechanoreceptors to the brain. Phil. Trans. R. Soc. B 366, 30163025. (doi:10.1098/rstb. 2011.0128)

Chapter 3

Cytoarchitecture, areas, and neuron numbers of the Etruscan shrew cortex

Published as:

Naumann, R. K., Anjum, F., Roth-Alpermann, C., Brecht, M. (2012). Cytoarchitecture, areas, and neuron numbers of the etruscan shrew cortex. Journal of Comparative Neurology, 520(11), 2512-2530.

Abstract

The Etruscan shrew, Suncus etruscus, is one of the smallest mammals. Etruscan shrews can recognize prey shape with amazing speed and accuracy, based on whisker-mediated tactile cues. Because of its small size quantitative analysis of the Etruscan shrew cortex is more tractable than in other animals. To quantitatively assess the anatomy of the Etruscan shrew's brain we sectioned brains and applied Nissl staining and NeuN (neuronal nuclei) antibody staining. On basis of these stains we estimated the number of neurons of ten cortical hemispheres using Stereoinvestigator and Neurolucida (MBF Bioscience) software. On average the neuron number per hemisphere was found to be $\approx$ 1 million. We also measured cortical surface area and found an average of 11.1 mm^2 (n = 7) and an average volume of 5.3 mm^3 (n = 10) per hemisphere. We identified 13 cortical regions by cytoarchitectonic boundaries in coronal, sagittal, and tangential sections processed for Nissl substance, myelin, cytochrome oxidase, ionic zinc, neurofilaments and vesicular glutamate transporter 2 (VGluT2). The Etruscan shrew is a highly tactile animal with a large somatosensory cortex, which contains a barrel field, but barrels are much less clearly defined than in rodents. The anatomically derived cortical partitioning scheme roughly corresponds to physiologically derived maps of neocortical sensory areas.

3.1 Introduction

The Etruscan shrew (*Suncus etruscus*) is one of the smallest mammals weighing only ≈2 g. Its small body size goes along with (relative to its body size) immense metabolic demands (Vogel, 1974; Jürgens et al., 1996). Etruscan shrews have amazing prey capture abilities allowing them to overwhelm large fast-moving prey. Prey capture is whisker-dependent and based on tactile shape cues. Prey representations are motion- and size-invariant and cricket shape manipulation experiments indicate that shrew behavior is guided by Gestalt-like schemes of prey. Thus, tactile object recognition in Etruscan shrews shares characteristics of human visual object recognition (Anjum et al., 2006), but as in other shrews (Catania et al., 2008) recognition proceeds much faster.

Shrews form the family of Soricidae within the order of Soricomorpha ("shrew-form") (Wilson and Reeder, 2005). There are more than 300 species of shrews; all of them are small, most no more than mouse size. The Etruscan shrew is the smallest shrew and belongs to the subfamily of Crocidurinae (white-toothed shrews). Though outdated (Wilson and Reeder, 2005), the term "insectivore" is still useful to refer to the order encompassing shrews, moles, and hedgehogs due to their similarities in brain size, structure, and scaling (Sarko et al., 2009).

The cytoarchitecture of the cerebral cortex of various shrews was described by Rose (1912), Ryzen and Campbell (1955), and Rehkämper (1981). These authors observed that the shrew cortex is less well differentiated than that of larger mammals and that there are only few neocortical areas. Catania (2005) confirmed the previous cytoarchitectonic observations with cytochrome oxidase histochemistry and could show that there are only four sensory areas in the neocortex of the masked shrew (Sorex cinereus), which are immediately adjacent to each other.

Among all mammals, the Etruscan shrew has the smallest brain and the smallest neocortex (Fons et al., 1984; Stephan et al., 1984; Stephan et al., 1991; Baron et al., 1996). Despite the diminutive absolute size of its brain structures, the Etruscan shrew has a higher relative brain size and higher ratio of neocortex to paleocortex volume (neocorticalization index) than a few other mammals like the Madagascan lesser hedgehog tenrec, Echinops telfairi (Stephan et al., 1991; Morawski et al., 2010).

The scaling of neuron number in mammalian brains is an active research topic with diverging conclusions. Earlier studies have emphasized the uniformity of neuron number below a certain surface area across cortical areas and species (Rockel et al. 1980). More recent work has questioned this conclusion and it was proposed that there is no general rule relating brain volumes and the number of neural elements for all mammals (Herculano-Houzel, 2009). Instead, each order of mammals has a different neuron

Aud	Auditory Cortex
Cing	Cingulate Cortex
Ent	Entorhinal Cortex
Fm	Frontal Medial Cortex
Fr	Frontal Rostral Cortex
Ins	Insular Cortex
Per	Perirhinal Cortex
Pir	Piriform Cortex
Pm	Parietal Medial Cortex
Rsp	Retrosplenial Cortex
Som	Somatosensory Cortex
Tm	Temporal Medial Cortex
Vis	Visual Cortex
CO	Cytochrome oxidase
NeuN	Neuronal Nuclei
NF	Neurofilament
VGluT2	Vesicular Glutamate Transporter 2

TABLE 3.1: Abbreviations.

number to volume relationship (Herculano-Houzel et al., 2006; Herculano-Houzel et al., 2007). Sarko et al. (2009) showed that the insectivore cortex scales similar to that of the rodent cortex in that larger cortices contain fewer neurons than expected from a linearly scaled up small insectivore cortex. Stolzenburg et al. (1989) counted neurons in vertical columns through somatosensory cortex of the Etruscan shrew and other insectivores and found that there is an inverse relationship between neuronal density and cortex thickness. Collins et al. (2010) mapped varying neuronal densities across the entire cerebral cortex in their study of different primate species.

In this study we aim to estimate neuron number across all regions of Etruscan shrew cortex using a stereological approach which is more easily combined with classical studies of cytoarchitecture and chemoarchitecture. To this end, we first describe the physical characteristics of the Etruscan shrew brain. Second, we derive a cytoarchitectonic partitioning scheme of the Etruscan shrew cortex by using histochemical (cytochrome oxidase, myelin, ionic zinc) and immunohistochemical markers (neurofilaments, vesicular glutamate transporter 2 [VGluT2]). Third, we used stereological methods to estimate neuron numbers in identified cortical regions and the entire Etruscan shrew cortex. Finally, we discuss our results in the context of recent electrophysiological mapping experiments on Etruscan shrews' cerebral cortex (Roth-Alpermann et al., 2010), to address the question of mammalian cortical scaling.

3.2 Materials and Methods

3.2.1 Animals and tissue

In this study we included 25 Etruscan shrews (Suncus etruscus). We used 10 female and 11 male animals; for 4 animals sex was not known. All experimental procedures were performed according to German guidelines on animal welfare under the supervision of local ethics committees. Shrews were housed in terraria containing a layer of dry soil, moss, stones, pieces of wood, and broken flowerpots. The diet consisted of crickets, mealworms, and water ad libitum. Breeding terraria contained a large block of plaster containing a system of tunnels and potential breeding chambers (see Anjum et al. 2006 for details).

All animals were euthanized by an overdose of isoflurane. The animals were perfused transcardially with 0.9 % saline followed by 4 % paraformaldehyde in 0.1 M phosphate buffer (PB). For zinc histochemistry animals were perfused in sequence, with saline, saline containing 0.1% sodium sulfide and 4% paraformaldehyde in 0.1 M PB. The brains were removed from the skull and postfixed overnight in 4 % paraformaldehyde in 0.1 M PB. The hemispheres were immersed in 30 % sucrose solution for cryoprotection until they sank to the bottom of the vial. Eighteen brains were embedded in a mixture of egg yolk and 30 % sucrose supplemented by 0.75 ml glutaraldehyde and mounted on a cryostat (Leica 2035 Biocut) to obtain 30- or 40-μm-thick coronal (11), sagittal (1), or tangential sections parallel to the pia (6).

Thirteen brains were used for quantitative studies. Seven brains from this group were used for counting neurons, surface area, and volumes and measuring brain weight. For two of these brains data on brain weight were not available. To assess brain weights more precisely, we weighed another six brains, adding up to a total of 11 brain weight measurements. In three of the seven brains used for counting we estimated neuron number and volume for both hemispheres, for a total of ten measurements (Table 3.3). The neuron number of individual cortical regions was estimated in three brains. The seven brains used for counting were stained for the following markers: NeuN (one), alternating for Nissl substance, myelin, and cytochrome oxidase (three), and only for Nissl substance (three).

One brain was not perfused and is shown in Figure 3.1. Additionally, 11 brains were used for cytoarchitectonic and histochemical studies. Five brains of this group were stained for immunohistochemical markers (one for neurofilaments, and four for VGluT2). The other six brains were stained for cytochrome oxidase (two), myelin (one), and synaptic zinc (three).

3.2.2 Histochemistry

Sections were processed for Nissl substance, cytochrome oxidase (Wong-Riley, 1979), myelin, and synaptic zinc. For the myelin staining a variation of the gold-chloride protocol was used (Schmued, 1990). Briefly, free-floating cryostat sections were incubated for 2-4 hours in a 0.1 % solution of gold chloride in 0.02 M PB, pH 7.4, and 0.9 % sodium chloride. After staining, sections were rinsed for 5 min, fixed for 5 min in a 2.5 % solution of sodium thiosulfate, and rinsed again for 30 min before mounting with Mowiol. After perfusion with a solution containing sodium sulfide, brain sections to be stained for synaptic zinc were washed thoroughly with 0.1 M PB, followed by 0.01 M PB. For the visualisation of synaptic zinc, sections were developed as described by Danscher (1981). In brief, sections were exposed to a solution containing gum arabic, citrate buffer, hydroquinone and silver lactate for 60-120 minutes, in the dark at room temperature. Development of reaction products was checked under a microscope and terminated by rinsing the sections in 0.01 M PB and, subsequently, several times in 0.1 M PB (Ichinohe and Rockland, 2004).

3.2.3 Immunohistochemistry / antibody characterization

One series of tangential sections was stained for neurofilaments with Anti-Neurofilament 160/200 antibodies (NF-200). This purified monoclonal (Clone RMdO20) antibody (Sigma-Aldrich, Catalog Nr. N2912) which we used at a dilution of 1:1,000 was raised against purified mid-size rat neurofilament (NF-M) subunit. It recognizes mainly the non-phosphorylated form of NF-M and NF-H, NF-M/H, ≈160 and 200 kDa (manufacturer's technical information). Staining of sections through the cerebral cortex produced a pattern of neurofilament staining reminiscent of previous descriptions in other species (Boire et al., 2005; Wong and Kaas 2008).

One series of coronal sections was stained for neuronal nuclei with mouse anti-neuronal nuclei I (NeuN) antibody. This purified monoclonal (Clone A60) antibody (Chemicon, Catalog Nr. MAB377, Lot Nr. LV1427917) which we used at a dilution of 1:1,000 was raised against purified cell nuclei from mouse brain. A previous lot of this antibody recognized two-three bands in the 46-48 kDa range and possibly another band at approximately 66 kDa (manufacturer's technical information). Staining of sections through the cerebral cortex produced a pattern of neuronal nuclei as expected from previous descriptions (Lind et al., 2005).

One series of sagittal sections, two series of coronal sections (alternating with cytochrome oxidase staining), and one series of tangential sections were stained for VGluT2 with

mouse anti-vesicular glutatamate transporter 2 (VGluT2) antibody. This purified monoclonal antibody (Chemicon, Catalog Nr. MAB5504, Lot Nr. LV1761053) which we used at a dilution of 1:1,000 was raised against the full-sequence recombinant rat VGluT2 protein. VGluT2 is a marker thalamocortical projections to sensory cortex (Fujiyama et al., 2001) and the staining pattern in cerebral cortex corresponds to what would be expected from previous studies using this antibody in other species (Wong and Kaas, 2008) and previous studies of thalamocortical projections in insectivores (Ebner, 1969; Valverde et al., 1986).

Sections were processed for NeuN and NF-200 and VGluT2 according to the protocol described in Wong and Kaas (2008). Briefly, sections were incubated in a blocker of 0.1 M phosphate-buffered saline (PBS), pH 7.2, with 0.5 % Triton X-100 and 5 % normal horse serum for 1 hour at room temperature before incubation in their respective primary antibodies (see description in text and Table 3.2) in the blocker for 48 hours at 4 °C. After rinsing, the sections were incubated in the blocker containing biotinylated horse anti-mouse/anti rabbit IgG (Vector, Burlingame, Catalog Nr. BA-1400, Lot Nr. U0417, produced in horse; 1:200) for 90 min at room temperature followed by ABC incubation (one drop each of reagent A and B per 7 ml of 0.1 M PB, pH 7.2; ABC kits, Vector, Burlingame) for 90 min, also at room temperature. Immunoreactivity was visualized by developing sections with diaminobenzidine histochemistry.

3.2.4 Light microscopy and anatomical reconstruction

Cortical region boundaries were detected by laminar and cell density changes in the sections that were processed for Nissl substance and a variety of histochemical markers. To distinguish cortical regions, Nissl sections were examined for absolute thickness of the cortex, thickness of the cortical layers, cell density in one or several layers, and cell size and shape. Histochemical stains were evaluated for staining pattern and intensity. In general, the different histological procedures revealed almost identical boundaries. Processed sections were viewed with StereoInvestigator software (MBF Bioscience, Williston, VT) employing an Olympus (Tokyo, Japan) BX51 microscope with an MBFCX9000 camera (MBF Bioscience) mounted on the microscope. The microscope was equipped with a motorized stage (LUDL Electronics, Hawthorne, NY) and a z-encoder (Heidenhain, Schaumburg, IL). StereoInvestigator software was used for stereological procedures and acquiring images. Digitized images were adjusted for brightness and contrast by using Adobe Photoshop (Adobe Systems, San Jose, CA), but they were not otherwise altered.

Name	Species	Catalog No., Lot No.	Immunogen	Supplier	Dilution	Specificity
Anti-Neurofilament 160/200	Mouse, monoclonal (Clone RMdO20)	N2912, 035K4754	purified mid-size rat neurofilament (NF-M) subunit	Sigma-Aldrich, St. Louis, MO	1:1000	Manufacturer
Anti-NeuN	Mouse, monoclonal (Clone A60)	MAB377, LV1427917	purified cell nuclei from mouse brain	Chemicon (now part of Millipore, Billerica, MA)	1:1000	Manufacturer
Anti-VGluT2	Mouse, monoclonal (Clone 8G9.2)	MAB5504, LV1761053	full-sequence recombinant rat VGluT2 protein	Chemicon	1:1000	Manufacturer

TABLE 3.2: Primary Antibodies Used in this Study

3.2.5 Stereology

In our analysis of total neuron numbers we included the entire neocortex and the entorhinal and piriform cortices. For analysis of individual cortical regions the neocortex was further subdivided into 11 regions plus the entorhinal and the piriform cortex. Cortical regions were identified and outlined at low magnifications. Neurons were identified in Nissl stained sections by their shape and staining intensity, two hemispheres stained for NeuN were included to control for misclassification of neurons in Nissl stained sections. Cortical neurons were individually counted using StereoInvestigator software on available Nissl-stained sections using high power magnification in 15-20 sections per hemisphere (Table 3.3). We employed a standard stereological sampling scheme called the optical fractionator method which is independent of volume measurements and shrinkage since the number of neurons is estimated directly without referring to neuron densities. The optical fractionator technique is performed by counting nucleoli in a known fraction of the entire region of interest. Optical disectors are randomly placed on a series of sections and used to count the number of particles (nucleoli) which come into focus and fall within the acceptance lines of the disector (Howard and Reed, 2005; West and Gundersen, 1990; West et al., 1991). This technique is the most commonly used unbiased estimation method partly because tissue shrinkage should not affect the total estimates.

Specimen ID	Hemisphere	Sex	Cut section thickness (μm)	Evaluated series	No. of cortex sections evaluated
Sh1	U	U	30	1:5	18
Sh2	L	U	30	1:5	20
Sh2	R	U	30	1:5	20
Sh3	L	U	30	1:6	15
Sh3	R	U	30	1:6	15
NeuN	L	U	30	1:6	16
NeuN	R	U	30	1:6	16
Sh180	L	F	40	1:6	15
Sh293	L	M	40	1:6	15
Sh294	R	M	40	1:6	15

TABLE 3.3: Characteristics of the 10 Etruscan Shrews Analyzed. U, unknown; L, left; r, right.

We used 10x10, 15x15, and 20x20 μm^2 counting frames. With these frames we counted on average 0.58 - 2.67 neurons per frame. The counting frame of 15x15 μm^2 size allowed counting on average between 1 and 2 neurons per counting frame which is considered optimal for this counting procedure (Howard and Reed, 2005). More than 400 neurons were counted for assessing the total number of neurons in each cerebral hemisphere. For counting of individual regions, approximately 200 (Howard and Reed, 2005) neurons were counted on average in an area of interest (mean 186).

In seven hemispheres sectioned coronally at 30 μm thickness and stained for Nissl substance (five) and NeuN (two) we estimated the total number of neurons. The cortex was contained in on average 120 sections, 1/5 or 1/6 of which were chosen by systematic random sampling. We used square counting frames of 10 μm or 20 μm side length and square sampling grids of 150 μm to 300 μm side lengths, resulting in an area sampling fraction of 1/225. The thickness of the mounted sections was measured in advance and found to be not less than 8-10 μm. A guard zone of 1 μm above and below the counting volume was used. Guard zones are regions in the z-axis that form the upper and lower boundaries for the counting volume, neurons falling within these zones are not counted. The thickness sampling fraction was therefore 3/4 or 4/5.

For estimating the number of neurons in individual regions of the cortex we used 3 additional hemispheres cut into 40-μm-thick coronal sections stained alternatingly for Nissl substance, cytochrome oxidase and myelin. Cytochrome oxidase staining allowed to identify sensory cortex. Myelin staining additionally helped to map piriform, entorhinal, and frontal rostral cortex. Other regions of cortex were identified by cytoarchitecture and absence of cytochrome oxidase or myelin staining. The cortex was represented on average on 90 sections, 1/6 of which were chosen by systematic random sampling. We used a

sampling grid of 100 μm side length, resulting in an area sampling fraction of 9/400. The mounted thickness was not less than 25 μm, so a guard zone of 5 μm above and below the counting volume with a height of 15 μm could be used. The thickness sampling fraction was therefore 3/5. The coefficient of error (CE) was calculated according to Gundersen et al. (1999).

We measured neocortical thickness perpendicular to the surface of three brains in Nissl-stained coronal sections of three brains in 498 positions. We took three measurements at each site perpendicular to surface and recorded the mean value. Mean cortical thickness for three animals was not significantly different; therefore measurements were aligned at the intersection of the midline and the line separating the olfactory bulbs from cortex. The measurements were plotted onto a grid with a field size of 120 x 120 μm and spatially filtered with a Gaussian kernel. In a fraction of these sites (186) we additionally measured the thickness of cortical layer 1. For total thickness, we provide raw data uncorrected for shrinkage (in the x-y plane) due to histological processing. Layer 1 thickness is given as relative percentage, which should be less affected by shrinkage effects. For each position we noted the cortical region. The plane of a coronal section is often close to a true perpendicular section but this is not accurate in the frontal and occipital poles of the cortex (Braitenberg and Schüz, 1998). Therefore measurements of thickness in these regions will be less accurate. The cortical surface was measured by drawing lines along the extent of layer 2 of the cortex. The sum of all these lines was multiplied by the section thickness and divided by the section sampling fraction to arrive at an estimate for the cortical surface area. The volume was measured using the Cavalieri estimator associated with the optical fractionator counting procedure.

3.3 Results

3.3.1 Macroscopic characteristics of the Etruscan shrew brain

Etruscan shrews have a lissencephalic brain. The cortex covers the dorsal and lateral surface of the brain but not the cerebellum and the colliculi (Fig. 3.1A; Stephan, 1956; Stephan et al, 1991). The brain is remarkably small, with an overall brain weight of only 64.4 ± 5.2 mg (n = 11 brains). Per hemisphere we measured a surface area of 11.1 ± 2.3 mm^2 (n = 7 hemispheres) and a cortical volume of 5.3 ± 1.4 mm^3 (n = 10 hemispheres).

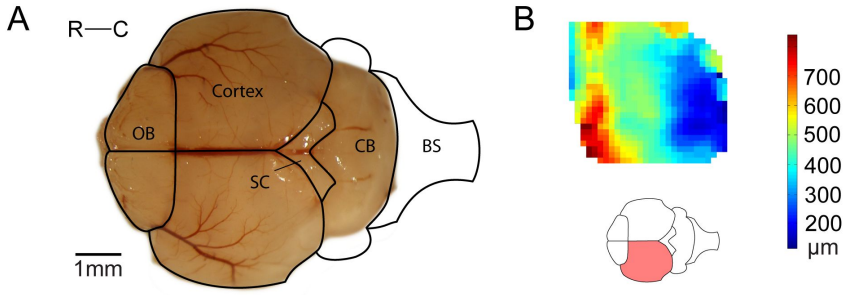

FIGURE 3.1: The Etruscan shrew brain and cortical thickness. (A) Dorsal view of the Etruscan shrew brain. Black lines outline major brain regions, from left to right: olfactory bulbs (OB), cerebral cortex, superior colliculus (SC), cerebellum (CB), and brainstem (BS). Some parts of the cerebellum and the brain stem seen in the line drawing are not visible on the photograph as they are usually lost in the preparation of the brain from the skull. R = rostral. C = caudal. (B) Dorsal view of the left hemisphere, showing the thickness of the cortex at each point. Lower inset: the red area indicates the location of the section shown. Right inset: the color code indicates the thickness of the neocortex measured perpendicular to the surface in μm, from blue (thin) to red (thick).

We measured the thickness of the cortex in Nissl stained sections of three shrews (Sh293, Sh294, Sh180) at 498 locations (Fig. 3.1B, Table 3.5). The mean of all measurements is 435 μm, with a standard deviation of 159 μm (not corrected for shrinkage). The cortex is especially thick in piriform cortex (mean = 586 μm) and very thin in posterior parts of cortex for example in visual cortex (mean = 310 μm). We find that in neocortical sensory areas, the cortex is often thicker than in neighboring regions. In 186 locations we also measured the extent of cortical layer 1. On average layer 1 takes up 26 % of the cortical thickness. There is large variability of relative layer 1 extent for different cortical regions (Table 3.5). Layer 1 is relatively thin in sensory neocortex (e.g. somatosensory cortex, 21 %). In lateral parts of cortex (e.g. piriform cortex, 31 %) layer 1 is relatively wider compared to medial parts (e.g. cingulate cortex, 21 %).

3.3.2 General remarks on the cortical architecture of the Etruscan shrew

As in other mammals the cortex of the Etruscan shrew is a cytoarchitectonically heterogeneous sheet of tissue. The presence of distinct subdivision of cortex is suggested by the fact that different staining methods (Nissl, cytochrome oxidase activity, myelin, VGluT2, synaptic zinc) indicate the same borders (see below). As shown previously (Rose, 1912; Rehkämper, 1981), we found that layer 1 of the cortex of the Etruscan shrew is very thick relative to the total thickness of the cortex. Also, layer 2 is always easy to distinguish from other layers in Nissl stainings. It is very thin and contains a high density of darkly stained neurons. This has been called the "accentuated layer 2" and is found in a variety of mammals including bats, shrews, hedgehogs, and marsupials (Sanides, 1972; Ferrer, 1986). Layer 4 is best defined by the staining pattern of cytochrome oxidase, VGluT2, and the absence of staining for synaptic zinc. The deeper layers are easier to define in Nissl stainings but also do not show clear sublayers. In layer 5 no giant pyramidal cells could be found - presumably shrews have only a very small motor cortex (Nudo and Masterton, 1990). Cytochrome oxidase did not stain any allocortical region strongly.

It was much easier to identify non-neocortical regions by cytoarchitecture. They share more cytoarchitectonic features with cortices of well-studied animals like mice than the neocortical areas. In Nissl stained sections the entorhinal and piriform cortex stand out by their characteristic cytoarchitectonic pattern. VGluT2 immunoreactivity marks thalamocortical axon terminals (Fujiyama et al., 2001). Therefore it is expressed primarily in layer 4 of neocortical primary sensory areas but also in the frontal rostral cortex and entorhinal cortex. Staining for synaptic zinc reveals the distribution of unbound ionic zinc contained in synaptic vesicles in the brain (Danscher, 1981). Zinc is present in synaptic vesicles of corticocortical neuron terminations but absent in terminations of thalamocortical projection neurons (Wong and Kaas, 2008). For example, staining for synaptic zinc is most pronounced in perirhinal and insular cortex but absent in layer 4 of sensory neocortex and frontal rostral cortex. The histological evidence provided in the following paragraphs was used to identify cortical regions for further quantitative study of the entire cortical sheet.

3.3.3 Overview of sensory and frontal cortices in tangential sections

Tangential sections stained for cytochrome oxidase (Fig. 3.2A), neurofilaments (Fig. 3.2B), synaptic zinc (Fig. 3.2C), and myelin (Fig. 3.2D) allow for a basic subdivision of the cerebral cortex. They show a similar arrangement of sensory neocortical and frontal

regions. Staining for synaptic zinc allows to locate further cortical regions, e.g. perirhinal cortex is very dark compared to neighboring regions (Fig. 3.2C). The frontal pole of the cortex contains one region staining strongly for cytochrome oxidase, neurofilament, and myelin (Figs. 3.2A, 3.2B, 3.2D): the frontal rostral cortex. This region likely receives thalamic afferents (absence of zinc staining in middle layers) and probably corresponds to ventral orbitofrontal cortex. In other shrews (Catania et al., 1999), hedgehogs (Kaas et al., 1970), and opossums (Wong and Kaas, 2009) there is an area staining strongly for cytochrome oxidase or myelin in a similar frontal position. The frontal medial cortex stains only weakly for cytochrome oxidase (Fig. 3.2A), neurofilaments (Fig. 3.2B), and myelin (Fig. 3.2D). It is in between frontal rostral cortex and somatosensory cortex (Fig. 3.2C).

The largest stained area in Figure 3.2A in the center of the cortex is most likely the somatosensory cortex. The two smaller areas caudal to somatosensory cortex have been tentatively identified as the auditory and visual cortical areas. The auditory cortex forms an almost round stained area posterior to the somatosensory cortex. It stains strongly for cytochrome oxidase (Fig. 3.2A) and neurofilaments (Fig. 3.2B). The border between the somatosensory and auditory areas is difficult to define in tangential sections. The visual cortex forms a thin stripe extending in rostro-caudal direction in the caudal part of the cortex. It stains strongly for cytochrome oxidase (Fig. 3.2A) and neurofilaments (Fig. 3.2B). Both visual and auditory cortex lack staining for synaptic zinc compared to neighboring regions (Fig. 3.2C).

3.3.4 Borders of sensory cortical areas

Medial to somatosensory cortex is a smaller area we termed parietal medial cortex. This region stains less strong for myelin (Fig. 3.3A) and cytochrome oxidase (Fig. 3.3B). Layer 1 is wider, and layer 2 is more densely packed in parietal medial cortex (Fig. 3.3C). Posterior to this cortical region, the somatosensory cortex is at one point very close to visual cortex, as shown by VGluT2-staining in Figure 3.3D. Nissl staining shows an increase in layer 1 thickness in the transition from somatosensory cortex to visual cortex (Fig. 3.3E). The somatosensory cortex is the region with the thinnest layer 1 (21 % relative thickness). At the lateral border of somatosensory cortex, myelin staining almost completely disappears (Fig. 3.3F). This is the border to insular cortex. In insular cortex, layer 1 increases in thickness from medial to lateral, whereas the appearance of layer 2 does not change dramatically (Fig. 3.3G).

The auditory and visual cortex are separated by a region we termed temporal medial cortex. Auditory cortex and visual cortex show strong staining for myelin and cytochrome

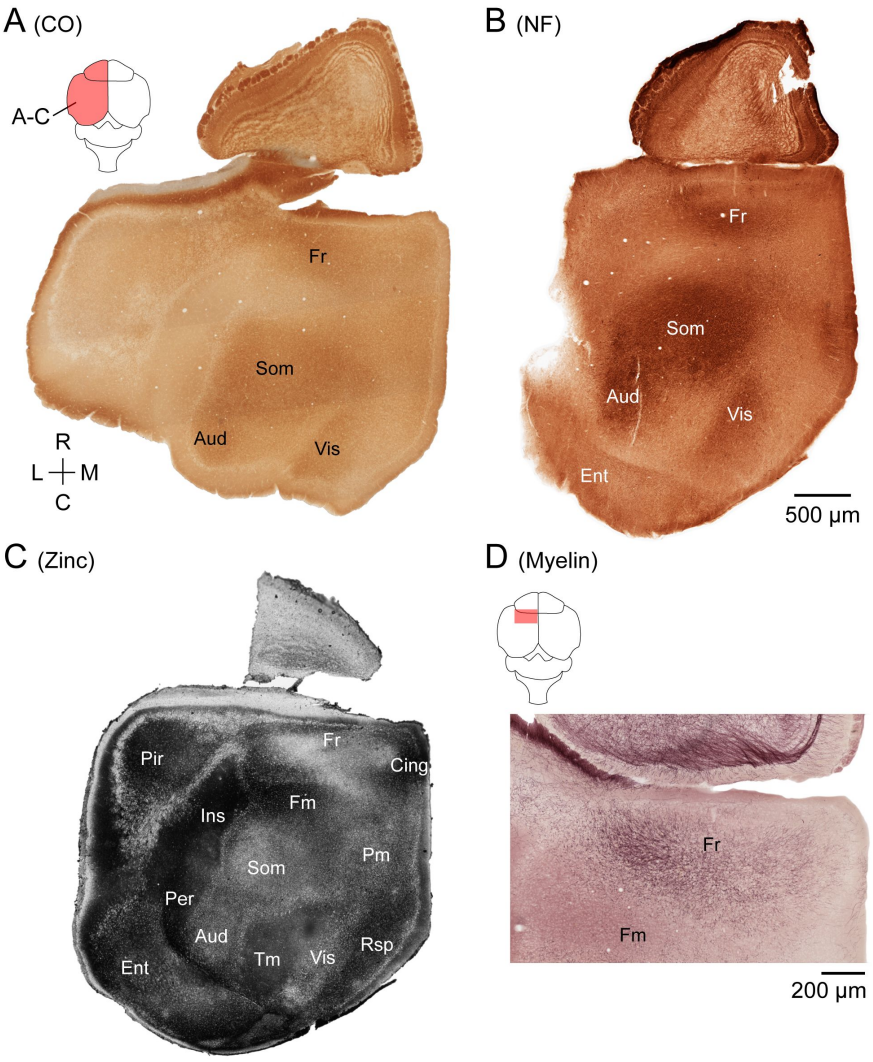

FIGURE 3.2: Flatmount preparation, stained for cytochrome oxidase activity, neurofilaments (NF-200), synaptic zinc and myelin. Sections of flattened cortex processed for (A) cytochrome oxidase, (B) NF-200, (C) synaptic zinc, and (D) myelin to reveal the subdivisions of cortex. Inset in (C): the red area indicates the location of the tangential section shown in (A), (B), and (C). Inset in (D): the red area indicates the location of the tangential section shown in (D). We indicate the location of cortical regions if they can be differentiated from neighboring regions. In (A) and (B) the large, dark staining region in the central part of the cortex contains the somatosensory area. Just medial to the somatosensory area, a small stripe of cortex is located in an area appropriate for the visual cortex. Caudal to the somatosensory area, a round spot of dark tissue marks the extent of auditory cortex. The scale bar in panel (B) also applies to (A) and (C). R = rostral. C = caudal. L = lateral. M = medial. For other abbreviations, see list. Scale bar in A = 500 μmm (applies to AC); 200 μmm in D.

oxidase whereas temporal medial cortex does not (Figs. 3.3H, 3.3I). In posterior sensory cortex the area stained for cytochrome oxidase appears to reach the cell dense layer 2 (Fig. 3.3I), therefore it is often difficult to distinguish layer 3 and 4. Layer 1 is relatively thin and layer 2 less densely packed with cells in the sensory cortex compared to temporal medial cortex (Fig. 3.3J). Also, we did not find subdivisions of layer 4 in visual cortex (Fig. 3.3J). Staining for synaptic zinc shows the sensory areas by their lack of staining in layer 4 (Fig. 3.3K). The lateral border of auditory cortex is formed by perirhinal cortex, which shows a much stronger staining for synaptic zinc throughout all layers (Fig. 3.3K).

3.3.5 Somatosensory cortex of the Etruscan shrew

The center of somatosensory cortex shows a weakly inhomogeneous, patchy cytochrome oxidase, VGluT2, and synaptic zinc staining compared to more lateral and medial parts of somatosensory cortex (Fig. 3.4A, 3.4B, 3.4C). This is reflected by the staining pattern in coronal sections (Fig. 3.4D, 3.4E, 3.4F) but is different from the clear structural arrangement of the barrel cortex of rodents. According to our electrophysiological mapping experiments (Roth-Alpermann et al., 2010) these parts correspond to the whisker representation of the somatosensory cortex. We suggest it is highly likely that the patches weakly visible in Figs. 3.4D, 3.4E correspond to 'barrels' (patches of cells preferentially representing one whisker), but that these 'barrels' are much less clearly defined than in rodents.

3.3.6 Cytoarchitectonics of anterior regions

We defined sensory cortical areas and their borders on the basis of a combination of markers and stains. We first present the cytoarchitectonics of the anterior cortex (Fig. 3.5A-C). Some regions of cortex are often defined by a lack of a certain marker like cytochrome oxidase compared to their neighboring regions or by a specific type of cytoarchitecture. For example, piriform cortex is characterized by its three-layer architecture, wide layer 1, and densely packed layer 2 (Fig. 3.5C), as in the cortex of the mouse. Its layer 1 is split into an outer part, which is crossed by myelinated fibers (Fig. 3.5A) and stains strongly for cytochrome oxidase (Fig. 3.5B) and an inner part, which does not share these features. Piriform cortex is located on the lateral wall of the cortical mantle and spans more than half of the rostro-caudal extent of the cortex (Fig. 3.2C). The piriform cortex is very thick compared to other regions. Its relative layer 1 thickness (33 %) is among the highest in the shrew cortex.

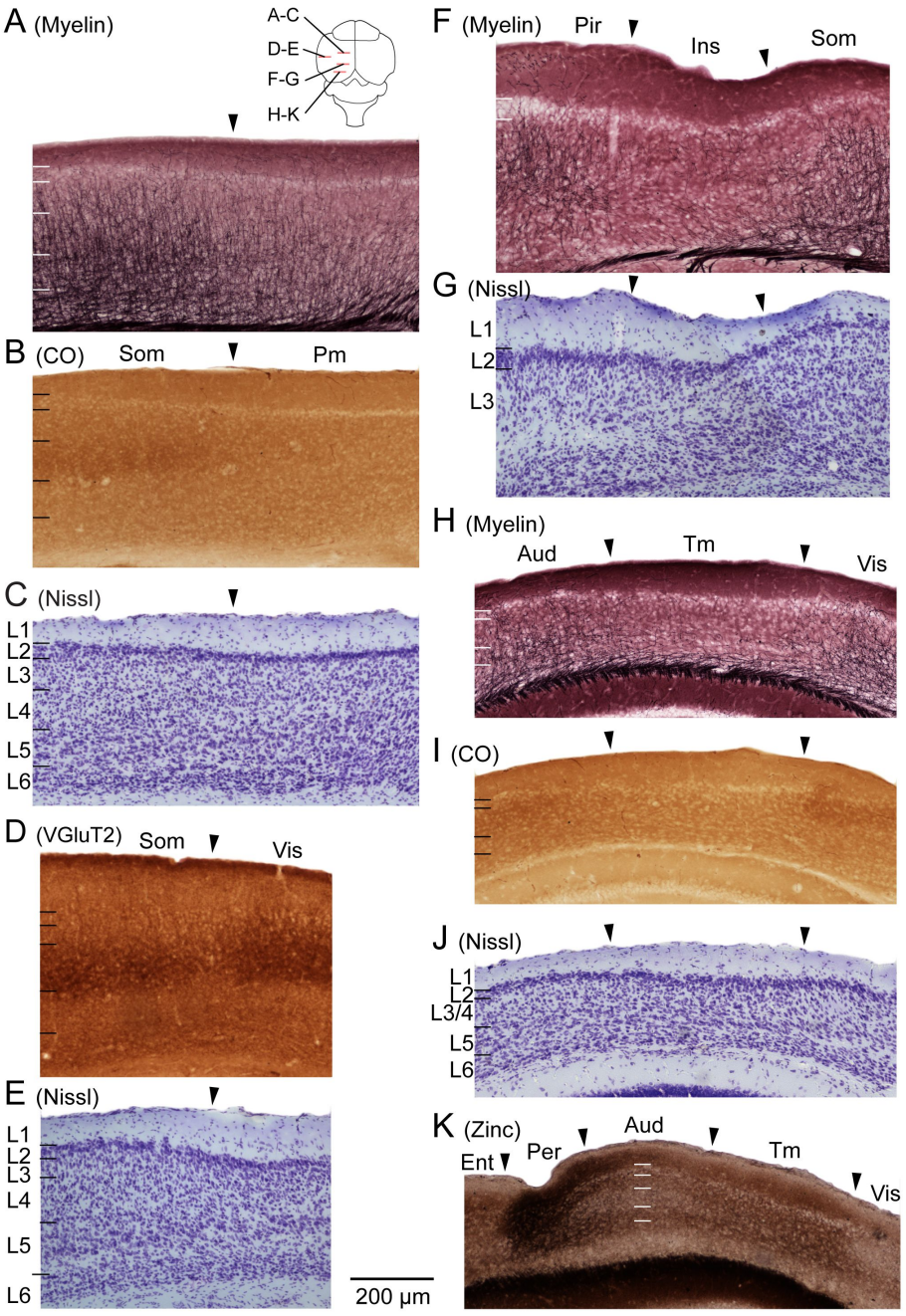

FIGURE 3.3: High magnification views of different borders of sensory cortical areas. Borders of sensory cortical areas visualized in coronal sections stained for Nissl, cytochrome oxidase activity, myelin, VGluT2, and synaptic zinc. Border of somatosensory cortex and parietal medial cortex shown by staining for myelin (A), cytochrome oxidase (B), and Nissl substance (C). Border of somatosensory cortex and visual cortex shown by staining for VGluT2 (D) and Nissl substance (E). Border of somatosensory and insular cortex shown by staining for myelin (F) and Nissl substance (G). Borders auf of auditory, temporal medial, and visual cortex shown by staining for myelin (H), cytochrome oxidase (I), Nissl substance (J), and synaptic zinc (K). Inset in (F): the red bar indicates the location of the coronal sections shown.

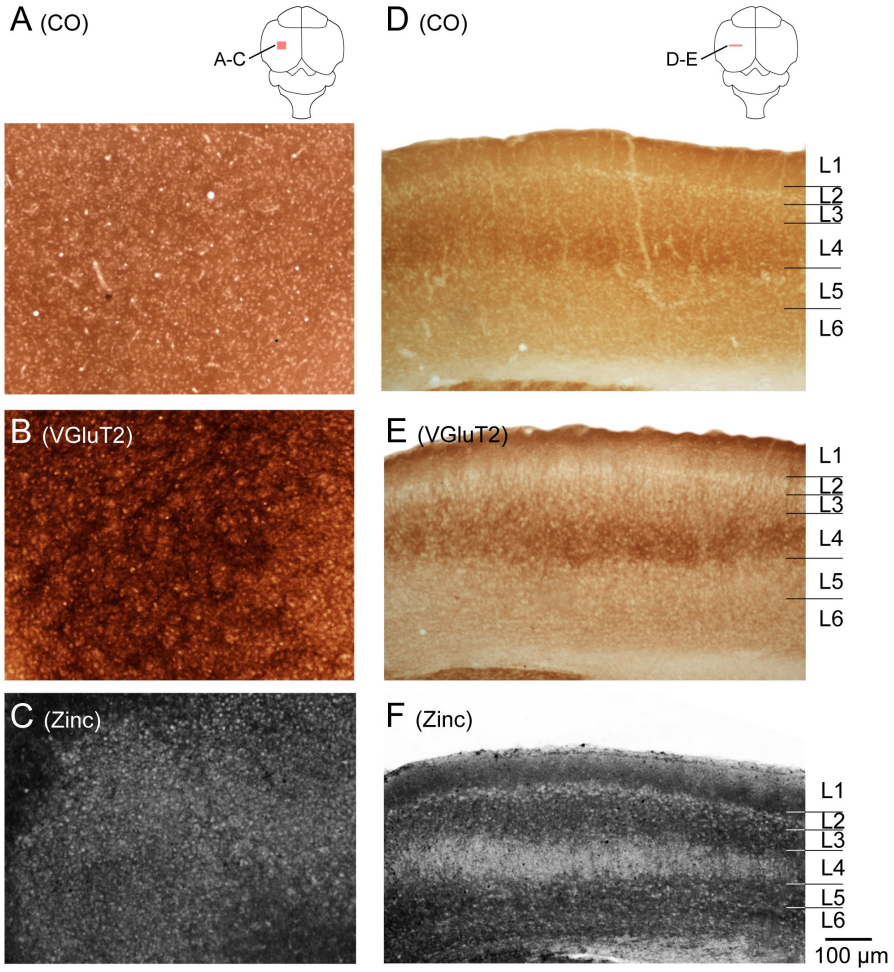

FIGURE 3.4: High magnification views of somatosensory cortex. Tangential and coronal sections of somatosensory cortex. Sections of flattened cortex (A), (B), (C) and coronal sections (D), (E), (F) were processed for cytochrome oxidase, VGluT2, and synaptic zinc. No clear barrel structure as in rodents is evident. Inset in (B): the red area indicates the location of the tangential section shown in (A), (B), and (C). Inset in (E): the red area indicates the location of the coronal section shown in (D), (E), and (F).

The transition from piriform cortex to insular cortex is characterized by several prominent cytoarchitectonic changes such as a decrease in myelination (Fig. 3.5A) and cytochrome oxidase activity in layer 1 (Fig. 3.5B) Also, the insular cortex is marked by dark staining for synaptic zinc compared to neighboring cortex (Fig. 3.2C). It is characterized by an indentation of layer 2 that is often larger and not at the same position as the indentation due to the rhinal fissure (Fig. 3.5C). The insular cortex has a lower packing density of cells in layer 2 (Fig. 3.5C). This lower density in layer 2 is shared by somatosensory cortex (Fig. 3.5C), which is the largest area of the neocortex (Fig. 3.5B). It is the thickest of all sensory areas and has a distinct lamination pattern (Fig. 3.5C). It has very dense cytochrome oxidase staining, particularly in layer 4 (Fig. 3.5B). This staining is more intense in the medial part of somatosensory cortex than in the lateral part (Fig. 3.5B). In the lateral part of the somatosensory cortex the cytochrome oxidase

band is located closer to the surface (Fig. 3.5B).

The parietal medial cortex has a denser layer 2 than the lateral somatosensory cortex and the medial cingulate cortex (Fig. 3.5C). The parietal medial cortex shows no or only weak staining for cytochrome oxidase (Fig. 3.5B) which probably correlates with a decrease of the density of cells in layer 4 compared to somatosensory cortex (Fig. 3.5C). In cingulate cortex staining for cytochrome oxidase (and likely layer 4) are absent (Fig. 3.5B). Cingulate cortex has a relatively thin layer 1 compared to other cortical regions. In general, relative layer 1 thickness increases from medial to lateral cortical regions. Also, frontal regions are thicker than posterior regions of cortex. Piriform, insular, frontal medial, and cingulate cortex have an average thickness of more than 500 μm (Table 3.5).

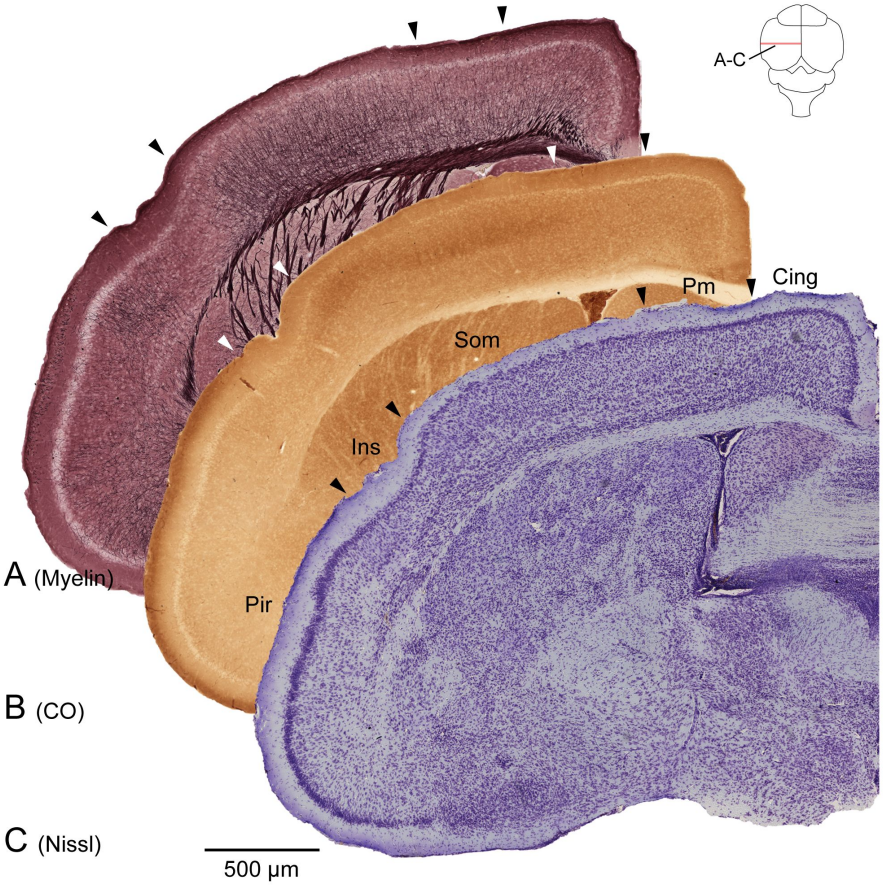

FIGURE 3.5: Cytoarchitectonics of anterior parts of shrew cortex. Architectonic characteristics of the Etruscan shrew cortex shown in 3 adjacent coronal sections. Adjacent coronal sections were processed for myelin (A), cytochrome oxidase (B), and Nissl substance (C). The boundaries of proposed cortical areas are shown superimposed on the sections. Inset: the red bar indicates the location of the coronal sections shown. Arrowheads mark region borders.

3.3.7 Cytoarchitectonics of middle parts of shrew cortex

We next present the cytoarchitectonics of middle parts of shrew cortex, where the shrew brain has its maximal width (Fig. 3.6A-C). Medial and caudal to the piriform cortex on the lateral wall of the cortex is the entorhinal cortex (Figs. 3.6A, 3.6B, 3.6C). The entorhinal cortex is thin and is subdivided into two clear cell-rich layers (layer 2/3 and layer 5/6) separated by the cell-poor layer 4 (Fig. 3.6C). Radial bundles of myelinated fibers extend from layer 5/6 through layer 4 in the entorhinal cortex (Fig. 3.6A). The perirhinal cortex forms a narrow strip of thin cortex between entorhinal cortex, the posterior somatosensory cortex, and auditory cortex (Figs. 3.6C). Perirhinal cortex is easily recognized by its lack of staining myelin preparations (Fig. 3.6A) and its intense staining for synaptic zinc compared to neighboring regions (Figs. 3.3K). With an average thickness of around 250 μm the perirhinal cortex is the thinnest part of the cerebral cortex. At the same time, layer 1 is very wide compared to the other layers in perirhinal cortex.

The rostro-caudal transition from retrosplenial to cingulate cortex is gradual. At one point, but not along the entire extent of visual cortex, there is very little intervening space between somatosensory and the frontal part of visual cortex (Fig. 3.3D). Anterior to that point, parietal medial cortex forms a thin wedge between somatosensory and visual cortex (Figs. 3.6A, 3.6B, 3.6C). The most medial region shown in Figure 3.6 is the retrosplenial cortex. It forms the caudal part of the medial wall of the cortex and is characterized by its accentuated layer 2. Also, the retrosplenial cortex has a strong myelination in the lower layers (Fig. 3.6A).

3.3.8 Cytoarchitectonics of posterior regions

The caudal parts of shrew cortex are illustrated in Fig. 3.7. Figure 3.7A shows that the caudal part of the entorhinal cortex contains no myelinated radial bundles. The entorhinal and perirhinal cortices are very thin, in the most caudal parts of the brain often less than 200 μm (Fig. 3.7C). The auditory and visual cortices are also very thin, but they are marked by intense cytochrome oxidase staining in the upper cortical layers (Fig. 3.7B) and increased myelination in the lower layers (Fig. 3.7C). Also, note the large size of the hippocampus relative to the cerebral cortex (Fig. 3.7C).

3.3.9 Cytoarchitectonic divisions visualized in sagittal sections

Sagittal sections from the lateral part of shrew cortex stained for VGluT2 demonstrate the gradual transition from auditory to somatosensory cortex (Fig. 3.8A). The transition

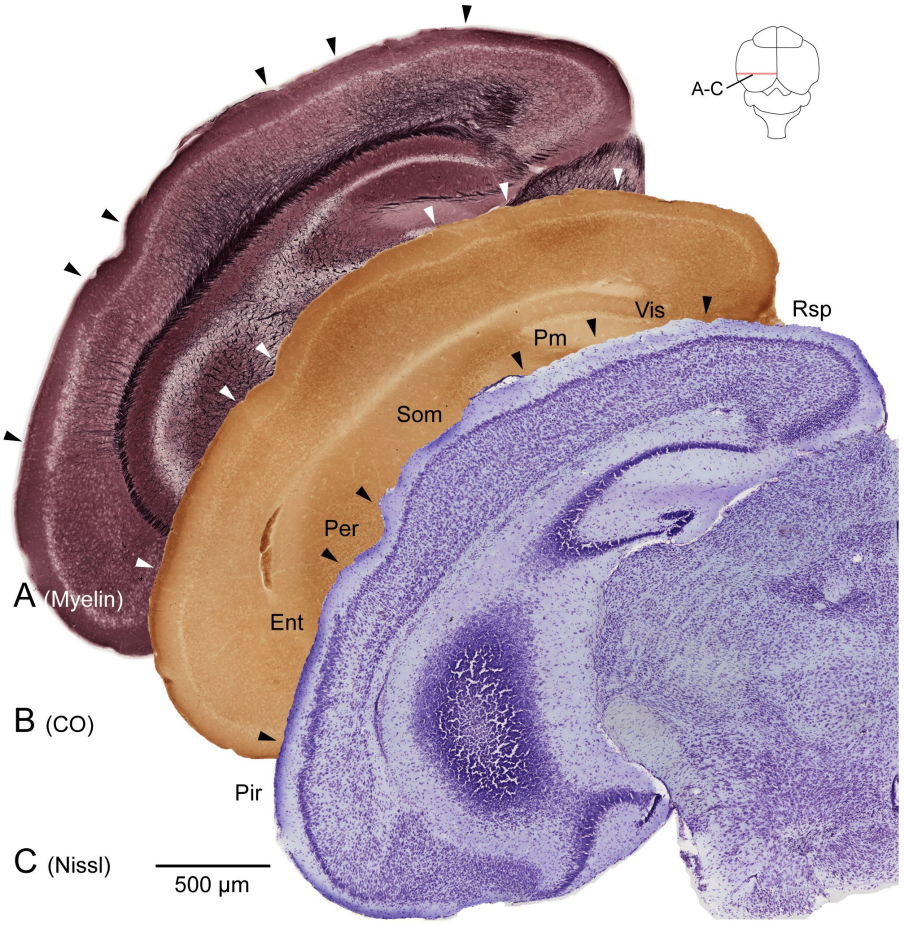

FIGURE 3.6: Cytoarchitectonics of middle parts of shrew cortex. Architectonic characteristics of the Etruscan shrew cortex shown in 3 adjacent coronal sections. Adjacent coronal sections were processed for myelin (A), cytochrome oxidase (B), and Nissl substance (C). The boundaries of proposed cortical areas are shown superimposed on the sections. Inset: the red bar indicates the location of the coronal sections shown.

is marked by a gradual increase in thickness of VGluT2 staining in layer 4 (Fig. 3.8A) and an increase in the width of the stained area (Fig. 3.2A). The piriform, insular, and perirhinal cortex show almost no staining for VGluT2 (Figs. 3.8A, 3.8B). The temporal medial and frontal medial cortex are only weakly stained compared to neighboring areas (Fig. 3.8C). The entorhinal and retrosplenial cortex show the strongest staining in layer 1 but less staining in lower layers (Figs. 3.8A, 3.8C). In general, VGluT2 staining is present in layer 1 in sensory neocortical areas but much stronger in layer 4. As shown in Figure 3.8C, frontal rostral cortex stains more strongly for VGluT2 than frontal medial cortex, which corresponds well with the others markers used to differentiate the regions, e.g. staining for myelin (Fig 3.2D).

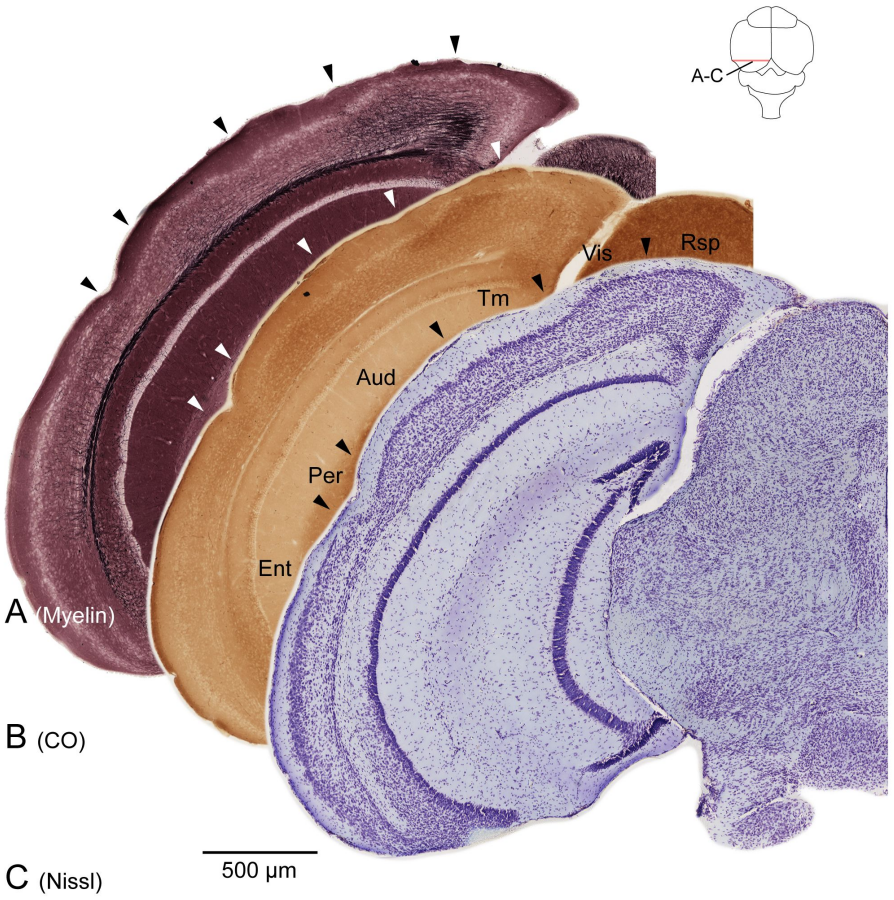

FIGURE 3.7: Cytoarchitectonics of posterior parts of shrew cortex. Architectonic characteristics of the Etruscan shrew cortex shown in 3 adjacent coronal sections. Adjacent coronal sections were processed for myelin (A), cytochrome oxidase (B), and Nissl substance (C). The boundaries of proposed cortical areas are shown superimposed on the sections. Inset: the red bar indicates the location of the coronal sections shown.

3.3.10 Number of neurons in the entire cortex and individual regions

After the cytoarchitectonic definition of clearly recognizable cortical subdivisions, which we refer to as areas, and less well-defined subdivisions which we refer to as regions, we set out to determine the number of neurons contained in these subdivisions.

The mean number of neurons per cortical hemisphere is 1,050,000 (n = 10, rounded to nearest 10,000), with a standard deviation of 160,000 (see Table 3.4). The corresponding coefficient of error (CE) was between 0.02 and 0.05, with a mean of 0.034. The coefficient of variation (CV, standard deviation / mean number of neurons) is 0.148. Subtracting the squared CE from the squared CV gives the (squared) biological coefficient of variation (BCV). The BCV^2 accounts for 95 % of the total variation (CV^2) whereas the CE^2 only accounts for 5 % of the total variation. This means that the variability due to inter-individual differences is much larger than variability of the stereological estimates.

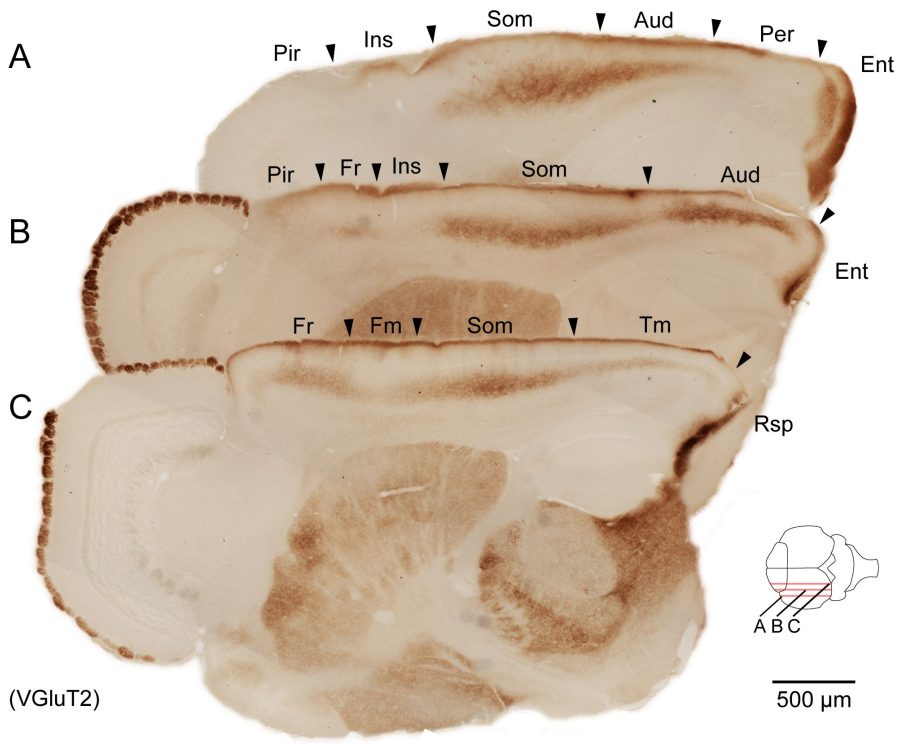

FIGURE 3.8: Three sagittal sections stained for vesicular glutamate transporter-2 (VGluT2). Architectonic characteristics of the Etruscan shrew cortex shown in 3 sagittal sections processed for VGluT2 (A), (B), (C). The boundaries of proposed cortical areas are shown superimposed on the sections. Inset: the red bars indicate the location of the sagittal sections shown.

Specimen ID	Hemisphere	Cortex neuron no. (10^6)
Sh1	U	1.11
Sh2	L	1.02
Sh2	R	1.10
Sh3	L	0.80
Sh3	R	0.90
NeuN	L	0.97
NeuN	R	1.08
Sh180	L	1.33
Sh293	L	1.25
Sh294	R	0.99
Mean ± SD		1.05 ± 0.16

TABLE 3.4: Cortex neuron number of the 10 Etruscan Shrews Analyzed. U, unknown; L, left; r, right.

The number of neurons per cortical region is shown in Table 3.5 and Figure 3.9. In each cortical hemisphere we identified and counted neurons 11 neocortical regions. On average the neocortex contained around 800,000 neurons or 70 % of the neurons in a cortical hemisphere. The region with the largest number of neurons was a non-neocortical region, the piriform cortex (shown in green in Fig. 3.9). It contains about 20 % of the neurons of one cortical hemisphere. The area with most neurons in neocortex was the somatosensory area (shown in red in Fig. 3.9) containing 17 % of the neurons of a hemisphere. The other primary sensory areas are small and located in the caudal, thin parts of the cortex and contain very few neurons. The auditory cortex (shown in blue in Fig. 3.9) contains 3 % and the visual cortex (shown in orange in Fig. 3.9) 4 % of the total amount of neurons in the cortex. For individual regions average CEs ranged from 0.05 to 0.15 with a mean of 0.1 for all regions. Given the number of neurons in a cortical hemisphere (1.05 million) and the surface area (11.1 mm^2), there are on average about 95,000 neurons below a square millimeter of cortical surface and 71 neurons below a rectangular surface area of 25 μm x 30 μm.

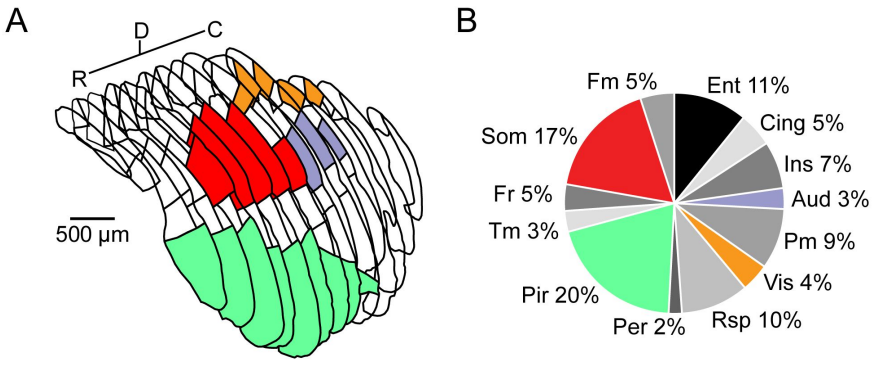

FIGURE 3.9: Illustration of counting procedure and percentage of neurons contained in each cortical area. Overview of the number of neurons per cortical area. (A) The outlines of the left hemisphere of the cortex of specimen Sh293. Shown are the 15 sections used for counting neuron numbers in individual areas. Colors show the areas highlighted in (B). R = rostral. C = caudal. D = dorsal. (B) The percentage of neurons contained on average in each cortical area for 3 shrews (see Table 3.5). Values rounded to nearest percent. See Table 3.1 for abbreviations.

3.4 Discussion

We describe general anatomical features of the cortex of the smallest terrestrial mammal - the Etruscan shrew. We identify cortical regions by cytoarchitecture and histochemical techniques. In three animals the number of neurons in these identified regions was estimated and in 10 animals the total number of neurons per cortical hemisphere was estimated using stereological techniques.

3.4.1 Architecture of the Etruscan shrew cortex

Larger brained mammals tend to have a larger number of cortical areas (Brodmann, 1909) but this is not always the case (Krubitzer, 2009). An example of this can be seen by comparing the Etruscan shrew and the hedgehog tenrec. This species was formerly grouped with the insectivores due to external similarities but is actually not closely related (Wilson and Reeder, 2005). The hedgehog tenrec has a 10 times larger brain than the Etruscan shrew but does not have a clearly defined granular layer 4 (Morawski, 2010). We propose that there is a layer 4 in the Etruscan shrew cortex, at least in the neocortical sensory areas, based on our cytochrome oxidase preparations (cytochrome oxidase stains highly active neurons in layer 4), VGluT2 staining and staining for synaptic zinc. This is consistent with early observations on shrew brains (Rose, 1912). Despite the lack of laminar differentiation in the hedgehog tenrec cortex it was possible to define several cortical areas based on microelectrode mapping and myeloarchitectonics (Krubitzer et al., 1997). Similarly, the Etruscan shrew lacks some characteristic architectonic features of mammalian cortex like sublamination of layer 4 in visual cortex (Brodmann, 1909; Rehkämper, 1981).

Nevertheless it was possible to delineate at least 13 cortical regions - a large number, considering that the about 50,000 times larger human cortex (Stephan et al., 1991; Herculano-Houzel, 2009) which contains over 5,000 times more neurons (Herculano-Houzel, 2009) has only about 50 cortical areas, according to the map of Brodmann (1909) or 200 according to more recent estimates (Kaas, 2011). Note that that the estimate of 13 cortical regions in the Etruscan shrew is a lower bound estimate, because we did not designate very small cortical regions as separate entities and were conservative in introducing areal subdivisions. In contrast to most mammals, Etruscan shrew cortex has probably a similar or even reduced number of cortical regions compared to ancestral mammalian cortex, which may have contained on the order of 15-20 cortical areas (Kaas, 2011).

3.4.2 Comparison of cytoarchitectonics and electrophysiological mapping

Figure 3.10A shows the neocortical sensory areas in color. Their location matches well with the results from electrophysiological mapping (Roth-Alpermann et al., 2010) shown in Figure 3.10B. As in our electrophysiological mapping study, the auditory cortex forms a small round area located posterior and lateral to the primary somatosensory cortex whereas the visual cortex forms a long thin strip medial and posterior to the primary somatosensory cortex. Located between auditory and visual cortex is the temporal

Specimen ID	Sh180, Sh293, Sh294		Sh 180	Sh293	Sh294		
Cortical areas	Mean thickness (μm)	Layer 1 relative thickness (%)	Neuron no. (10^4)			Mean (10^4)	% of Total
Auditory Cortex	253.0	26	3.3	4.0	3.5	3.6	3
Cingulate Cortex	578.8	21	7.2	6.7	5.0	6.3	5
Entorhinal Cortex	266.1	34	13.8	14.6	10.8	13.1	11
Frontal Medial Cortex	569.1	22	3.6	5.3	5.3	4.7	4
Frontal Rostral Cortex	390.4	29	6.7	4.8	7.4	6.3	5
Insular Cortex	532.3	31	9.8	8.3	6.1	8.1	7
Perirhinal Cortex	254.4	33	2.9	2.8	2.6	2.8	2
Piriform Cortex	586.0	31	27.1	24.8	20.3	24.1	20
Parietal Medial Cortex	481.2	23	12.0	13.5	7.3	10.9	9
Retrosplenial Cortex	460.3	23	11.8	12.7	9.3	11.3	10
Somatosensory Cortex	477.9	21	26.7	18.9	13.2	19.6	17
Temporal Medial Cortex	273.5	33	3.1	4.9	3.4	3.8	3
Visual Cortex	310.2	22	4.7	3.6	4.2	4.2	4

TABLE 3.5: Cortex area neuron number, mean area thickness, and relative extent of cortical layer 1 of the 3 Etruscan shrews analyzed.

medial cortex. In contrast to other shrew species (Catania et al., 1999), the area medial to visual cortex does not stain for cytochrome oxidase or myelin. This could point to difference in cortical organization between white-toothed shrews (Crocidurinae) like the Etruscan shrew and the red-toothed shrews investigated by Catania et al. (1999). No visual or auditory responses could be evoked in temporal medial cortex (Roth-Alpermann et al. 2010). This probably means that this area does not contain a secondary visual or auditory area. Instead, the area is responsive to whisker and body touch (Roth-Alpermann et al. 2010).

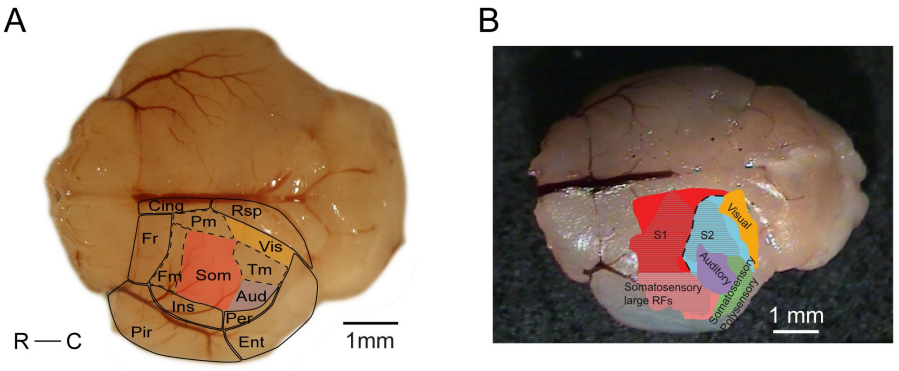

FIGURE 3.10: Overview map of the Etruscan shrew cortex and comparison with electrophysiological mapping. Comparison of anatomical and electrophysiological mapping. (A) Overview of the anatomical map assembled from coronal and tangential sections. Colors highlight the neocortical sensory areas. Other clearly identifiable regions are shown with solid lines, more putative regions with dashed lines. R = rostral. C = caudal. (B) Map of cortical areas as found in electrophysiological mapping (Roth-Alpermann et al., 2010). The primary sensory areas correspond well, the secondary somatosensory and polysensory areas could correspond to temporal, perirhinal, and insular cortex.

By both histology and electrophysiological mapping the primary somatosensory cortex is the largest and most prominent cortical area located in the middle of the cortical mantle. There are anatomical differences between the lateral and medial parts of the somatosensory cortex. Laterally the cytochrome stain approaches the pial surface and medially layer 2 and 3 take up more space. These anatomical differences point to the existence of a primary and secondary somatosensory cortex consistent the results from electrophysiological mapping (Roth-Alpermann et al. 2010).

Similar anatomical differences regarding the intensity and the uniformity of cytochrome oxidase staining were also found in the Hedgehog tenrec (Krubitzer et al., 1997). The Masked shrew and other shrew species also show an inverted representation of the body surface (Catania et al., 1999; Catania, 2005). In some studies of other mammals, multisensory responses were observed in or near the primary areas (Hunt et al., 2006, Krubitzer et al., 1997). Like previous researchers (Krubitzer et al., 1997) we found responses to body touch, whisker movement, and polysensory responses even far laterally in the

cortex. We designated these cortical regions as lateral somatosensory and polysensory areas (Roth-Alpermann et al., 2010). These regions did not show strong staining for cytochrome oxidase or myelin and correspond probably to the somatosensory, temporal medial, perirhinal and insular cortex.

In several preparations we observed patches stained strongly for cytochrome oxidase located in frontal parts of the cortex. These patches were always very close to the olfactory bulbs and comparatively far from somatosensory cortex. In all mammals examined so far motor cortex directly borders somatosensory cortex, therefore the staining pattern here probably does not correspond to motor cortex. All mammals examined to date have at least one visual, one auditory, and two somatosensory areas but not all have a motor cortex. Studies in opossums did not show evidence for a motor area rostral to somatosensory cortex but movements can be evoked by stimulating their somatosensory cortex (Beck et al., 1996; Kaas, 2011). In shrews it was not yet possible to define motor cortex by electrophysiological mapping (Catania, 2005; Roth-Alpermann et al., 2010). Nudo and Masterton (1990) found a presumptive motor cortex in the least shrew (Cryptotis parva). It is located fronto-medially and less than 400 neurons could be labeled by tracing connections from the spinal cord. Its location corresponds best to parietal medial cortex in this study. We did not find any giant Betz cells which agrees with the findings of Rose (1912) and Nudo and Masterton (1990).

In summary, converging evidence from anatomy and physiology supports the presence of primary sensory neocortical areas in the Etruscan shrew. A number of further regions (retrosplenial, cingulate, perirhinal, insular, entorhinal, frontal rostral, and piriform cortex) are cytoarchitectonically well defined and appear to be homologous to areas identified in other shrews and mammals (Catania, 2005; Wong and Kaas, 2009). We indicated these regions by filled lines in Figure 3.10A. Frontal medial, parietal medial, and temporal medial cortex are indicated by dashed lines in Figure 3.10A since they are defined by the absence of staining for cytochrome oxidase, myelin, and differences in cytoarchitecture. Corresponding regions were defined in other mammals, e.g. temporal medial cortex of the Etruscan shrew could correspond to occipital-temporal-parietal cortex in the Short-tailed opossum (Wong and Kaas, 2009).

3.4.3 Number of neurons in the entire cortex and individual regions

Several previous comparative studies have analyzed (relative) volumes of brain structures (Stephan, 1991) and the number of neurons (Herculano-Houzel, 2009). We found, that there are on average 2.1 million neurons in both cerebral hemispheres of the Etruscan shrew. We included two allocortical regions in our counts - subtracting these from

the total yields a value of 1.6 million neurons in the entire neocortex, that is, in one hemisphere there are about 800,000 neurons - as much neurons as in the honeybee brain (Witthöft, 1967). So far, the smallest numbers of cortical neurons in mammals were found in the Masked shrew (6 million, Ryzen and Campbell, 1955) and the Smoky shrew (7.14 million, Sarko et al, 2009). These numbers have been obtained by different methods from the one used here, but the definition of total cortex in Sarko et al, 2009 seems to correspond well to the definition of total cortex used here. The scaling relations between brain volume and neuron numbers have been worked out with a new non-stereological technique in rodents, primates, and insectivores (Herculano-Houzel et al., 2006, 2007, 2008; Sarko et al, 2009).

In the Etruscan shrew, most cortical neurons are in the olfactory cortex and somatosensory cortex, suggesting that smell and touch are of prime importance, similarly as implied by fossil evidence of ancestral mammals (Rowe et al., 2011). In the neocortex, one-fourth of the neocortical neurons are in somatosensory cortex which corresponds well to our observation that a large part of the Etruscan shrew neocortex responds to tactile stimuli (Roth-Alpermann et al., 2010) and the importance of tactile input for prey capture (Anjum et al., 2006). As suggested by Beaulieu (1993), this could mean that the sensory modality preferentially used by an animal will have the highest number of neurons in its corresponding cortical area. The other sensory neocortical areas are extremely small, for example the auditory and visual cortex contain on average about 40,000 neurons. For comparison, a single barrel column of rat barrel cortex contains about 20,000 neurons (Meyer et al., 2010).

Mammalian brain and cortical size varies by a factor of more than 100,000, but average cortical thickness varies only by a factor of 7; from 0.4 mm in Suncus etruscus to 2.8 mm in humans (Nieuwenhuys et al., 1998). Here we found an average value of 435 μm, very close to the value given by Nieuwenhuys et al. (1998) and Stolzenburg et al. (1989). The Cortical regions in the Etruscan shrew show a large variability in thickness as in other mammals (Rockel et al. 1980). Layer 1 of Etruscan shrew cortex takes up relatively more of the cortex than in rats and mice (DeFelipe et al., 2002) or other small mammals (Stolzenburg et al., 1989) but not the hedgehog tenrec (Stephan et al., 1991). Krieg (1946) extensively described variability of layer thickness of different cortical areas in the rat. In visual cortex (area 18) and auditory cortex (area 41) layer 1 amounts to about 10 % of total thickness (Krieg, 1946) whereas it is more than 20 % in the Etruscan shrew. In contrast, layer 1 in Krieg's area 13 takes up about 27 %; in the corresponding insular cortex in the shrew layer 1 takes up 31 %. Therefore, the relatively larger layer 1 thickness in the Etruscan shrew is most prominent in neocortical sensory areas.

Rockel et al. (1980) postulated that there are a constant number of about 110 neurons below any 25 μm x 30 μm square surface of any part of the cortex of any mammal. For the Etruscan shrew we find an average of 71 neurons, calculated using the total number of neurons and the measured surface area. This is in contrast to the findings of Rockel et al. (1980), but in line with a growing amount of data on the "nonuniformity" of the cerebral cortex (Herculano-Houzel et al., 2008; Stolzenburg et al., 1989; Beaulieu, 1993). This average value does not reflect intracortical variability of neurons in a cortical column but given the enormous variability of cortical thickness we propose that columns across the Etruscan shrew's cortex contain varying numbers of neurons. A recent study provides evidence for large variations in neuronal density across the cerebral cortex in primates (Collins et al., 2010).

A synopsis of our anatomical, physiological (Roth-Alpermann et al, 2010) and behavioral analyses (Anjum et al. 2006) portray the Etruscan shrew as an extremely tactile animal with a miniature brain that is highly specialized for active touch.

3.5 References

Anjum F, Turni H, Mulder PG, van der Burg J, Brecht M. 2006. Tactile guidance of prey capture in Etruscan shrews. Proc Natl Acad Sci 103: 16544-9.

Baron G, Stephan H, Frahm HD. 1996. Comparative Neurobiology in Chiroptera: Macromorphology, brain structures, tables, and atlases, Volume 1. Birkhäuser Verlag.

Beaulieu C. 1993. Numerical data on neocortical neurons in adult rat, with special reference to the GABA population. Brain Research 609: 284-292.

Beck PD, Pospichal MW and Kaas JH. 1996. Topography, architecture, and connections of somatosensory cortex in opossums: evidence for five somatosensory areas. J. Comp. Neurol. 366: 109-133.

Boire D, Desgent S, Matteau I and Ptito M. 2005. Regional analysis of neurofilament protein immunoreactivity in the hamster's cortex. J Chem Neuroanat 293: 193-208.

Braitenberg V, Schüz A. 1998. Cortex: Statistics and Geometry of Neuronal Connectivity Springer, Berlin, Germany.

Brodmann K. 1909. Vergleichende Lokalisationslehre der Grohirnrinde: in ihren Prinzipien dargestellt auf Grund des Zellenbaues. J.A. Barth, Leipzig.

Catania KC. 2005. Evolution of sensory specializations in insectivores. Anat Rec A Discov Mol Cell Evol Biol. 287: 1038-50.

Catania KC, Lyon DC, Mock OB, Kaas JH. 1999. Cortical organization in shrews: evidence from five species. J Comp Neurol. 410: 55-72.

Catania KC, Hare JF, Campbell KL. 2008. Water shrews detect movement, shape and smell to detect prey underwater. Proc Natl Acad Sci 105: 571-576.

Collins CE, Airey DC, Young NA, Leitch DB, Kaas JH. 2010. Neuron densities vary across and within cortical areas in primates. Proc Natl Acad Sci 107: 15927-15932.

Danscher G. 1981. Histochemical demonstration of heavy metals. A revised version of the sulphide silver method suitable for both light and electron microscopy. Histochemistry. 71: 1-16.

DeFelipe J, Alonso-Nanclarens L, Arellano JI. 2002. Microstructure of the neocortex: comparative aspects. J. Neurocytol. 31: 299-316

Ebner, FF. 1969. A comparison of primitive forebrain organization in metatherian and eutherian mammals. Ann. N.Y. Acad. Sci. 167: 241-257.

Ferrer I. 1986. Golgi study of the isocortex in an insectivore: The common European mole (Talpa europaea). Brain Behav. Evol. 29: 105-114.

Fons R, Stephan H, Baron G. 1984. Brains of Soricidae I. Encephalization and macromorphology, with special reference to Suncus Etruscus. Z. zool. Syst. Evolut.-forsch. 22: 145-158.

Fujiyama F, Furuta T, Kaneko T. 2001. Immunocytochemical localization of candidates for vesicular glutamate transporters in the rat cerebral cortex. J Comp Neurol. 435: 379-387.

Gundersen HJ, Jensen EB, Kieu K, Nielsen J. 1999. The efficiency of systematic sampling in stereology - reconsidered. J. Microsc. 193: 199-211.

Herculano-Houzel S. 2009. The human brain in numbers: a linearly scaled-up primate brain. Front Hum Neurosci. 3: 31.

Herculano-Houzel S, Mota B, Lent R. 2006. Cellular scaling rules for rodent brains. Proceedings of the National Academy of Sciences 103: 12138-12143.

Herculano-Houzel S, Collins CE, Wong P, Kaas JH. 2007. Cellular scaling rules for primate brains. Proceedings of the National Academy of Sciences 104: 3562-3567.

Herculano-Houzel S, Collins CE, Wong P, Kaas JH, Lent R. 2008. The basic nonuniformity of the cerebral cortex. Proceedings of the National Academy of Sciences 105: 12593-12598.

Howard V, Reed MG. 2005. Unbiased stereology: three-dimensional measurement in microscopy. Garland Science/BIOS Scientific Publishers, 2nd edition.

Hunt DL, Yamoah EN, Krubitzer L. 2006. Multisensory plasticity in congenitally deaf mice: How are cortical areas functionally specified? Neuroscience 139: 1507-1524

Ichinohe N, Rockland KS. 2004. Region specific micromodularity in the uppermost layers in primate cerebral cortex. Cereb Cortex. 14(11): 1173-1184.

Jürgens KD, Fons R, Peters T, Sender S. 1996. Heart and respiratory rates and their significance for convective oxygen transport rates in the smallest mammal, the Etruscan shrew Suncus etruscus. Journal of Experimental Biology 199: 2579-2584.

Kaas J, Hall WC, Diamond IT. Cortical visual areas I and II in the hedgehog: relation between evoked potential maps and architectonic subdivisions. 1970. J Neurophysiol. 33(5): 595-615.

Kaas JH. 2011. Neocortex in early mammals and its subsequent variations. Ann. N.Y. Acad. Sci. 1225: 28-36.

Krieg WJ. 1946. Connections of the cerebral cortex. 1. The albino rat. B. Structure of the cortical areas. J Comp Neurol. 84: 277-323.

Krubitzer L. The Magnificent Compromise: Cortical Field Evolution in Mammals. 2009. Neuron 56: 201-208.

Krubitzer L, Künzle H, Kaas J. 1997. Organization of sensory cortex in a Madagascan insectivore, the tenrec (Echinops telfairi). J Comp Neurol. 379: 399-414.

Lind D, Franken S, Kappler J, Jankowski J, Schilling K. 2005. Characterization of the neuronal marker NeuN as a multiply phosphorylated antigen with discrete subcellular localization. J Neurosci Res 79: 295-302.

Meyer HS, Wimmer VC, Oberlaender M, de Kock CP, Sakmann B, Helmstaedter M. 2010. Number and laminar distribution of neurons in a thalamocortical projection column of rat vibrissal cortex. Cereb Cortex. 20(10): 2277-86.

Morawski M, Brückner G, Jäger C, Seeger G, Künzle H, Arendt T. 2010. Aggrecan-based extracellular matrix shows unique cortical features and conserved subcortical principles of mammalian brain organization in the Madagascan lesser hedgehog tenrec (Echinops telfairi Martin, 1838). Neuroscience 165: 831-49.

Nieuwenhuys R, Donkelaar HJ, Nicholson C. 1998. The Central Nervous System of Vertebrates. Springer, Berlin, Heidelberg.

Nudo RJ, Masterton RB. 1990. Descending pathways to the spinal cord, III: Sites of origin of the corticospinal tract. J Comp Neurol. 296: 559-583.

Rehkämper G. 1981. Vergleichende Architektonik des Neocortex der Insektivora. Z. zool. Syst. Evolut.-forsch. 19: 233-263.

Rockel AJ, Hiorns RW, Powell TP. 1980. The basic uniformity in structure of the neocortex. Brain103: 221-44.

Rose M. 1912. Histologische Lokalisation der Großhirnrinde bei kleinen Säugetieren (Rodentia, Insectivora, Chiroptera). J. Psychol. Neurol. 19: 119-227.

Roth-Alpermann C, Anjum F, Naumann R, Brecht M. 2010. Cortical organization in the Etruscan shrew (Suncus etruscus). J Neurophysiol. 104(5): 2389-2406.

Rowe TB, Macrini TE, Luo, Z-X. 2011. Fossil evidence on the origin of the mammalian brain. Science 332: 955-957.

Ryzen M, Campbell B. 1955. Organization of the cerebral cortex III. The cortex of Sorex pacificus. J Comp Neurol 102: 365-423.

Sanides F, and Sanides D. 1972. The "extraverted neurons" of the mammalian cerebral cortex. Z. Anat. Entwickl. Gesch. 136: 272-293.

Sarko DK, Catania KC, Leitch DB, Kaas JH, Herculano-Houzel, S. 2009. Cellular scaling rules of insectivore brains. Front. Neuroanat. 3: 8.

Schmued LC. 1990. A rapid, sensitive histochemical stain for myelin in frozen brain sections. J. Histochem. Cytochem. 38: 717-720.

Stephan H. 1956. Vergleichend-anatomische Untersuchungen an Insektivorengehirnen I. Hirnform, paleo-neocortikale Grenze und relative Zusammensetzung der Cortexoberfläche. Morphol. Jb. 97: 77-142.

Stephan H, Baron G, Fons R. 1984. Brains of Soricidae II. Volume comparison of brain components. Z. zool. Syst. Evolut.-forsch., 22: 328-342.

Stephan H, Baron G, Frahm HD. 1991. Insectivora: with a stereotaxic atlas of the hedgehog brain. New York: Springer-Verlag.

Stolzenburg JU, Reichenbach A, Neumann M. 1989. Size and density of glial and neuronal cells within the cerebral neocortex of various insectivorian species. Glia 2: 78-84.

Valverde F, deCarlos JA, Lopez-Mascaraque L, and Donate-Oliver F. 1986. Neocortical layers I and II of the hedgehog (Erinaceus europaeus). II. Thalamo-cortical connections. Anat. Embryol. 175:167-179.

Vogel P. 1974. Kälteresistenz und reversible Hypothermie der Etruskerspitzmaus (Suncus etruscus, Soricidae, Insectivora). Zeitschrift fur Säugetierkunde 39: 78-88.

West MJ, Gundersen HJ. 1990. Unbiased stereological estimation of the number of neurons in the human hippocampus. J Comp Neurol. 296: 1-22.

West MJ, Slomianka L, Gundersen HJ. 1991. Unbiased stereological estimation of the total number of neurons in the subdivisions of the rat hippocampus using the optical fractionator. Anat Rec 231:482-497.

Wilson DE, Reeder DM. 2005. Mammal Species of the World: a Taxonomic and Geographic Reference. The Johns Hopkins University Press; 3rd edition.

Witthöft W. 1967. Absolute Anzahl und Verteilung der Zellen im Hirn der Honigbiene. Z. Morphol. Oekol. Tiere 61: 160-184.

Wong P, Kaas JH. 2008. Architectonic subdivisions of neocortex in the gray squirrel (Sciurus carolinensis). Anat Rec 291: 1301-1333.

Wong P, Kaas JH. 2009. An Architectonic Study of the Neocortex of the Short-Tailed Opossum (Monodelphis domestica). Brain Behav Evol. 73: 206-228

Wong-Riley M. 1979. Changes in the visual system of monocularly sutured or enucleated cats demonstrable with cytochrome oxidase histochemistry. Brain Res., 171: 11-28.

Chapter 4

Grid-layout and Theta-modulation of Layer 2 Pyramidal Neurons in Medial Entorhinal Cortex

Under review:

Saikat Ray*, Robert Naumann*, Andrea Burgalossi*, Qiusong Tang*, Helene Schmidt & Michael Brecht

* These authors contributed equally

Abstract

Little is known about how microcircuits are organized in layer 2 of medial entorhinal cortex. We visualized principal cell microcircuits and determined cellular theta-rhythmicity in freely moving rats. While calbindin-negative dentate-gyrus-projecting stellate cells were uniformly distributed, non-dentate-projecting calbindin-positive pyramidal cells bundled dendrites together and formed patches arranged in a hexagonal grid aligned to layer 1 axons, parasubiculum and cholinergic inputs. Cholinergic drive sustained theta-rhythmicity, which was two-fold stronger in pyramidal than in stellate neurons. Hence, theta-rhythmicity was cell-specific but not based on stellate-cell-intrinsic properties. Layer 2 divides into a uniform, weakly theta-locked stellate cell lattice and spatiotemporally highly organized pyramidal grid. According to clustering, rhythmicity and cholinergic modulation this grid could be an embodiment of the brain's representation of space in hexagonal grids.

4.1 Introduction

Temporal (1-3) and spatial (4) discharge patterns in layer 2 of medial entorhinal cortex (MEC) are related through phase precession (5) and the correlation of gridness (hexagonal regularity) and theta-rhythmicity (2). Layer 2 principal neurons divide into pyramidal and stellate cells, which have been suggested to shape entorhinal theta (6,7) and grid activity (8) by their intrinsic properties. Progress in understanding entorhinal microcircuits has been limited, because most though not all (9-11) data stem from extracellular recordings of unidentified cells. Such recordings have characterized diverse functional cell types (12-14) in layer 2. Clustering of grid cells (15) points to spatial organization. It is not clear, however, how functionally defined cell types correspond to stellate and pyramidal cells (7,16), which differ in conductances, immunoreactivity, projections and inhibitory inputs (6,17-20). We combined juxtacellular labeling with principal cell identification (20) to visualize microcircuits in MEC (Fig. 4.1A).

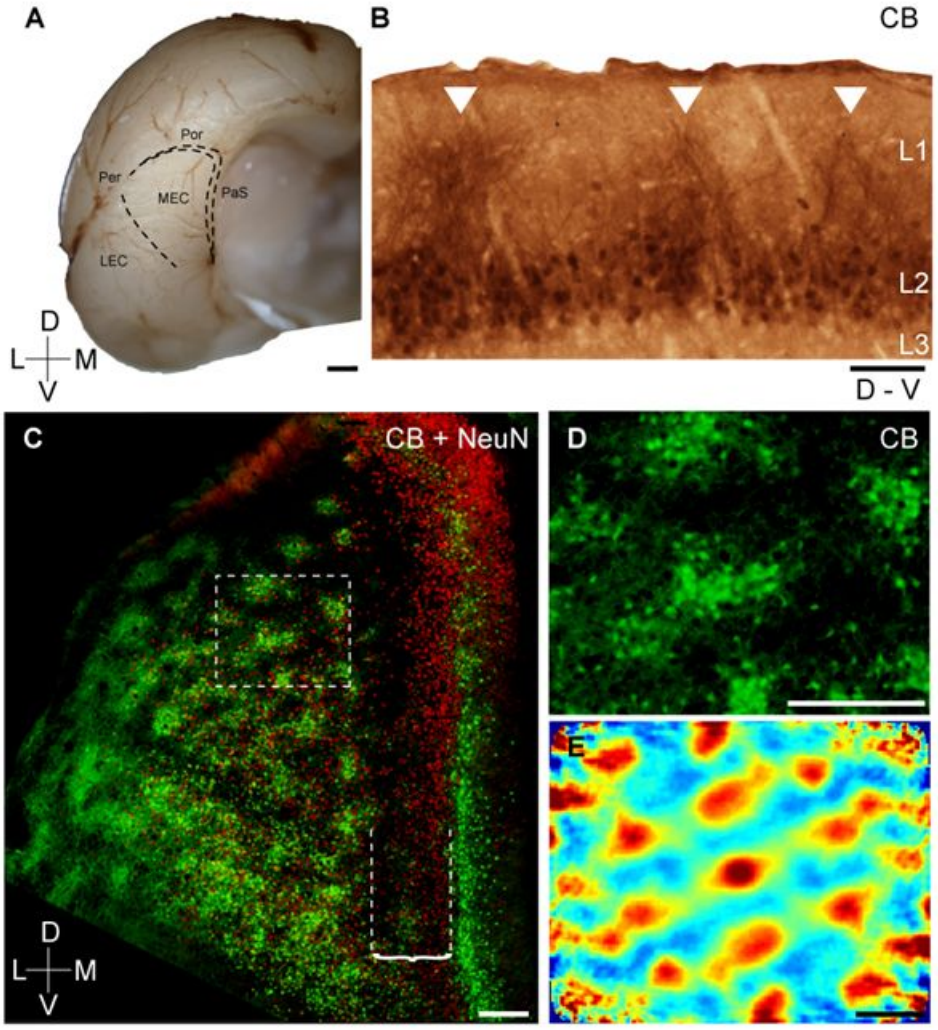

FIGURE 4.1: Grid-like arrangement of calbindin-positive pyramidal cells in the medial entorhinal cortex A, Posterior view of a rat cortical hemisphere. Medial entorhinal cortex (MEC), lateral entorhinal cortex (LEC), parasubiculum (PaS), perirhinal cortex (Per), postrhinal cortex (Por). B, Calbindin-immunoreactivity (brown precipitate) in a parasaggital section reveals patches with apical dendrites of calbindin$^+$ pyramidal cells forming tents (white arrows) in layer 1. C, Tangential section showing all neurons (red, NeuN-antibody) and patches of calbindin$^+$ neurons (green). Bracket, dashed lines indicate the patch-free stripe of MEC. D, inset from C. E, Two-dimensional spatial autocorrelation of D revealing a hexagonal spatial organization of calbindin$^+$ patches. Color scale: -0.5 (blue) through 0 (green) to 0.5 (red), grid score is 1.18. Scale bars: A = 1 mm; B = 100 μm; C,D,E = 250 μm. D = dorsal, L = lateral, M = medial, V = ventral.

4.2 Results

Calbindin immunoreactivity (20) identifies a relatively homogeneous pyramidal neuron population in MEC layer 2. Parasagittal sections stained for calbindin (Fig. 4.1B) showed that calbindin-positive (calbindin$^+$) pyramidal cells were arranged in patches (21). Apical dendrites of calbindin$^+$ pyramidal cells bundled together in layer 1 to form tent-like structures over the patches (Fig. 4.1B). The patchy structure is well defined at the layer 1/2 border, whereas a "salt and pepper" appearance of calbindin$^+$ and calbindin$^-$ cells is observed deeper in layer 2 (Fig. 4.2).

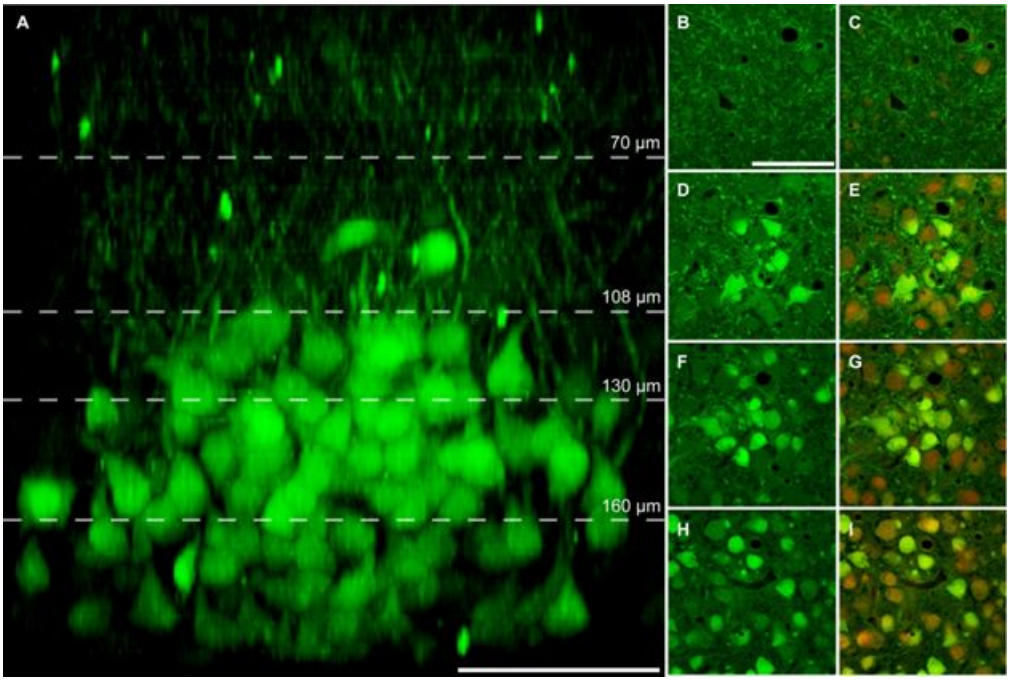

FIGURE 4.2: Cellular architecture of an individual calbindin patch A, Side view of an optically-cleared patch of calbindin$^+$ cells. Serial optical sections spaced 2 μm apart were taken along the x-z-axis and displayed as maximum intensity projection. B-I, Optical sections at the levels indicated in A, showing calbindin$^+$ cells in green (B, D, F, H) and an overlay of calbindin$^+$ cells in green and red autofluorescence showing all neurons (C, E, G, I). Dashed lines in A indicate the level of the optical sections displayed in (B-I): 70 μm below surface (B, C), 108 μm below surface D, E, 130 μm below surface (F, G) and 160 μm below surface (H, I). Note the increase in patch diameter from the upper to middle levels. At the lower level there is no apparent modular structure of calbindin$^+$ cells. Scale bars: A = 50 μm; B = 50 μm, applies to B-I.

Patches contained 187 $\pm$ 70 cells (111 $\pm$ 42, $\approx$ 60 % calbindin$^+$, 76 $\pm$ 28, $\approx$ 40 % calbindin$^-$ cells; counts of 19 patches from four brains). We double-stained tangential sections for calbindin (green) and the neuronal marker NeuN (red) to visualize patches in the cortical plane. Calbindin$^+$ (green/yellow) patches covered the MEC except for a 400-500 μm wide patch-free medial stripe adjacent to the parasubiculum (Fig. 4.1C). Clustering was not observed in calbindin$^-$ neurons (red) (Fig. 4.1C). We noted a striking hexagonal organization of calbindin$^+$ patches (Fig. 4.1C,D) and characterized this

organization by three techniques: (i) Two-dimensional spatial autocorrelation analysis (4), which captures spatially recurring features and revealed a hexagonal regularity (Fig. 4.1E). (ii) Grid scores (12) modified to quantify hexagonality also in elliptically distorted hexagons (22), distortions which result from tissue curvature and anisotropic shrinkage. Grid scores range from -2 to +2, with values >0 indicating hexagonality. The example in Fig. 4.1D had a grid score of 1.18 suggesting a high degree of hexagonality. (iii) We assessed the probability of hexagonal patch arrangements given preserved local structure (14) by a shuffling procedure. We found that the strongest Fourier component of the sample (Fig. 4.1D) exceeded that of the 99th percentile of shuffled data, suggesting such hexagonality is unlikely to arise by chance.

We retrogradely labeled neurons from ipsilateral dentate gyrus (Fig. 4.3A) using biotinylated dextran amine (Fig. 4.3B) or cholera toxin B (Fig. 4.3C) to investigate the arrangement of layer 2 principal cells with identified projection patterns and immunoreactivity (20). While most retrogradely labeled neurons were stellate cells (16,23), a small fraction had pyramidal morphologies, but these neurons appeared larger than calbindin$^+$ pyramidal cells (Fig. 4.3B). Calbindin$^+$ neurons did not project to the dentate gyrus (only 1 double-labeled out of 313 neurons in Fig. 4.3C-E; see also 20). Calbindin$^+$ patches were hexagonally arranged (Fig. 4.3C,D,F), while dentate-gyrus-projecting neurons (red) were uniformly distributed (Fig. 4.3E,G).

Reconstructions of calbindin$^+$ and calbindin$^-$ cells labeled in vivo confirmed their pyramidal and stellate morphologies, respectively. calbindin$^+$ dendrites were largely confined to patches, whereas calbindin$^-$ stellates cells had three times larger dendritic trees (7.6 vs 2.6 mm average total length, $p < 0.03$), which extended unrelated to patches (Fig. 4.3H,I). Differentiating layer 2 neurons by calbindin and reelin immunoreactivity confirmed patchy hexagonality of calbindin$^+$ cells and scattered distribution of reelin$^+$ cells without overlap between these neurons (20) (Fig. 4.4).

To investigate the organization of calbindin$^+$ patches across MEC, we prepared flattened whole-mount preparations. Patches had similar arrangements throughout the dorsoventral extent of MEC (Fig. 4.5). At the layer 1/2 border we consistently observed hexagonal arrangements in well-stained specimen. We quantified patch size and spacing in ten largely complete MEC whole-mounts. Patch density was similar throughout MEC, while patch diameter slightly increased towards ventral (Fig. 4.5). We estimated 69 $\pm$ 17 patches across the entire MEC (n = 10). Calbindin staining corresponded to previously described cytochrome-oxidase-patterns (9) with the exceptions that (i) calbindin patterns were better delineated, (ii) cytochrome-oxidase staining revealed more patches in MEC (9), (iii) patterns did not correspond in the parasubiculum.

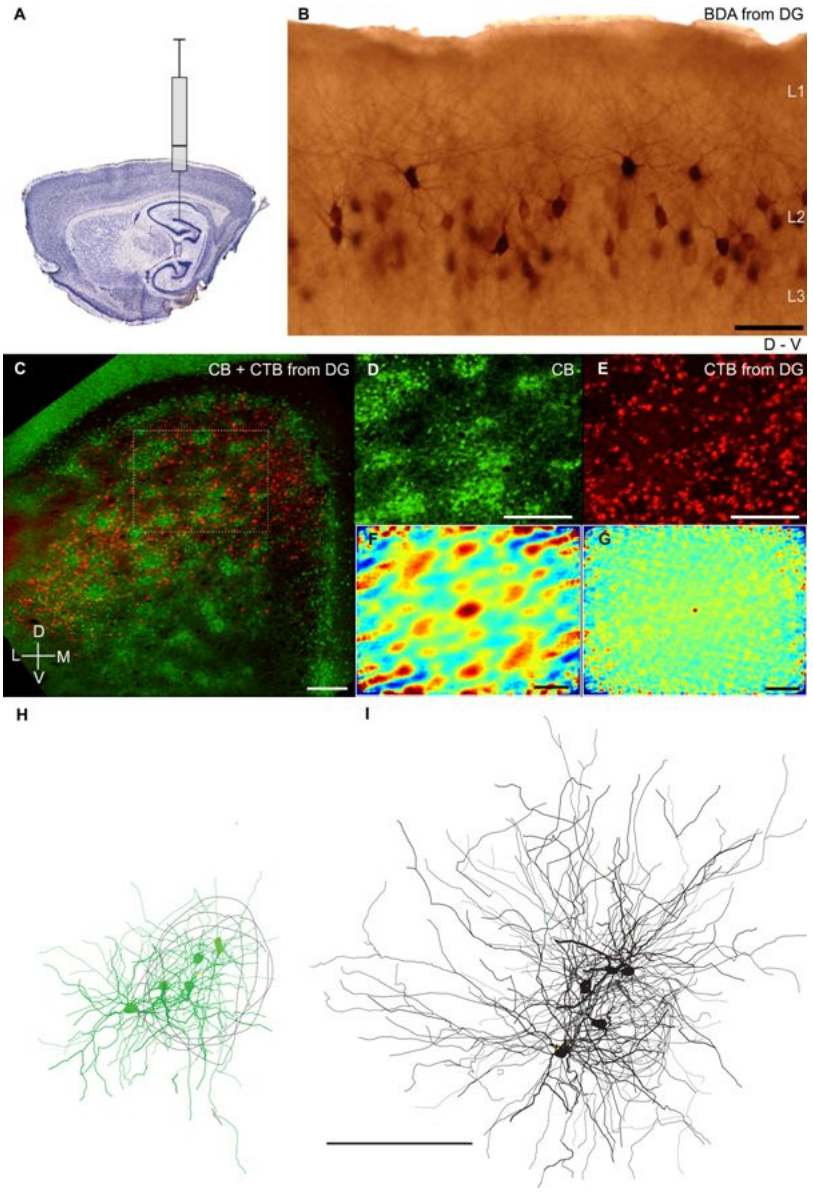

FIGURE 4.3: Calbindin positive pyramidal but not dentate-projecting stellate neurons form patches A, Schematic of retrograde labeling from dentate gyrus. B, Such retrograde labeling (BDA, brown) stains neurons (most with stellate morphologies) in a parasaggital MEC section. C, Tangential MEC section showing calbindin$^+$ neurons (green) and retrogradely-labeled neurons (red) following dentate-gyrus-cholera-toxin-B injection. D,E insets from C. F, Two-dimensional spatial autocorrelation of D reveals regular organization of calbindin$^+$ patches; grid score is 0.32. The strongest Fourier component of the sample exceeded that of the 99th percentile of shuffled data confirming hexagonality. G, Two-dimensional spatial autocorrelation of E reveals no spatial organization, grid score is -0.03. H,I, Superimposed reconstructions of dendritic morphologies of 5 calbindin$^+$ pyramidal (green) and 5 calbindin$^-$ stellate neurons (black) in the tangential plane. Morphologies were 'patch-centered' aligned according to orientation and the center of the nearest calbindin$^+$ patch (grey outlines). Scale bars: B = 100 μm; C,D,E,G,H,I = 250 μm; D = dorsal, L = lateral, M = medial, V = ventral.

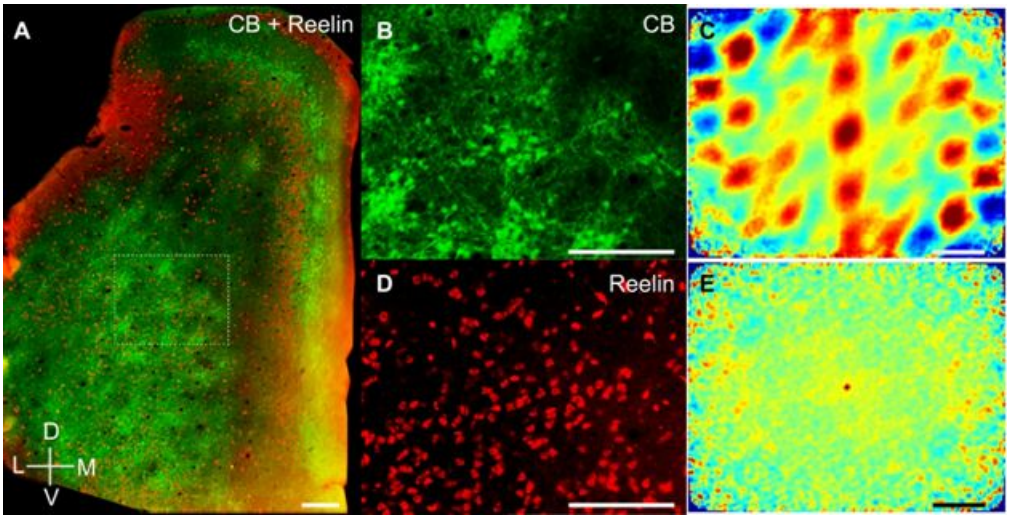

FIGURE 4.4: Calbindin-positive pyramidal neurons but not reelin-positive cells form patches. A, Tangential section of the rat MEC showing calbindin$^+$ pyramidal neurons and neuropil (green) and reelin$^+$, putative stellate, neurons (red). calbindin$^+$ and reelin$^+$ neurons form two non-overlapping populations (2 double-labeled neurons in 168 calbindin$^+$ and 405 reelin$^+$ layer 2 neurons) (20). B, Inset from A showing a high magnification of calbindin$^+$ patches. C, Two-dimensional spatial autocorrelation of B illustrating regular spatial organization of calbindin$^+$ patches. The grid score is 0.49. The strongest Fourier component of the sample exceeded that of the 99th percentile of shuffled data, confirming hexagonality. D, Corresponding image section from B showing reelin$^+$ neurons. E, Spatial autocorrelation of D illustrating a lack of spatial organization of reelin$^+$ neurons. The grid score is -0.04. Scale bars: A-E = 250 μm. D = dorsal, L = lateral, M = medial, V = ventral.

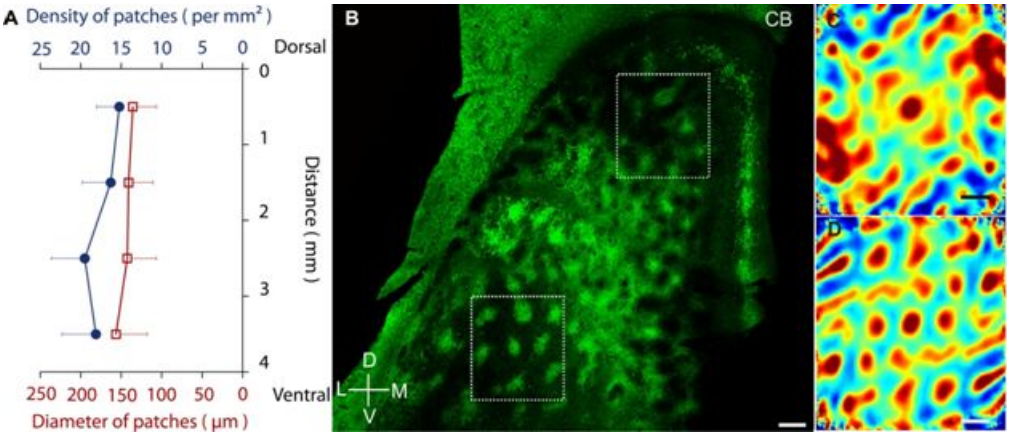

FIGURE 4.5: Layout of calbindin patches across the extent of medial entorhinal cortex A, Measurements of mean patch diameter (red) and density (blue) across the dorsoventral extent of the MEC. Measurements refer to ten MEC whole-mounts and did not include the medial patch-free stripe of MEC (see Fig. 4.1C). Error bars = SD. B, Tangential section from a flattened cortical preparation processed for calbindin immunoreactivity (green) showing modularity throughout the MEC. The image was flipped around the vertical axis for comparability. C, Two-dimensional spatial autocorrelation of the dorsal inset in A. The grid score is 0.32. The strongest Fourier component of samples C, D exceeded that of the 99th percentile of shuffled data confirming hexagonality. D, Two-dimensional spatial autocorrelation of the ventral inset in A. The grid score is 0.79.

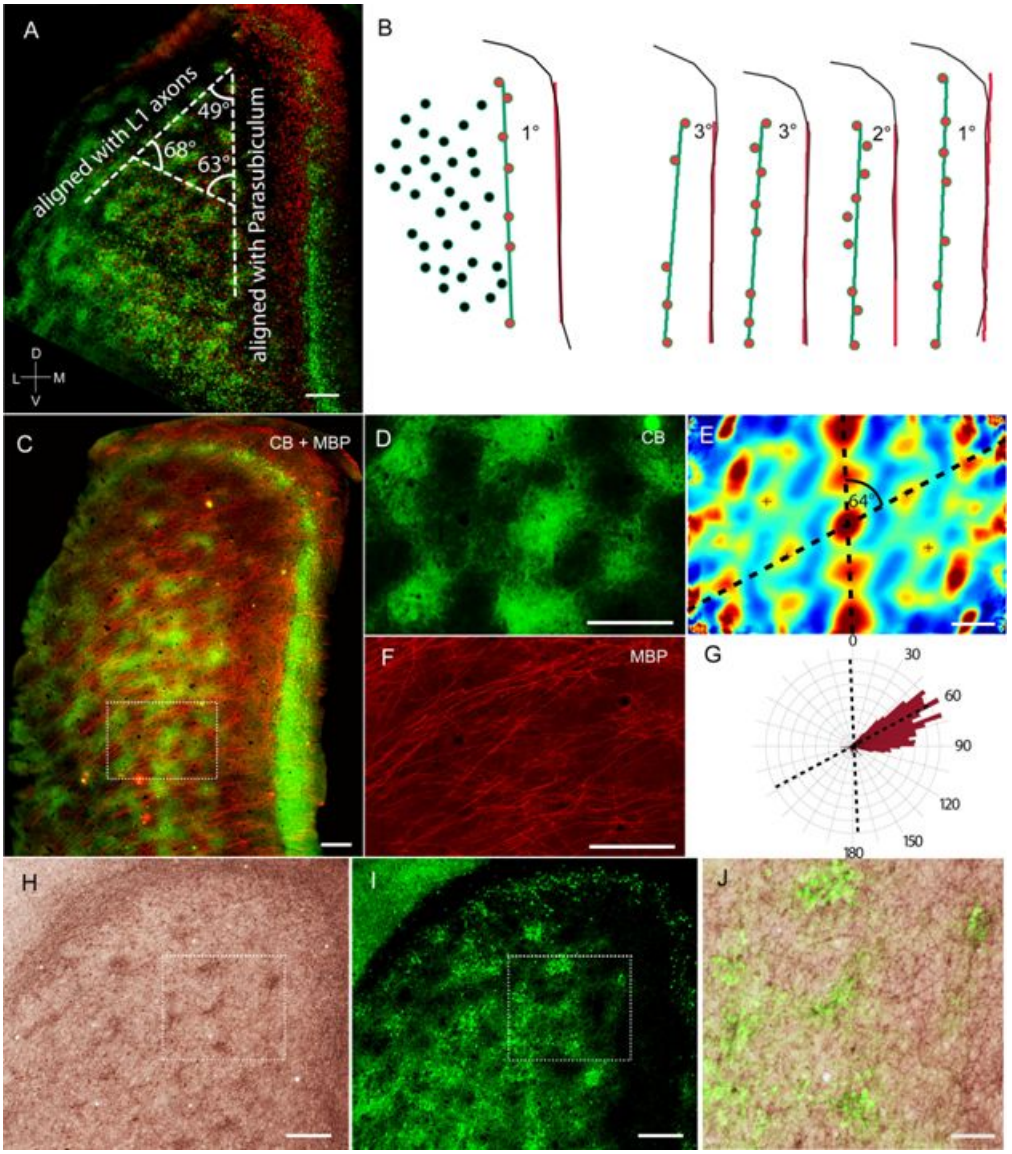

FIGURE 4.6: Alignment of the calbindin grid to parasubiculum, layer 1 axons and cholinergic markers A, Section from Fig. 4.1C. Dashed white lines indicate axes of the calbindin$^+$ grid (angles are indicated). Axes aligned with parasubiculum (B) and layer 1 axons (C-G). B, left, schematic of calbindin patches and parasubiculum from A. The orange line fits the dorsoventral axis of the parasubiculum, the green line fits the most medial column of patches (red), the angle between these lines is indicated. Right, fitted lines and their relative angles for four other brains. C, Tangential section processed for calbindin (green) and myelin basic protein (red). D, inset from C. E, Two-dimensional spatial autocorrelation of D. Dashed black lines indicate grid axes. F, inset from C. G, Polar plot of axonal orientations from F. Superimposed dashed lines are grid axes from E. H, Tangential section stained for acetylcholinesterase activity. I, Section from H co-stained for calbindin. J, Overlay of H,I shows overlap between acetylcholinesterase and calbindin staining. Scale bars: A,C,D,E,F,H,I = 250 μm; J = 100 μm. D = dorsal, L = lateral, M = medial, V = ventral.

calbindin$^+$ patches shared a roughly 60° symmetry of their axes (Fig. 4.6A). One axis runs parallel to the dorsoventral axis of the parasubiculum (Fig. 4.6A-B). Lines fitted through the dorsoventral axis of the parasubiculum and the most medial column of calbindin$^+$ patches had the same orientation (Fig. 4.6B). A second consistent axis was tilted about 60° relative to the dorsoventral axis. This calbindin$^+$ patch axis curved ventrally at more lateral positions and aligned with the orientation of overlaying layer 1 myelinated axons (Fig. 4.6C-F). Thus, the line connecting diagonally neighboring calbindin patches (revealed by spatial autocorrelation, Fig. 4.6D,E) aligned with the preferred axis of layer 1 axons (Fig. 4.6F,G), which share one orientation in MEC (9,24,25). Cholinergic transmission is of importance for MEC function (26,27) and grid cell activity (28-30). We observed a patchy pattern of acetylcholinesterase activity at the layer 1/2 border (Fig. 4.6H), which colocalized with the cores of calbindin$^+$ patches (Fig. 4.6H-J). Axonal terminals positive for the vesicular acetylcholine transporter (VAChT) were closely apposed to calbindin$^+$ cells and their density was twofold larger in calbindin$^+$ patches than between patches (Fig. 4.7).

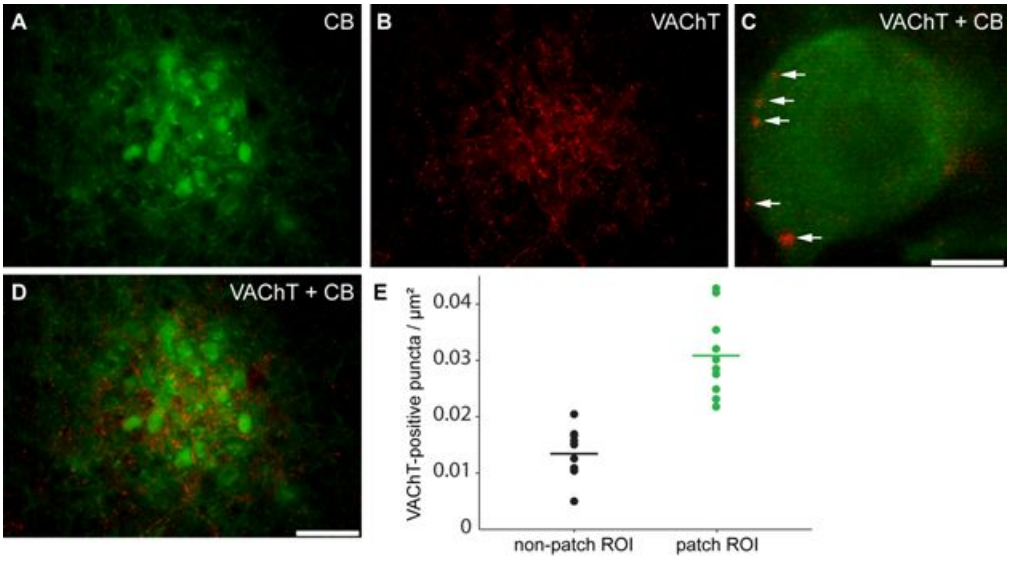

FIGURE 4.7: Vesicular acetylcholine transporter in calbindin patches A, Fluorescence micrograph showing one calbindin patch from a tangential section stained for calbindin (green). B, Same section as in A stained for VAChT immunoreactivity (red). Note the higher density of VAChT-positive puncta in the calbindin-patch than in the surrounding area. C, Magnification from B, showing close appposition of VAChT-positive puncta onto a calbindin$^+$ neuron (arrows). D, Overlay of A and B. E, Density of VAChT-positive puncta in calbindin patches (green dots) and non-patch areas (black dots) at the layer 1/2 border. In five rats we selected 10 regions of interest (ROI) centered on calbindin patches and 10 ROIs positioned equidistant between calbindin patch centers. Horizontal bars indicate mean values. All VAChT positive puncta in the ROI were counted and divided by area size to obtain puncta density. Scale bars: A, B, D = 50 μm; C = 10 μm.

Finally, we assessed in freely moving animals how activity of identified neurons related

to the entorhinal theta-rhythm. We recorded 31 layer 2 neurons in rats trained to explore open fields, and classified them by morphology and immunoreactivity. calbindin$^+$ neurons (n = 12) were pyramidal cells, while calbindin$^-$ neurons (n = 19) had stellate morphologies. Firing rates were not different (calbindin$^+$ = 2.1 ± 1.1 Hz; calbindin$^-$ = 2.3 ± 1.5 Hz; p >0.5, Mann-Whitney test). We found, however, that calbindin$^+$ neurons (Fig. 4.8A-C) showed stronger theta-rhythmicity than calbindin$^-$ cells (Fig. 4.8D-G; p <0.01, Mann-Whitney test). Theta-rhythmicity was associated with locomotion of the animal (Fig. 4.9).

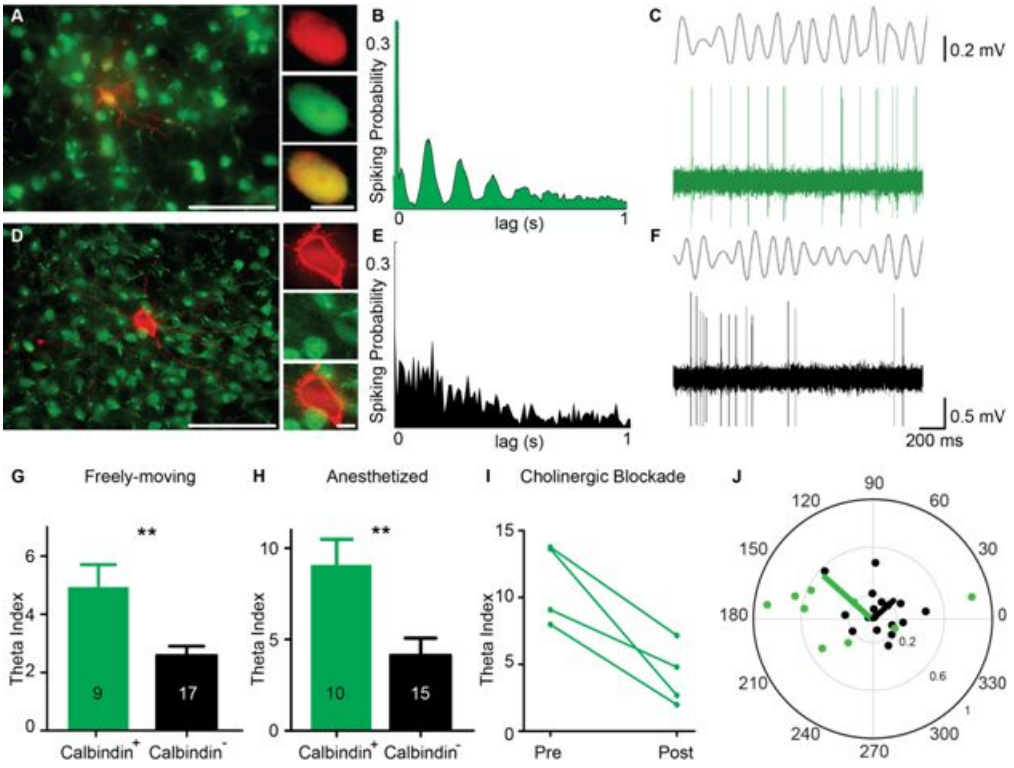

FIGURE 4.8: Theta-modulation of calbindin positive and calbindin negative cells A, Left, micrograph (tangential section) of a calbindin$^+$ neuron recorded in a freely moving animal. Green, calbindin; red, neurobiotin. Right, soma in red, green channel and overlay. B, Autocorrelogram of spike discharges for the calbindin$^+$ neuron shown in A. C, Filtered (4-12 Hz) local field potential (top) and spiking pattern (bottom) of the neuron shown in A. D-F, same as A-C but for a calbindin$^-$ neuron. G, Strength of theta-rhythmicity in calbindin$^+$ and calbindin$^-$ neurons in freely moving animals. Numbers = n of neurons. Error bars = SEM. H, Same as G but for recordings under urethane-ketamine anesthesia (31). I, Theta-rhythmicity in calbindin$^+$ neurons under anesthesia before and after systemic cholinergic blockade with scopolamine. J, Polar plot of preferred theta-phase (theta-peak = 0 °) and modulation strength (Rayleigh vector, 0-1, proportional to eccentricity) for calbindin$^+$ (green) and calbindin$^-$ (black), dots = single cells, lines = averages. Scale bars: A,D, = 100 μm (left), 10 μm (right).

A similar twofold difference in theta-rhythmicity between calbindin$^+$ and calbindin$^-$ cells was observed under urethane-ketamine anesthesia (Fig. 4.8H; p = 0.007, Mann-Whitney test), which preserves cortico-hippocampal theta-rhythmicity (3,31). To probe

the involvement of cholinergic inputs in theta-rhythmicity, we blocked cholinergic transmission by scopolamine under anesthesia and found that theta-rhythmicity was disrupted in calbindin$^+$ neurons (Fig. 4.8I). Cells also differed in their phase-locking to entorhinal field potential theta: calbindin$^+$ cells were more strongly phase-locked (average Rayleigh vector length = 0.52 vs 0.22 in calbindin$^-$ cells; p <0.004, Mann-Whitney test) and fired near the trough of the theta-oscillation, whereas locking was weaker and more variable in calbindin$^-$ cells (Fig. 4.8J).

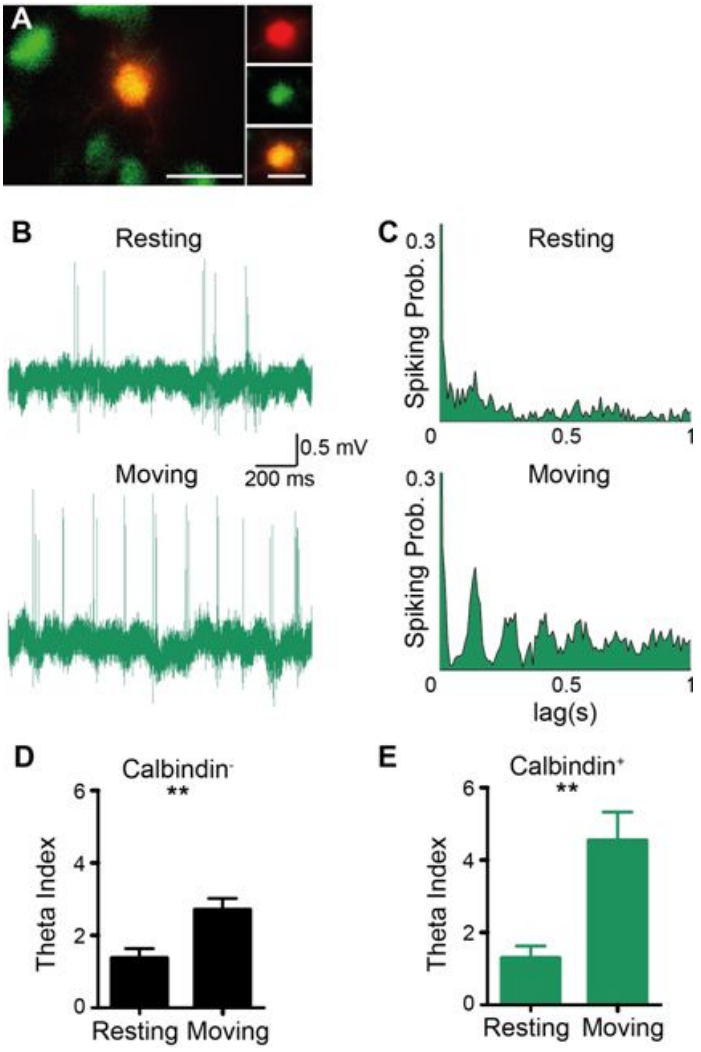

FIGURE 4.9: Movement dependency of theta-rhythmicity of spiking activity in calbindin-positive neurons A, Fluorescence micrograph of a representative calbindin$^+$ layer 2 neuron recorded from a freely moving rat. Green: calbindin, red: Neurobiotin. Scale bars: 100 m (left) and 10 m (right). B, Representative raw juxtacellular traces from the calbindin$^+$ neuron shown in A under resting (top) and moving state (bottom; speed cutoff = 2 cm/s). Note the prominent theta-rhythmicity of spiking activity during movement. C, Spike autocorrelograms of the calbindin$^+$ neuron shown in A under resting (top) and moving state (bottom). D,E Population average of the strength of theta-rhythmicity (theta index; see Supplementary Methods) under resting and moving state in calbindin$^-$ (D) and calbindin$^+$ neurons (E). Note the stronger movement dependency of theta-rhythmicity for calbindin$^+$ neurons. P = 0.0034 (left panel, n = 17) and 0.0036 (right panel, n = 9), Mann-Whitney test. Error bars = SEM.

4.3 Discussion

What is the cellular basis of theta-rhythmicity in MEC layer 2? Stellate cells have been prime candidates for theta discharges in layer 2 (6,7), because intrinsic conductances make them resonate at theta frequency (32,33). We found, however, that calbindin$^+$ pyramidal cells showed twofold stronger theta-rhythmicity and theta phase-locking than calbindin$^-$ stellate neurons. The stronger theta-rhythmicity of calbindin$^+$ pyramidal neurons, which have weaker sag-currents (7,9,20), is opposite from what had been predicted based on intrinsic properties (8,34). Hence, layer 2 theta-modulation is cell type specific, but not driven by cell-intrinsic resonance properties. This conclusion agrees with other evidence that questions a causal relationship between intrinsic properties and theta-rhythmicity in vivo (10,34,35). calbindin$^+$ neurons might correspond to a subset of neurons with strong membrane potential theta-oscillations (11). Cholinergic innervation and effects of cholinergic blockade suggest cholinergic drive sustains theta-rhythmicity of calbindin$^+$ cells. The finding that cholinergic transmission targets the non-dentate-projecting calbindin$^+$ cells might be related to the observation that medial-septum-blockade disrupts grid cells, but only mildly affects hippocampal place cells (28-30).

We were not yet able to assess spatial modulation in a sufficient number of identified neurons to directly relate our results to grid cell function. The limited available evidence suggests grid cells are a heterogeneous neuronal population in layer 2 (10,11,36) possibly indicating weak structure-function relationships (37). Yet, we observed intriguing similarities between calbindin$^+$ neurons and grid cells: (i) calbindin$^+$ cells receive cholinergic inputs, which are required for grid cell activity (28-30); (ii) calbindin$^+$ cells have strong theta-rhythmicity, a feature which correlates with grid cell discharge (2); (iii) like grid cells, calbindin$^+$ cells are clustered. Our observations inspired a 'isomorphic mapping hypothesis' according to which an anatomical grid is instrumental in generating grid cell activity (38). Alignment of calbindin$^+$ neurons and layer 1 axons could contribute to grid scale modularity (15) by funneling similar axonal input into stripes of patches. Hexagonality often results from spacing constraints, but such mechanisms do not predict MEC-pyramidal-grid alignment. A 'grid-cell-grid' might offer similar advantages as isomorphic representations of body parts in somatosensory cortices of tactile specialists. In such isomorphisms, whisker pads are represented as barrel fields (39) and nose appendages as nose stripes (40). Resolving identified entorhinal circuits during navigation will tell, if the calbindin$^+$ grid is an embodiment of the brain's representation of space in hexagonal grids.

4.4 References

1. M. Mizuseki, A. Sirota, E. Pastalkova, G. Buzski, Neuron 64, 267 (2009).

2. C.N. Boccara et al., Nat. Neurosci. 13, 987 (2010).

3. P. Quilichini, A. Sirota, G. Buzski, J. Neurosci. 30, 11128 (2010).

4. T. Hafting, M. Fyhn, S. Molden, M-B. Moser, E.I. Moser, Nature 436, 801 (2005).

5. T. Hafting, M. Fyhn, T. Bonnevie, M-B. Moser, E.I. Moser, Nature 453, 1248 (2008).

6. A. Alonso, R.R Llins, Nature 342, 175 (1989).

7. A. Alonso, R. Klink, J. Neurophysiol. 70, 128 (1993).

8. M.E. Hasselmo, L.M. Giocomo, E.A. Zilli, Hippocampus 17, 1252 (2007).

9. A. Burgalossi, et al., Neuron 70, 773 (2011).

10. C. Schmidt-Hieber, M. Häusser, Nat. Neurosci. 16, 325 (2013).

11. C. Domnisoru, A.A. Kinkhabwala, D.W. Tank, Nature 495, 199 (2013).

12. F. Sargolini, et al., Science 312, 758 (2006).

13. T. Solstad, C.N. Boccara, E. Kropff, M-B. Moser, E.I. Moser, Science 322, 1865 (2008).

14. J. Krupic, N. Burgess, J. O'Keefe, Science 337, 853 (2012).

15. H. Stensola et al., Nature 492, 72 (2012).

16. P. Germroth, W.K. Schwerdtfeger, E.H. Buhl, Neuroscience 30, 683 (1989).

17. K. Lingenhöhl, D.M Finch, Exp Brain Res 84, 57 (1991).

18. R. Klink, A. Alonso, J. Neurophysiol. 77, 1813 (1997).

19. C.B. Canto, M.P. Witter, Hippocampus 22, 1277 (2012).

20. C. Varga, S.Y. Lee, I. Soltesz, Nat. Neurosci. 13, 822 (2010).

21. Y. Fujimaru, T. Kosaka, Neurosci. Res. 24, 329 (1996).

22. C. Barry, L.L. Ginzberg, J. O'Keefe, N. Burgess, Proc. Natl. Acad. Sci. U.S.A. 109, 17687 (2012).

23. N. Tamamaki, Y. Nojyo, Y. Hippocampus 3, 471 (1993).

24. T.W. Blackstad, J. Comp. Neurol. 105, 417 (1956).

25. M.P. Witter, Prog. Neurobiol. 33, 161 (1989).

26. C. Barry, J.G. Heys, M.E. Hasselmo, Front Neural Circuits 6, 5 (2012).

27. J.G. Heys, N.W. Schultheiss, C.F. Shay, Y. Tsuno, M.E. Hasselmo, Front Behav Neurosci 6, 32 (2012).

28. J. Koenig, A.N. Linder, J.K. Leutgeb, S. Leutgeb, Science 332, 592 (2011).

29. M.P. Brandon et al., Science 332, 595 (2011).

30. E.L. Newman, M.E. Hasselmo, Society for Neuroscience Meeting Abstract (2011).

31. T. Klausberger et al., Nature 421, 844 (2003).

32. D.L.F. Garden, P.D. Dodson, C. O'Donnell, M.D. White, M.F. Nolan, Neuron 60, 875 (2008).

33. L.M. Giocomo, M.E. Hasselmo, J. Neurosci. 28, 9414 (2008).

34. F.R. Fernandez, J.A. White, J. Neurosci. 28, 3790 (2008).

35. L.M. Giocomo et al., Cell 147:1159 (2011)

36. S.J. Zhang et al., Science 340, 123 (2013).

37. D.C. Rowland, M.-B. Moser Curr. Opin. Neurobiol. 24:22 (2014).

38. M. Brecht et al. Phil. Trans. Royal Soc in revision (2013).

39. T.A. Woolsey, H. Van der Loos, Brain Res. 17, 205 (1970).

40. K.C. Catania, R.G. Northcutt, J.H. Kaas, P.D. Beck, Nature 364, 493 (1993).

41. This work was supported by Humboldt Universität zu Berlin, BCCN Berlin (German Federal Ministry of Education and Research BMBF, Förderkennzeichen 01GQ1001A), NeuroCure, the Neuro-Behavior ERC grant and the Gottfried Wilhelm Leibniz Prize of the DFG. We thank Christian Ebbesen, Moritz von Heimendahl, Rajnish Rao, Juliane Steger, John Tukker and Undine Schneeweiß.

4.5 Materials and Methods

All experimental procedures were performed according to German guidelines on animal welfare.

4.5.1 Brain tissue preparation

For anatomy experiments, male and female Wistar rats (150-400 g) were anesthetized by isoflurane, and then euthanized by an intraperitoneal injection of 20% urethane. They were then perfused transcardially with 0.9% phosphate buffered saline solution, followed by 4% paraformaldehyde (PFA) in 0.1 M phosphate buffer (PB). After perfusion, brains were removed from the skull and postfixed in PFA overnight. They were then transferred into a 10% sucrose solution in PB and left overnight, and subsequently immersed in 30% sucrose solution for at least 24 hours for cryoprotection. The brains were embedded in Jung Tissue Freezing Medium, and subsequently mounted on the freezing microtome to obtain 20-60 μm thick sagittal sections or tangential sections (parallel to the pial surface). Tangential sections of the medial entorhinal cortex were obtained by separating posterior cortices (including the entorhinal cortex) from the remaining hemisphere by a cut parallel to the surface of the medial entorhinal cortex. The tissue was then frozen and positioned with the pial side to the block face of the microtome.

4.5.2 Histochemistry and immunohistochemistry

Acetylcholinesterase (AChE) activity was visualized according to previously published procedures (42,43). After washing brain sections in a solution containing 1 ml of 0.1 M citrate buffer (pH 6.2) and 9 ml 0.9% NaCl saline solution (CS), sections were incubated with CS containing 3 mM $CuSO_4$, 0.5 mM K3Fe$(CN)_6$, and 1.8 mM acetylthiocholine iodide for 30 min. After rinsing in PB, reaction products were visualized by incubating the sections in PB containing 0.05% 3,3'- Diaminobenzidine (DAB) and 0.03% nickel ammonium sulfate.

Immunohistochemical stainings were performed according to standard procedures. Briefly, brain sections were pre-incubated in a blocking solution containing 0.1 M PBS, 2% Bovine Serum Albumin (BSA) and 0.5% Triton X-100 (PBS-X) for an hour at room temperature (RT). Following this, primary antibodies were diluted in a solution containing PBS-X and 1% BSA. Primary antibodies against the calcium binding proteins Calbindin (1:5000), the extracellular matrix protein Reelin (1:1000), the extrinsic membrane protein Myelin Basic Protein (1:1000), the vesicular acetylcholine transporter (1:1000), and

the DNA binding neuron specific protein NeuN (1:1000) were used. Incubations with primary antibodies were allowed to proceed for at least 24 hours under mild shaking at 4 °C in free-floating sections. Incubations with primary antibodies were followed by detection with secondary antibodies coupled to different fluorophores (Alexa 488 and 546). Secondary antibodies were diluted (1:500) in PBS-X and the reaction was allowed to proceed for two hours in the dark at RT. For multiple antibody labeling, antibodies raised in different host species were used. After the staining procedure, sections were mounted on gelatin coated glass slides with Mowiol or Vectashield mounting medium.

In a subset of experiments, primary antibodies were visualized by DAB staining. For this purpose, endogenous peroxidases were first blocked by incubating brain tissue sections in methanol containing 0.3% hydrogen peroxide in the dark at RT for 30 min. The subsequent immunohistochemical procedures were performed as described above, with the exception that detection of primary antibodies was performed by biotinylated secondary antibodies and the ABC detection kit. Immunoreactivity was visualized using DAB staining.

For whole-mount immunohistochemistry (as in Fig. 4.2) we used a variant of the protocol in (44,45). Thick tangential sections ($\approx$ 300 μm) containing layer 2 of the MEC were first post-fixed in Dent's fixative overnight at 4 °C and then incubated in Dent's bleach overnight at 4 °C. They were then dehydrated twice in 100% methanol for 30 min each and then rehydrated for 90 min each in 50% and 15% methanol in PBS at RT. Subsequently, sections were incubated with 10 μg/ml proteinase K for 5 min at RT. Sections were then rinsed three times for ten minutes in PBS at RT and subsequently incubated in PBS-X containing 2% BSA overnight. Primary antibodies were diluted in PBS-X containing 5% DMSO, 1% BSA and incubated for 96 hours at 4 °C. After this incubation, whole-mounts were washed in PBS-X three times for 2-3 h each and then incubated overnight in secondary antibodies diluted in PBS-X and 5% DMSO at 4 °C. Sections were then washed three times in PBS-X for 2-3 h each and incubated in PBS-X overnight to ensure efficient removal of unbound antibodies. The sections were dehydrated in series of 50%, 80%, and 100% methanol in PBS at RT for 90 min each. Finally, the sections were transferred for at least 2 days into a clearing solution consisting of two parts of benzyl benzoate and one part of benzyl alcohol at RT, until they became transparent.

For histological analysis of juxtacellularly-labeled neurons, neurobiotin was visualized with streptavidin conjugated to Alexa 546 (1:1000). Subsequently, immunohistochemistry for Calbindin was performed as described above and visualized with Alexa Fluor 488. After fluorescence images were acquired, the neurobiotin staining was converted into a dark DAB reaction product, performed as previously described (31). This has

advantages of being more sensitive than most fluorescent dyes, is permanent and not sensitive to photobleaching (46). In general we found similar results for calbindin immunohistochemistry as previous authors (20,47), who showed that the large majority ($\approx$ 90% in 47) of calbindin$^+$ cells are glutamatergic neurons.

4.5.3 Retrograde Neuronal Labeling

Retrograde tracer solutions containing either Biotynilated-Dextrane Amine (BDA) (10% w/v; 3.000 MW) or Cholera Toxin Subunit B, Alexa Fluor 488 Conjugate (CTB) (0.8 % in PB) were injected in juvenile rats ($\approx$ 150 g) under ketamine/xylazine anesthesia. Briefly, a small craniotomy was opened above the dentate gyrus at intermediate positions along the septo-temporal axis. Animals were placed in a stereotaxic apparatus, and prior to injection, the granule cell layer was localized by electrophysiological recordings, based on characteristic signatures of the local field potential and neuronal spiking activity. Glass electrodes with a tip diameter of 10-20 μm, filled with CTB or BDA solution, were then lowered unilaterally into the target region. Tracers were either pressure-injected (CTB; 10 injections using positive pressure of 20 p.s.i., 10-15 s injection duration) or iontophoretically-injected (BDA; 7s on/off current pulses of 1-5 mA for 15 min). After the injections, the pipettes were left in place for several minutes and slowly retracted. The craniotomies were closed by application of silicone and dental cement. The animals survived for 3-7 days before being transcardially perfused. The results from back-labeling agreed with previous authors (16,23,48), who also found that the large majority of retrogradely-labeled neurons from the dentate gyrus had stellate morphologies.

4.5.4 Image acquisition

A microscope equipped with a motorized stage and a z-encoder, was used for bright field microscopy. Images were captured using a MBF CX9000 camera using Neurolucida or StereoInvestigator. An epifluorescence microscope with camera was used to image the immunofluorescent sections. Alexa fluorophores were excited using the appropriate filters (Alexa 488 - L5, Alexa 546 - N3). Fluorescent images were acquired in monochrome, and colour maps were applied to the images post acquisition. Whole-mount stainings were imaged using a microscope. Fluorescence images were acquired with a 25x (1.05 NA) water-immersion objective. A femtosecond laser was used to excite fluorophores at 850 nm. Post hoc linear brightness and contrast adjustment were applied uniformly to the image under analysis.

4.5.5 Cell Counts and Patch Sizes

In the analysis for determining cell numbers and patch sizes, patches in consecutive sections were matched by overlaying them in Adobe Photoshop, and only the ones which could be reliably followed in all the sections under consideration were taken up for further analysis. Image stacks were first converted into .tiff files for different channels and focal planes using ImageJ. These files were then merged back together into a single file using the Neurolucida image stack module. In these patches all cells positive for Calbindin and NeuN were counted manually. Quantification of patch sizes was done with the Neurolucida software by using the mean of maximum and minimum Feret diameter, defined as the maximum and minimum diameter of the patch, respectively. To correct for overestimation of neurons due to double counting in two adjacent sections, we estimated the number of cells in a section assuming uniform cell density and uniform spherical cell shape in the section and applied a correction factor of s / (s+d) where, s is the section thickness and d is the diameter of a cell, to correct for the cells which would be counted again in an adjacent section.

4.5.6 Quantification of axonal orientation and cholinergic boutons

To quantify the orientation of axonal fibers in layer 1, axon segments from myelin-stained sections were traced using Neurolucida software. The polar histogram in Fig. 4.6 was constructed with angular bins of 3 °, and the total length of axons in each angular direction was summed up.

Using Stereoinvestigator software we quantified the density of VAChT-positive puncta in calbindin patch and non-patch areas at the layer 1/2 border in tangential sections from five rats. In total, we selected 10 regions of interest (ROI) centered on calbindin patches and 10 ROIs positioned equidistant between calbindin patch centers. All VAChT positive puncta in the ROI were counted manually and divided by area size to obtain puncta density.

4.5.7 Analysis of Spatial Periodicity

To determine the spatial periodicity of calbindin$^+$ patches, we determined spatial autocorrelations and spatial Fourier spectrograms. The spatial autocorrelogram was based on Pearson's product moment correlation coefficient (as in 12):

$$\mathrm{r}(\tau_x,\, \tau_y) = \frac{n\sum f(x,y)f(x-\tau_x,y-\tau_y) - \sum f(x,y)\sum f(x-\tau_x,y-\tau_y)}{\sqrt{n\sum f(x,y)^2-(\sum f(x,y))^2}\sqrt{n\sum f(x-\tau_x,y-\tau_y)^2-(\sum f(x-\tau_x,y-\tau_y))^2}}$$

where, r(τ_x, τ_y) is the autocorrelation between pixels or bins with spatial offset τ_x and τ_y. f is the image without smoothing or the firing rate map after smoothing, n is the number of overlapping pixels or bins. Autocorrelations were not estimated for lags of τ_x and τ_y, where n<20.

Grid scores were calculated as previously described (49) by taking a circular sample of the autocorrelogram, centered on, but excluding the central peak. The Pearson correlation of this circle with its rotation for 60 degrees and 120 degrees was obtained (on peak rotations) and also for rotations of 30 degrees, 90 degrees and 150 degrees (off peak rotations). Gridness was defined as in (13) as the minimum difference between the on-peak rotations and off-peak rotations. To determine the grid scores, gridness was evaluated for multiple circular samples surrounding the center of the autocorrelogram with circle radii increasing in unitary steps from a minimum of 10 pixels more than the width of the radius of the central peak to the shortest edge of the autocorrelogram. The radius of the central peak was defined as the distance from the central peak to its nearest local minima in the spatial autocorrelogram. The grid score was defined as the best score from these successive samples (13). Grid scores reflect both the hexagonality in a spatial field and also the regularity of the hexagon. To disentangle the effect of regularity from this index, and consider only hexagonality, we transformed the elliptically distorted hexagon into a regular hexagon (22) and computed the grid scores. A linear affine transformation was applied to the elliptically distorted hexagon, to stretch it along its minor axis, till it lay on a circle, with the diameter equal to the major axis of the elliptical hexagon. The grid scores were computed on this transformed regular hexagon. The spatial Fourier spectrogram was calculated by implementing a two dimensional discrete Fourier transform and determining its power (14):

$$\mathrm{F(x,y)}=\frac{1}{\sqrt{MN}}\sum_{n=0}^{N-1}\sum_{m=0}^{M-1} f(m,n)e^{-2\pi i(\frac{mx}{M}+\frac{ny}{N})}$$

$$\mathrm{P(x,y)}=\sqrt{F_r^2(x,y)+F_i^2(x,y)}$$

where, F is the spatial Fourier transform of f, which is a binary image representing the sample with regions of interest (patches) marked as white blocks, with the remaining area as black and zero padded to 2048x2048. M and N are the width and height of the image before zero-padding. Normalization by $\sqrt{MN}$ enables comparison of Fourier power in differently sized samples. P is the power of the Fourier transform with F_r and F_i being the real and imaginary parts of the Fourier transform.

To determine the probability that the patches present in the selected area would be arranged hexagonally, we employed a shuffling procedure and compared the maximum Fourier power of the block pattern representing the original image, to the 99th percentile of the power of a shuffled one with the same blocks (representing the patches) being

randomly distributed in the same area without overlapping. This shuffling was performed on all samples on a sample-by-sample basis until the 99th percentile of the maximum power Fourier component converged to a constant.

4.5.8 Electrophysiology methods

Basic procedures for obtaining juxtacellular recordings in freely moving animals were essentially performed as previously described (9,50), but with two significant changes in our procedures: (1) different from the approach taken previously, we worked exclusively with animals extensively familiarized with the test arenas and trained to forage for chocolate pellets during the recording (see below); (2) We did not use our previous wake-up protocol, where single neurons were labeled in initially anesthetized animals, which were woken-up by injection of antagonist, and the activity of the neurons subsequently monitored in freely-moving animals. Instead, neurons were analyzed in drug-free animals. These changes were implemented to have the same experimental conditions as in previous studies (4). Juxtacellular recordings in freely moving animals were obtained in male Wistar and Long-Evans rats (150-250 g) which were maintained on a 12-h light / 12-h dark schedule and tested in the dark phase. Pipettes (4-6 MΩ) were filled with extracellular (Ringer) solution containing (in mM) NaCl 135, KCl 5.4, HEPES 5, $CaCl_2$ 1.8, and $MgCl_2$ 1 (pH 7.2) as well as neurobiotin (1-2%). Rats were habituated to the behavioral arena and trained for 3-7 days (2-6 sessions per day, of 15-20 min duration each) to collect randomly scattered chocolate crumbs in the behavioral arena (80x80 cm or 1x1 m square box with a white cue card on the wall). Training was performed both before and after implantation (see below), or only after implantation (3-5 days). Animals were then implanted according to previously published procedures (9,50) with a basic head-implant, which included a metal post for head-fixation and placement of a miniaturized preamplifier, a plastic ring and a protection cap (50). For targeting the dorsalmost region of medial entorhinal cortex, a plastic ring was glued on the skull surface 0.2-0.8 mm anterior to the transverse sinus and 4.5-5 mm lateral to the midline. Animals were allowed to recover from the surgery, after which they were habituated to head-fixation for 3-5 days, as previously described (51), and trained to chase chocolate pellets in the open field arena. On the day of recording, the implants were completed under isoflurane anesthesia (1-3%) by implanting an additional metal post, which served to anchor the miniaturized micromanipulator (52). Animals were put back in their cages, and allowed to recover from the isoflurane anesthesia. 3-4 hours to 1 day later, rats were then head-fixed and the miniaturized micromanipulator and preamplifier secured to the metal posts. After the recording glass electrode was advanced into the brain, a thick agarose solution (4-5% in Ringer) was applied into the recording chamber for

sealing the craniotomy. Animals were then released from the fixation frame and gently transferred to the behavioral arena. To minimize discomfort from the head implant, we sometimes supplied local anesthesia in the neck region. Searching for neurons began when animals were already freely behaving and running in the arena. At the end of the recording, juxtacellular labeling was attempted according to standard procedures (51). After labeling, the animal was injected with an overdose of ketamine or urethane and perfused transcardially with 4% paraformaldehyde solution, typically within 10-30 min after labeling.

Juxtacellular recordings in anesthetized animals (Fig. 4.8H-I) were performed under ketamine/urethane anesthesia, essentially as previously described (31). The ketamine/urethane mix is the anesthetic of choice for studying temporal dynamics of spiking activity, and it has long been used to study many aspects of hippocampal and entorhinal physiology (3,31). In a subset of recordings (n=4, Fig. 4.8I), scopolamine was injected systemically (0.4-1 mg/ml, i.p.) (54). After a pre-injection baseline recording of $\approx$ 5 min, scopolamine was injected and the effect on the recorded cell's activity monitored for further 15-20 min. The juxtacellular signals were amplified by the ELC-03XS amplifier and sampled at 20 kHz by a data-acquisition interface under the control of PatchMaster 2.20 software. The animal's location was automatically tracked at 25 Hz by a videotracking system.

4.5.9 Data analysis

The position of the rat was defined as the midpoint between two head-mounted LEDs. A running speed threshold (2 cm/s) was applied for isolating periods of rest from active movement. Theta-rhythmicity of spiking discharge was determined by first calculating the spike train's autocorrelation determined from the Fast Fourier Transform-based power spectrum of the spike-train autocorrelation functions of the cells, binned at 10 ms. To measure modulation strength in the theta band (4-12 Hz), a theta-index was computed (2), defined as the average power within 1 Hz of the maximum of the autocorrelation function in the 4-12 Hz, and divided by the average power in the 3-125 Hz range. Only cells with firing rate >0.5 Hz were included in the theta analysis (17 out of 19 calbindin$^-$ cells and 9 out of 12 calbindin$^+$ cells) since low firing rates impede detection of firing rhythmicity (55). Statistical significance was assessed by two-tailed Mann-Whitney nonparametric test with 95% confidence intervals.

For spike-theta phase analysis, juxtacellular signals were band-pass filtered at 4-12 Hz, and a Hilbert transform was used to determine the instantaneous theta phase of the filtered theta wave (peaks = 0, 360 ° and troughs = 180 °). Then, each spike was assigned

to the theta-phase of the Hilbert transform at the time of that spike. Only spikes during running (speed cutoff = 2 cm/s) were included in the analysis. To estimate the modulation strength, the Rayleigh average vector of spikes' theta phases was calculated for each cell and then averaged across each neuronal subpopulation (calbindin$^-$ and calbindin$^+$ neurons). Spike distributions within the theta cycle were computed for each cell by using bins of 18 °.

4.5.10 Methods references

42. N. Ichinohe et al., Cereb. Cortex 18, 1125 (2008).

43. S. Tsuji, Folia Histochem. Cytobiol. 36, 67 (1998).

44. R.V. Sillitoe, R. Hawkes, J. Histochem. Cytochem. 50, 235 (2002).

45. N. Jährling, K. Becker, E.R. Kramer, H-U. Dodt, Medical Laser Application. 23, 209 (2008).

46. M. Marx, R.H. Günter, W. Hucko, G. Radnikow, D. Feldmeyer, Nat. Protoc. 7, 394 (2012).

47. R.F. Langston et al., Science 328, 1576 (2010).

48. D.A. Peterson et al., Journal of Neuroscience 16, 886 (1996).

49. S.P. Schwartz, P.D. Coleman, Experimental neurology 74, 305 (1981).

50. L. Herfst et al., J Neurophysiol. 108, 697 (2012).

51. A.R. Houweling, G. Doron, B.C. Voigt, L.J. Herfst, M. Brecht, J. Neurophysiol. 103, 1696 (2010).

52. A.K. Lee, I.D. Manns, B. Sakmann, M. Brecht, Neuron 51, 399 (2006).

53. D.A. Pinault, J. Neurosci. Methods 65, 113 (1996).

54. Y. Tsuno, N.W. Schultheiss, M.E. Hasselmo, J Physiol. 15, 2611 (2013).

55. C. Barry, D. Bush, J. O'Keefe, N. Burgess, Nature 488, 103 (2012).

Chapter 5

Modular architecture of superficial layers of the rat retrohippocampal region

Abstract

The entorhinal cortex is a central brain region for spatial cognition in mammals. Its structure is highly organized into different areas, layers and modules. These modules have been best described in primates but less extensively in rodents. The goal of this study is a descriptive mapping of modular structures in superficial layers of the rat medial entorhinal cortex as a basis for further quantitative anatomical and functional investigations. We focus on putative pyramidal cells marked by calbindin immunoreactivity and putative stellate cells marked by reelin immunoreactivity. In superficial layer 2 of medial entorhinal cortex these cells show a strikingly ordered distribution. The distribution of these groups of cells is related to staining patterns of cytochrome oxidase, zinc ions, innervation by basket cells and subcortical transmitter systems. We compare the modular structure of entorhinal cortex with modular patterns of other retrohippocampal areas and discuss the possible functional significance of modular patterns in the light of known retrohippocampal connections.

5.1 Introduction

In rodents, the entorhinal cortex has recently emerged as a central hub in the circuits for spatial navigation through the discovery of grid cells (Hafting et al., 2005), which increase their activity in certain locations, tiling space in a hexagonal grid pattern. The spatial activity pattern of individual grid cells is modular but there are also modules of different grid cells along the dorso-ventral axis in entorhinal cortex (Barry et al., 2007; Brun et al., 2008). A recent detailed study described up to 5 modules of different grid-spacing in the dorsal half of medial entorhinal cortex (Stensola et al., 2012). So far it has been difficult to assign a distinct function to the various types of modular structures in the cerebral cortex (Horton & Adams, 2005; da Costa & Martin, 2010). Therefore, we aim to provide a map of modular structures in the rat entorhinal cortex, as a basis for investigations of the structural determinants of function.

5.1.1 Two populations of principal cells in layer 2 of medial entorhinal cortex

In layer 2 of medial entorhinal cortex there are two distinct principal cell types based on electrophysiological properties: intrinsically rhythmic neurons and neurons that do not show intrinsic rhythmicity (Alonso & Llinás, 1989; Alonso & Klink, 1993). Morphological identification indicates that intrinsically rhythmic cells are stellate cells, whereas pyramidal cells are not intrinsically rhythmic (Klink & Alonso, 1997). Recently, Varga et al. (2010) demonstrated that reelin positive cells show electrophysiological parameters traditionally assigned to stellate cells whereas electrophysiological properties of calbindin positive cells are similar to those of pyramidal cells. This suggests a simple scheme of cellular organization yet there are a variety of intermediate morphologies between stellate and pyramidal cells (Canto & Witter, 2012) and at least some stellate cells may be calbindin positive (Fujimaru & Kosaka, 1996; Wouterlood, 2002). Cells most strongly immunoreactive for calbindin are often GABAergic cells, such as double bouquet cells in the primate cortex (DeFelipe, 1997), but in superficial layers of isocortex and entorhinal cortex, $\approx$ 90 % of the (weakly) calbindin positive cells are not GABAergic (Kubota et al., 1994; Peterson et al., 1996). Instead, they show pyramidal morphology (Hayes & Lewis, 1992).

5.1.2 Multiple markers of modularity in layer 2 of medial entorhinal cortex

A number of histochemical markers are distributed in a modular pattern in rodent medial entorhinal cortex, yet their relation to the principal cell distribution is largely unknown. In Chapter 4 we demonstrated that acetylcholinesterase patches (Mathisen & Blackstad, 1964; Slomianka & Geneser, 1991) overlap with clusters of calbindin positive cells. Other markers revealing modularity include cytochrome oxidase (Burgalossi et al., 2011), zinc ions (Slomianka, 1992; Slomianka & Geneser, 1997) and a number of afferent fiber systems such as commissural fibres (Blackstad, 1956), inputs from presubiculum and parasubiculum (Köhler, 1985), and intrinsic connections originating in layer 5 of medial entorhinal cortex (Köhler, 1986 b). Since calbindin positive cells in medial entorhinal cortex show a striking geometric order (Fujimaru & Kosaka, 1996) we ask whether the same is true for reelin positive cells and investigate differences in their innervation by basket cells. The relations of different modular structures are only poorly defined in rodents (Witter & Moser, 2006). We use classic histochemical methods such as cytochrome oxidase staining and staining for synaptic zinc in combination with immunohistochemical stainings, to clarify the relations between the different markers. We suggest that this may form a basis for connecting cellular level microcircuits, modular scale connectivity and possibly modular distribution of cellular function in medial entorhinal cortex.

LEC	Lateral entorhinal cortex
MEC	Medial entorhinal cortex
Occ	Occipital cortex
PaS	Parasubiculum
Per	Perirhinal cortex
Por	Postrhinal cortex
PrS	Presubiculum
Rsa	Retrosplenial agranular cortex
Rsg	Retrosplenial granular cortex
Sub	Subiculum
AChE	Acetylcholinesterase
CB	Calbindin
CCK	Cholecystokinin
CO	Cytochrome oxidase
CR	Calretinin
NADPH	β-nicotinamide adenine dinucleotide phosphate diaphorase, NADPH diaphorase
NeuN	neuronal specific nuclear protein
M2	muscarinic acetylcholine receptor subtype M2
PV	Parvalbumin
TH	Tyrosine hydroxylase
VGluT3	Vesicular glutamate transporter 3
5-HT	Serotonin

Table 5.1: Abbreviations.

5.2 Methods

5.2.1 Animals

Male and female young adult Wistar rats were used in the study. All experimental procedures were performed according to the German guidelines on animal welfare under the supervision of local ethics committees.

5.2.2 Tissue Preparation

Animals were anaesthetized by isoflurane, and then euthanized by an intraperitoneal injection of 20% urethane. They were then perfused transcardially with first 0.9% phosphate buffered saline solution, followed by 4% formaldehyde, from paraformaldehyde (PFA), in 0.1 M phosphate buffer. After perfusion, brains were removed from the skull and postfixed in PFA overnight. They were then transferred to 10% sucrose solution for one night and subsequently immersed in 30% sucrose solution for at least one night for

cryoprotection. The brains were embedded in Jung Tissue Freezing Medium (Leica Microsystems Nussloch, Germany), and subsequently mounted on the freezing microtome (Leica 2035 Biocut) to obtain 20-60 μm thick sagittal sections, horizontal sections or tangential sections parallel to the pia.

Tangential sections of the medial entorhinal cortex were obtained by separating the entorhinal cortex from the remaining hemisphere by a cut parallel to the surface of the medial entorhinal cortex. For subsequent sectioning the surface of the entorhinal cortex was attached to the block face of the microtome.

5.2.3 Histochemistry

Acetylcholinesterase activity: Acetylcholinesterase (AChE) was stained following the method of Ichinohe et al. (2008) and Tsuji (1998). After washing in a mixture containing 1 ml of 0.1 M citrate buffer (pH 6.2) and 9 ml 0.9% saline (CS), sections were incubated with CS containing 3 mM $CuSO_4$, 0.5 mM K3Fe$(CN)_6$, and 1.8 mM acetylthiocholine iodide for 30 min. After rinsing in PB, sections were intensified in PB containing 0.05% 3,3'- Diaminobenzidine (DAB) and 0.03% nickel ammonium sulfate.

Synaptic zinc: After perfusion with a solution containing sodium sulfide, brain sections to be stained for synaptic zinc were washed thoroughly with 0.1 M PB, followed by 0.01 M PB. This staining method allows to label zinc ions, which are present in presynaptic terminals of glutamatergic cortico-cortical projection neurons. For the visualisation of synaptic zinc, sections were developed as described by Danscher (1981). In brief, sections were exposed to a solution containing gum arabic, citrate buffer, hydroquinone and silver lactate for 60-120 minutes, in the dark at room temperature. Development of reaction products was checked under a microscope and terminated by rinsing the sections in 0.01 M PB and, subsequently, several times in 0.1 M PB (Ichinohe & Rockland, 2004).

NADPH diaphorase activity: NADPH diaphorase activity was visualized according to the protocol of Paxinos et al. (2009). Sections were washed in PB and then incubated in PB containing 1.35 mM β-NADPH (Sigma, N1630), 305 μM nitroblue tetrazolium (Sigma, N6876), 1 mM $MgCl_2$, and 0.5% Triton X-100. The incubation was done at 37 °C for 30 min and terminated by washing in PB.

Myelin staining: For myelin staining, a variation of the gold-chloride protocol was used (Schmued, 1990). Briefly, free-floating cryostat sections were incubated for 2-4 hours in a 0.1% solution of gold chloride in 0.02 M phosphate buffer, pH 7.4, and 0.9% sodium chloride. After staining, sections were rinsed for 5 min, fixed for 5 min in a 2.5% solution of sodium thiosulfate, and rinsed again for 30 min before mounting with Mowiol.

Cytochrome oxidase activity: For cytochrome oxidase staining we used the protocol of Wong-Riley (1979).

Immunohistochemistry: Tangential, horizontal and sagittal sections were immunostained for antibodies listed in Table 2. For multiple antibody labeling, antibodies raised in different host species were combined. In each series of sections the primary antibody was omitted in one section to control for secondary antibody specificity. This always led to complete absence of staining. When available, a control antigen was added to the incubation medium of one section for each series to control for primary antibody specificity. This always led to a strong reduction in staining intensity.

Calbindin The mouse monoclonal anti-calbindin (CB) antibody was raised using hybridization of mouse myeloma cells with spleen cells from mice immunized with the CB D-28k that was purified from the chicken gut (Celio et al., 1990). This monoclonal antibody is not known to cross-react with other known calcium binding-proteins and specifically stains the 45Ca-binding spot of CB D-28k (MW 28,000, IEP 4.8) of different mammals in a two-dimensional gel (manufacturer's technical information).

The rabbit polyclonal anti-CB antiserum was raised against recombinant rat calbindin D-28k (Airaksinen et al., 1997). It crossreacts with calbindin D-28k from many mammalian species. In immunoblots it recognizes a single band of approximately 27-28 kDa (manufacturer's technical information).

Parvalbumin The goat polyclonal anti-PV antiserum was raised against rat muscle parvalbumin (Schwaller et al., 1999). It cross-reacts with some other mammalian species but does not stain the brain of parvalbumin knock out mice (manufacturer's technical information).

Calretinin The monoclonal antibody against calretinin (CR) was produced in mice by immunization with recombinant human calretinin-22k (Zimmermann & Schwaller, 2002). The antibody reacts specifically with calretinin in tissue originating from human and rat and does not cross-react with other known calcium binding-proteins, as determined by its distribution in the brain, as well as by immunoblots (manufacturer's technical information).

Neuronal specific nuclear protein The polyclonal rabbit antibody was raised against Glutathione S-transferase -tagged recombinant protein corresponding to mouse neuronal specific nuclear protein (NeuN) (Mullen et al., 1992). This antibody recognizes NeuN at the N-terminus in several mammalian species. A previous lot of this antibody recognized 2-3 bands in the 46-48 kDa range and possibly another band at approximately 66 kDa (manufacturer's technical information).

Name	Species	Catalog No.	Immunogen	Supplier	Dilution	Specificity
Anti-Calbindin	mouse monoclonal	300	Calbindin D-28k purified from chicken gut	Swant, Bellinzona, Switzerland	1:5000	Manufacturer
Anti-Calbindin	rabbit polyclonal	CB38	recombinant rat calbindin D-28k	Swant, Bellinzona, Switzerland	1:5000	Manufacturer
Anti-Parvalbumin	goat polyclonal	PVG214	rat muscle parvalbumin	Swant, Bellinzona, Switzerland	1:5000	Manufacturer
Anti-Calretinin	mouse monoclonal	6B3	recombinant human calretinin-22k	Swant, Bellinzona, Switzerland	1:5000	Manufacturer
Anti-NeuN	rabbit polyclonal	ABN78	GST-tagged recombinant protein corresponding to mouse NeuN	Millipore, Billerica, MA, USA	1:1000	Manufacturer
Anti-tyrosine hydroxylase	mouse monoclonal	MAB318	Tyrosine Hydroxylase purified from PC12 cells	Millipore, Billerica, MA, USA	1:1000	Manufacturer
Anti-serotonin	rabbit polyclonal	AB125	5-Hydroxytryptamine-glutaraldehyde-Poly-lysine	Millipore, Billerica, MA, USA	1:1000	Manufacturer
Anti-M2 receptors	rat monoclonal	MAB367	i3 loop of m2 receptor fusion protein (225-359), fused to Glutathione S-transferase	Millipore, Billerica, MA, USA	1:1000	Manufacturer
Anti-CCK	goat polyclonal	sc-21617	peptide mapping near the C-terminus of CCK of human origin	Santa Cruz Biotechnology, CA, USA	1:500	Manufacturer

TABLE 5.2: Primary Antibodies Used in this Study

Tyrosine hydroxylase The monoclonal antibody was raised against tyrosine hydroxylase (TH) purified from PC12 cells (Croft et al., 2005). It recognizes an epitope on the outside of the regulatory N-terminus in a wide range of vertebrate species and recognizes a protein of approximately 59-61 kDa by Western blot (manufacturer's technical information).

Serotonin The polyclonal rabbit antibody was produced against 5-Hydroxytryptamine-glutaraldehyde-Poly-lysine (Geffard et al., 1985). This antibody has been reported to stain a pattern of cellular morphology and distribution identical to previous reports of serotonergic neurons (Lu et al., 2006).

M2 receptors The monoclonal rat antibody was raised against the i3 loop of m2 receptor fusion protein (225-359), fused to Glutathione S-transferase (Levey et al., 1995). It recognizes a full length m1 protein in mice and rats. It has exhibited no cross reactivity with other muscarinic proteins tested so far (manufacturer's technical information).

Cholecystokinin The affinity purified goat polyclonal antibody was raised against a peptide mapping near the C-terminus of cholecystokinin (CCK) of human origin. This antibody recognizes CCK in a wide range of mammalian species (manufacturer's technical information; Bombardi et al., 2010).

For the immunostainings processed with DAB, first, the endogenous peroxidases were blocked by incubating methanol containing 0.3% hydrogen peroxide in the dark at room temperature (RT) for 30 mins. Rinses were carried out between all incubation steps with 0.1 M phosphate buffered saline (PBS). They were then pre-incubated in a blocking solution containing 0.1 M PBS, 2% Bovine Serum Albumin (BSA) and 0.5% Triton X-100 (PBS-X) for an hour. Following this, the primary antibody was diluted as described above with PBS-X and 1% BSA and incubated overnight at 4 °C.

Subsequently, the appropriate biotinylated secondary antibody (Vectorlabs, Burlingame CA, USA; 1:200) was diluted with PBS-X and the sections were incubated in this solution for two hours at RT. Then, sections were incubated in freshly prepared avidin biotin complex (ABC kit, PK-6100, Vectorlabs, Burlingame CA, USA) solution in PBS. Peroxidase was visualized using DAB histochemistry.

In some cases, in addition to DAB staining, alkaline phosphatase (Vectorlabs, Burlingame CA, USA; 1:200), was used for dual color immunohistochemistry for light microscopy. Alkaline phosphatase was diluted with PBS-X and the sections were incubated in this solution overnight. Alkaline phosphatase was visualized using Vector Blue (Vector Blue Alkaline Phosphatase Substrate Kit, SK-5300, Vectorlabs, Burlingame CA, USA).

For immunofluorescence, the sections were pre-incubated as above prior to incubating in the primary antibodies. Subsequently, secondary antibodies conjugated to different fluorophores (Invitrogen; 488 nm, 546 nm, 633 nm excitation wavelength) and reactive to different species were diluted (1:500) with PBS-X to incubate the sections for two hours, in the dark, at RT.

After the staining procedure, sections were mounted on gelatin coated glass slides and cover-slipped with Mowiol, Vectashield (H-1000, Vectorlabs, Burlingame CA, USA) or Fluoromount (0100-01, Southern Biotech, Birmingham AL, USA) mounting medium.

5.2.4 Light and fluorescence microscopy

An Olympus BX51 microscope (Olympus, Shinjuku Tokyo, Japan) was used to view the images using bright field microscopy. The microscope was equipped with a motorized stage (LUDL Electronics, Hawthorne NY, USA) and a z-encoder (Heidenhain, Shaumburg IL, USA). Images were captured using a MBF CX9000 (Optronics, Goleta CA, USA) camera using Neurolucida or StereoInvestigator (MBF Bioscience, Williston VT, USA).

A Leica DM5500B epifluorescence microscope with a Leica DFC345 FX camera (Leica Microsystems, Mannheim, Germany) was used to image the immunofluorescent sections. Alexa fluorophores were excited using the appropriate filters (Alexa 488 - L5, Alexa 546 - N3, Alexa 633 - Y3). The fluorescent images were acquired in monochrome and colour maps were applied to the images post acquisition.

Post hoc linear brightness and contrast adjustment were applied uniformly to the image under analysis.

5.3 Results

5.3.1 Reelin positive cells form a lattice surrounding calbindin patches

The study of Varga et al. (2010) related two immunohistochemical markers, calbindin and reelin, to distinct electrophysiological cell types. Figures 5.1A, 5.1B, 5.1C show a tangential section through upper layer 2 of medial entorhinal cortex stained for reelin and calbindin immunoreactivity. Reelin positive cells are densely packed but leave out patches lacking reelin positive cells (arrows in Fig. 5.1A). These patches contain a high density of calbindin positive cells (Fig. 5.1B, 5.1C). Figure 5.1D shows a tangential section stained for reelin immunoreactivity. This section includes a large part of upper layer 2 of medial entorhinal cortex and ventro-laterally the transition to lateral entorhinal cortex. The reelin positive cells leave out a regular array of (calbindin) patches. Figure 5.1E shows a higher magnification view from Figure 5.1D, highlighting the regular pattern of patches lacking reelin positive cells. Another high magnification view, from a section at the layer 1/2 border, shows that reelin positive cells form ring-like structures surrounding calbindin patches (Fig. 5.1F). For an overview of the entorhinal cortex in tangential, horizontal and sagittal sections, see Chapter 1, Figure 1.2.

5.3.2 Calbindin positive and negative cells differ in innervation by basket cells

Varga et al. (2010) show that cholecystokinin positive basket cell terminals specifically innervate calbindin positive cells using VGluT3 as an indirect marker (Somogyi et al., 2004). We find that cholecystokinin immunoreactivity in medial entorhinal cortex layer 2 occurs in clusters (Fig. 5.2A; Köhler, 1986 a). Figures 5.2B and 5.2C shows that cholecystokinin terminals are prominent surrounding calbindin positive cells. A higher magnification view (Fig. 5.2D) illustrates that cholecystokinin positive puncta form baskets surrounding calbindin positive cells. In contrast, parvalbumin positive neuropil surrounds nearly all cells in layer 2 (Fig. 5.2E). Figures 5.2F and 5.2G shows parvalbumin positive neuropil are prominent surrounding calbindin positive cells. A higher magnification view (Fig. 5.2H) illustrates that parvalbumin positive puncta form baskets surrounding calbindin positive cells.

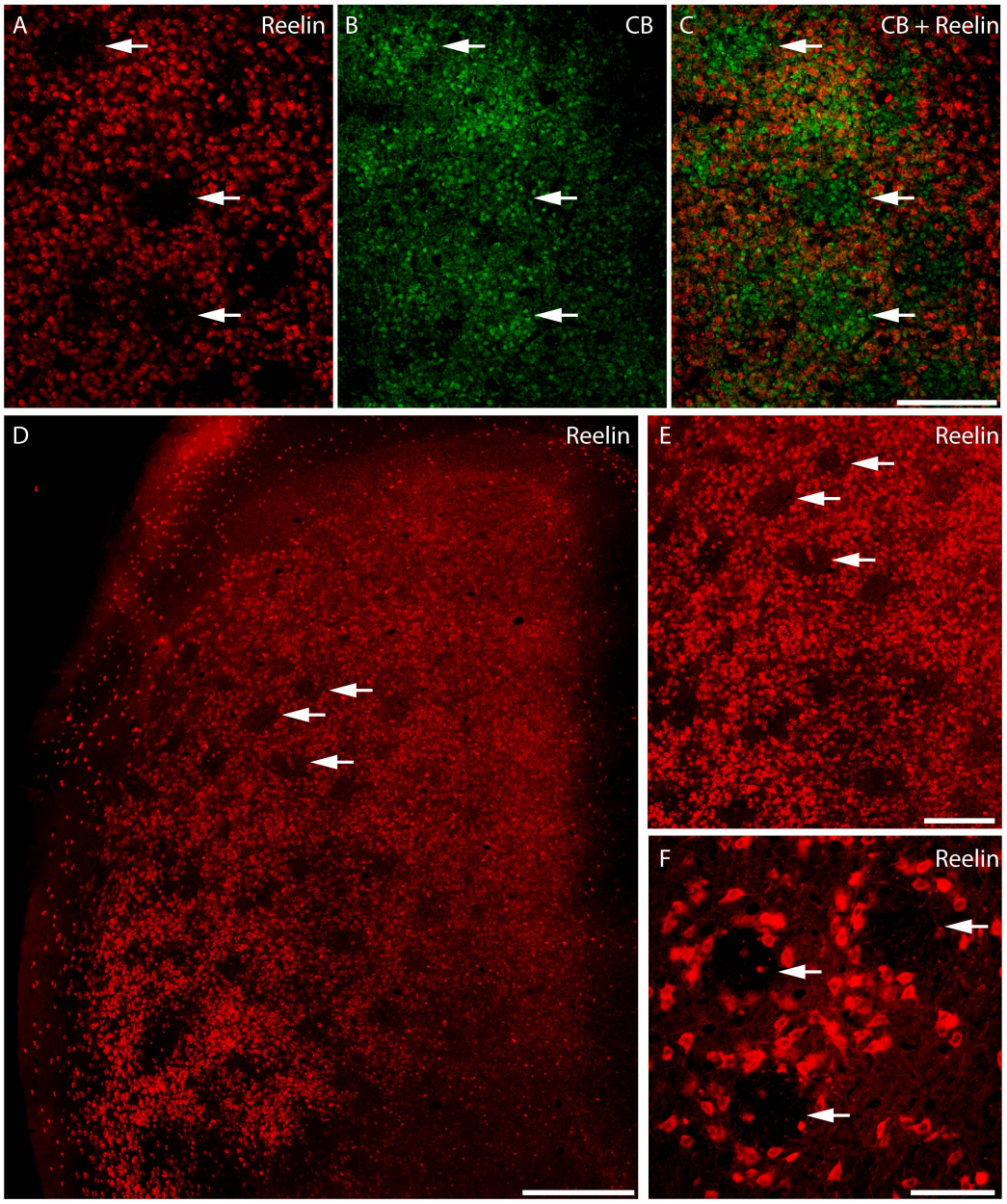

FIGURE 5.1: Reelin positive cells form a lattice surrounding calbindin patches. A, Tangential section through upper layer 2 of medial entorhinal cortex stained for reelin immunoreactivity. Neurons are densely distributed but leave out patches lacking reelin positive cells (arrows). B, Same section as in A co-stained for calbindin, showing calbindin patches. C, Overlay of A and B, showing non-overlapping distribution of reelin and calbindin positive cells. D, Tangential section stained for reelin immunoreactivity. This section includes a large part of upper layer 2 of medial entorhinal cortex and ventro-laterally the transition to lateral entorhinal cortex. The reelin positive cells leave out a regular array of (calbindin) patches (arrows). E, Higher magnification view of the same section as in D. F, Higher magnification view of a tangential section at the layer 1/2 border. Reelin positive cells form rings surrounding calbindin patches (arrows). Scale bars: C = 250 μm (also for A, B); D, E, F = 250 μm.

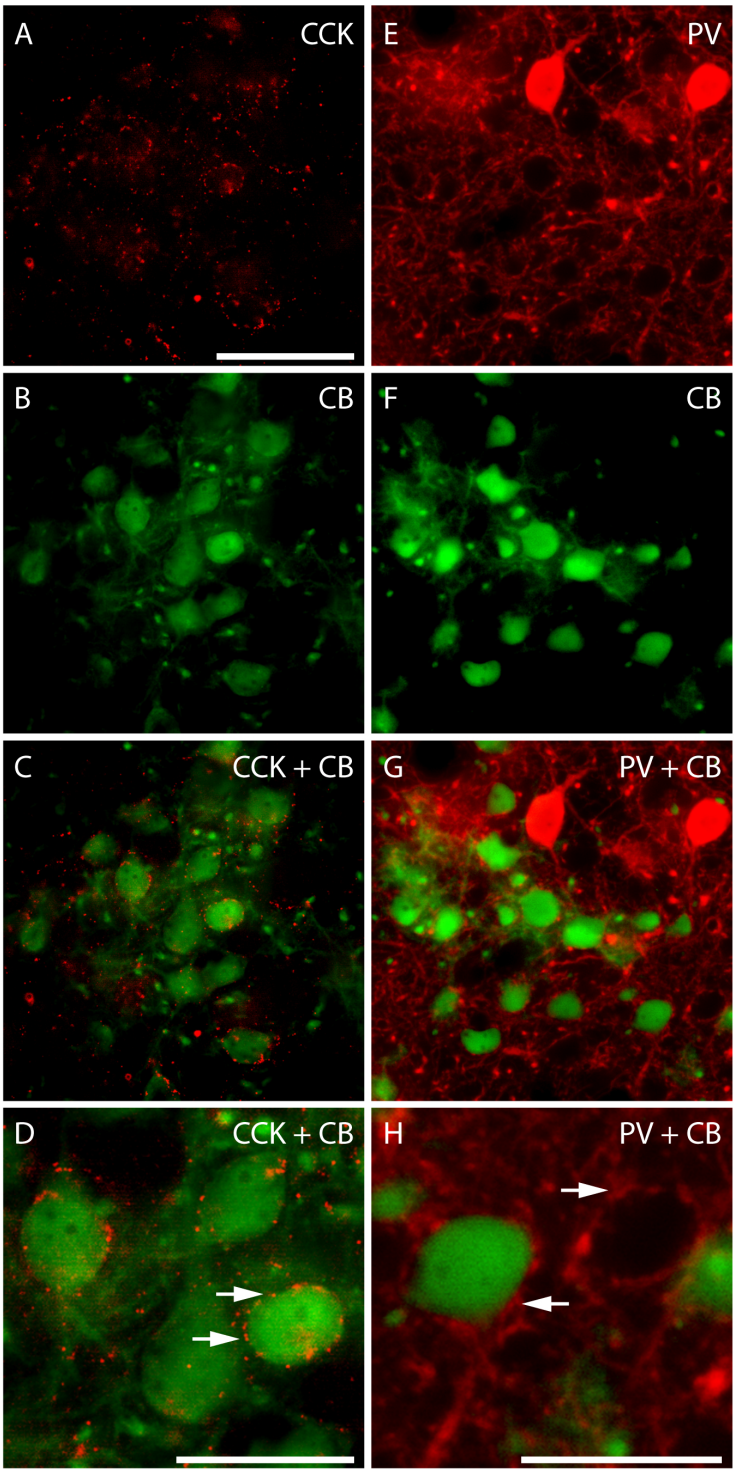

FIGURE 5.2: Calbindin positive and negative cells differ in innervation by basket cells. A, Tangential section stained for cholecystokinin. B, Same section as in A co-stained for calbindin, showing a calbindin patch. C, Overlay of A and B, showing overlap between cholecystokinin and calbindin staining patterns. D, High magnification view from C. Arrows indicate cholecystokinin immunoreactivity around calbindin positive cells. E, Tangential section stained for parvalbumin. F, Same section as in E co-stained for calbindin, showing a calbindin patch. G, Overlay of E and F, showing overlap between parvalbumin and calbindin staining patterns. H, High magnification view from G. Arrows indicate parvalbumin immunoreactivity around calbindin positive and negative cells. Scale bars: A = 50 μm (also for A, B, E, F, G); D, H = 25 μm.

5.3.3 Histochemical demonstration of an alternative pathway through layer 2 of medial entorhinal cortex

Based on overlapping modular organization of calbindin positive cells and acetylcholinesterase (Chapter 4) we asked how synaptic zinc is distributed in medial entorhinal cortex. Staining for synaptic zinc reveals a different kind of modular organization in medial entorhinal cortex (Fig. 5.3A). The staining intensity of synaptic zinc increases slowly from dorsal to ventral in medial entorhinal cortex and strongly in the transition to lateral entorhinal cortex (Haug, 1973). Staining the same section for calbindin immunoreactivity reveals discrete islands of calbindin positive cells (Fig. 5.3B), but higher magnification views show them to be largely nonoverlapping with increased staining for synaptic zinc (Figs. 5.3C, 5.3D, 5.3E). This relation is not as strict as the alignment of acetylcholinesterase and calbindin positive patches, especially in the most ventral part of medial entorhinal cortex that has a higher density of smaller zinc positive islands which in some cases overlap with calbindin patches. Figure 5.3F shows a sagittal section stained for synaptic zinc. There is little synaptic zinc in upper layer 1, somewhat irregularly sized patches of increased staining for synaptic zinc at the layer 1/2 border. Lower layer 2 shows low intensity of staining for synaptic zinc while it is high in layer 3. The same section stained for calbindin immunoreactivity (Fig. 5.3G) and the overlay (Fig. 5.3H) show that dendritic bundles formed by calbindin positive cells to a large extend avoid the regions of increased synaptic zinc staining.

5.3.4 Overlap of cytochrome oxidase patches and calbindin patches

A horizontal section through dorsal medial entorhinal cortex stained for NeuN, calbindin, and cytochrome oxidase activity is shown Figures 5.4A-D. In medial entorhinal cortex, calbindin positive cells align with increased cytochrome oxidase activity, although cytochrome oxidase activity is more widely spread than the more discrete calbindin patches. Staining for cytochrome oxidase in tangential sections usually has the appearance of a web of interconnected islands unlike the most commonly discrete patches of calbindin positive cells. Figures 5.4E-H show a more ventral horizontal section containing a part of (ventral) medial entorhinal cortex and lateral entorhinal cortex. The approximate border is indicated by a black triangle. In superficial layers of lateral entorhinal cortex calbindin positive and calbindin negative cells split into two different layers. Here only the upper, calbindin negative layer shows cytochrome oxidase activity (Fig. 5.4H).

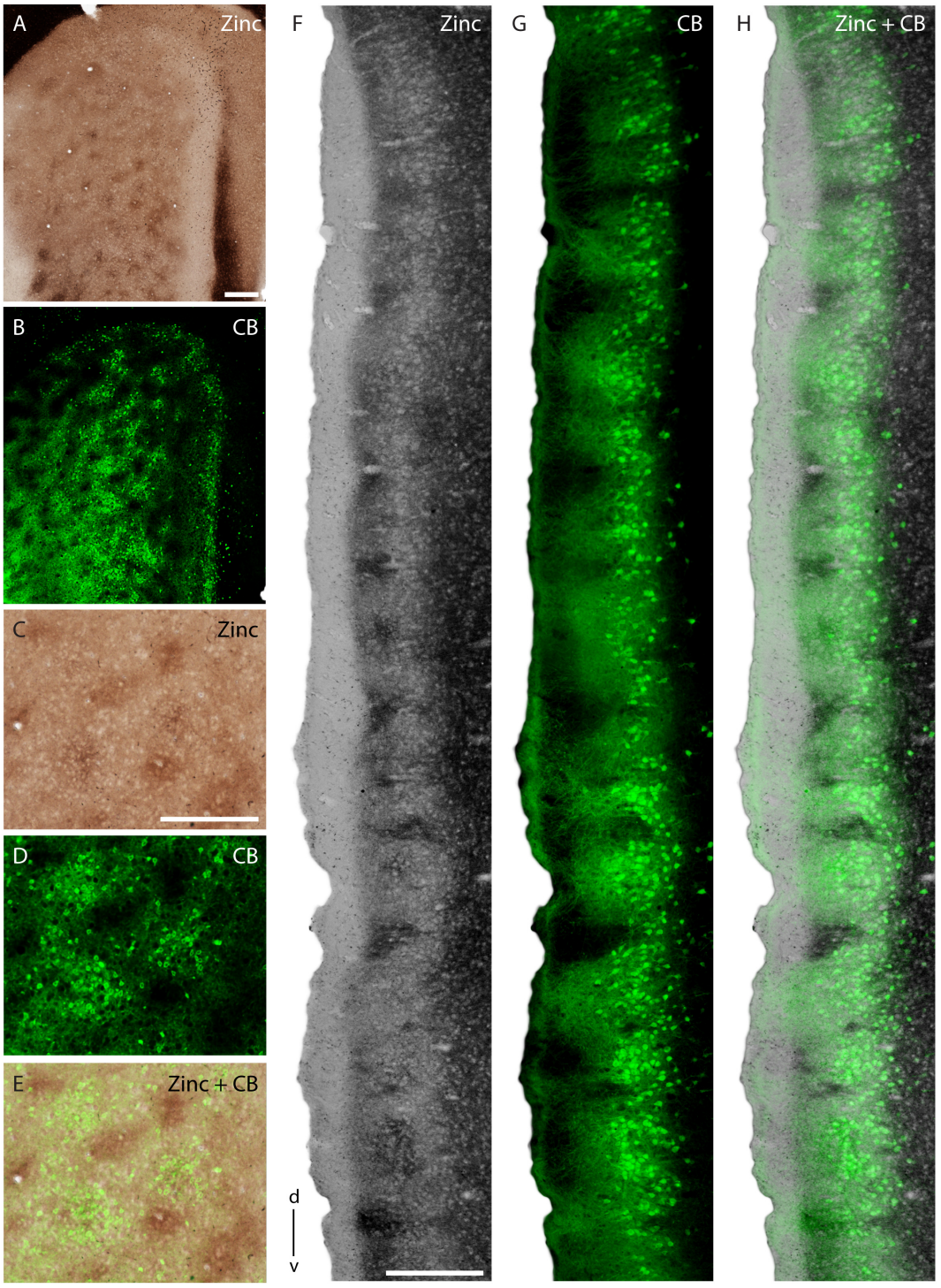

FIGURE 5.3: Relation of zinc positive modules to calbindin patches. A, Tangential section stained for synaptic zinc ions, showing discrete clusters of staining. B, Same section as in A co-stained for calbindin, showing calbindin patches. C, High magnification view from A. D, High magnification view from B. E, Overlay of C and D, showing largely non-overlapping zinc and calbindin staining patterns. F, Sagittal section stained for synaptic zinc ions, showing discrete clusters of staining. G, Same section as in F co-stained for calbindin, showing calbindin patches. H, Overlay of E and F, showing largely non-overlapping zinc and calbindin staining patterns. Scale bars: A = 250 μm (also for B); C = 250 μm (also for D, E); F = 250 μm (also for G, H). d = dorsal, v = ventral.

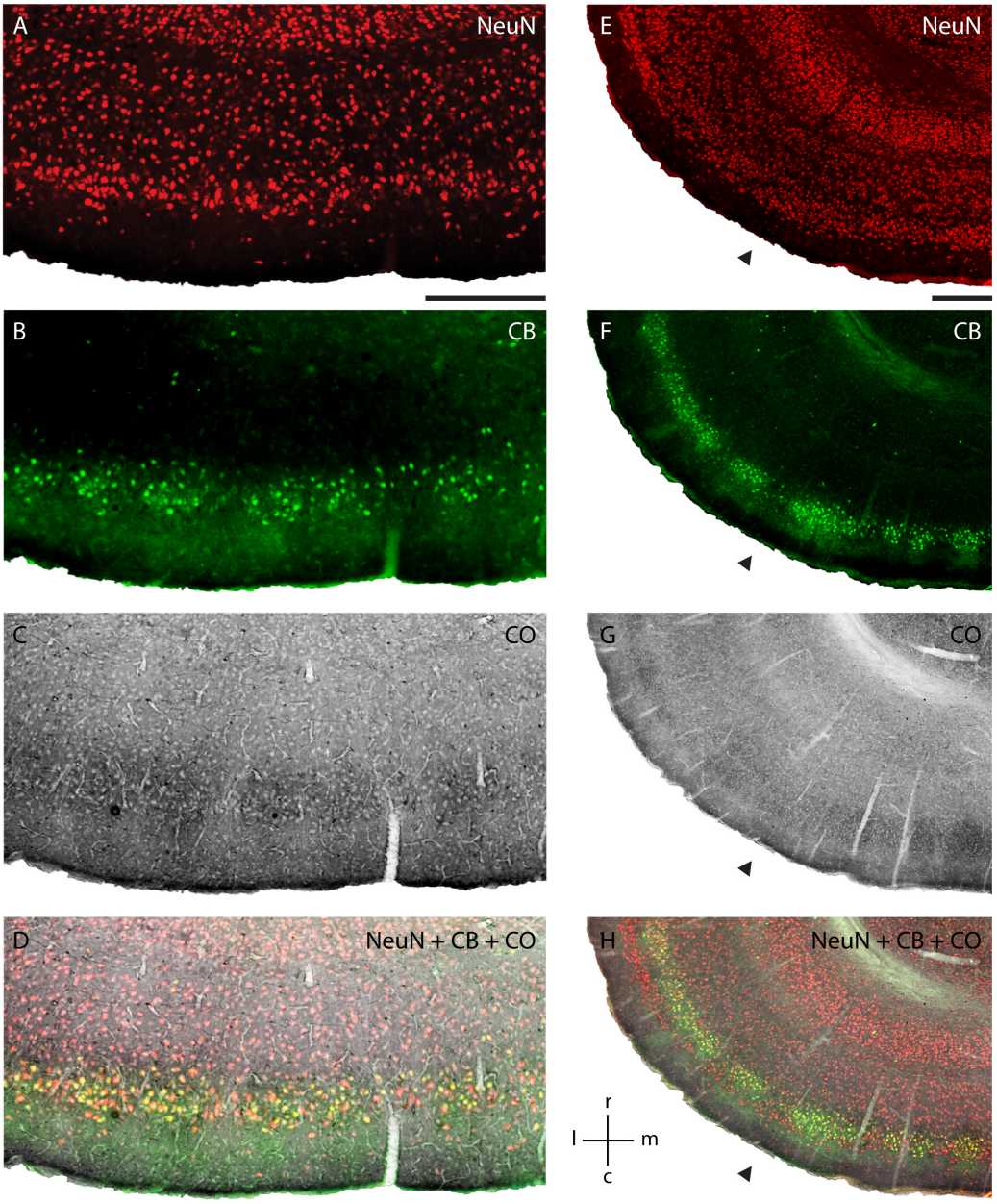

FIGURE 5.4: Relation of cytochrome oxidase modules to calbindin patches. A, Horizontal section through dorsal medial entorhinal cortex stained for NeuN. B, Same section as in A co-stained for calbindin, showing calbindin patches. C, Same section as in A stained for cytochrome oxidase (CO) activity, showing discrete clusters of staining. D, Overlay of A, B and C, showing overlap between the cytochrome oxidase activity and calbindin staining. E, Horizontal section through lateral and ventral medial entorhinal cortex stained for NeuN. The marker shows the approximate border between the areas. F, Same section as in E co-stained for calbindin, showing calbindin patches. G, Same section as in E stained for cytochrome oxidase activity, showing discrete clusters of staining. H, Overlay of A, B and C, showing overlap between the cytochrome oxidase activity and calbindin staining in ventral medial entorhinal cortex but not in later entorhinal cortex where the layer above the calbindin positive cells has higher cytochrome oxidase activity. Scale bars: A = 250 μm (also for B, C, D); E = 250 μm (also for F, G, H). l = lateral, m = medial, r = rostral, c = caudal.

5.3.5 Fiber systems in layer 1 of medial entorhinal cortex

The entorhinal cortex is connected with a multitude of cortical and subcortical regions (Witter et al., 1989). Here we describe different subsets of axons located in layer 1 of entorhinal cortex. These axons are best visible at the top or above the calbindin positive cell clusters. All of these different axon systems show the same preferred diagonal orientation while only a few axons run in an oblique direction. In general, fibres run parallel to the entorhinal / perirhinal border and orthogonal to the medial entorhinal / lateral entorhinal border while towards the parasubiculum they curve slightly ventral (Fig. 5.5A, 5.5B). Myelin staining shows a subset of fast-conducting axons. Dense myelin staining marks the medial entorhinal / parasubiculum border and the cellular clusters of the parasubiculum are surrounded by myelinated fibre bundles (Fig. 5.5A). Staining for acetylcholinesterase activity shows axon segments with the same preferred direction as the myelinated fibres (Fig. 5.5B). As shown previously, staining for vesicular acetylcholine transporter immunoreactivity shows a similar pattern of fibers and putative release sites of acetylcholine. The different fibres often run in between the calbindin patches. Staining for a certain fibre system and calbindin in the same section reveals that calbindin patches are ordered along the same direction as the fibre systems. This is illustrated for tyrosine hydroxylase containing fibres (Fig. 5.5C) and serotonergic fibres (Fig. 5.5D) in combination with calbindin staining using two-color immunohistochemistry. Axons were stained red-brown using peroxidase / DAB and calbindin positive cells were stained blue-black using alkaline phosphatase / tetrazolium blue. Figure 5.5C shows a higher magnification view of dorsal medial entorhinal cortex oriented in same way as the section above. Most of the tyrosine hydroxylase positive fibres are running in the same orientation as described for myelin but some can be seen entering calbindin patches or running in an oblique direction (Fig. 5.5C). Similarly, most serotonergic fibres are running in the same orientation as described for myelin but some can be seen entering calbindin patches or running in an oblique direction (Fig. 5.5D).

5.3.6 Overview of modular structures adjacent to entorhinal cortex

In occipital (or visual) cortex, zinc positive axon terminals at the border of layer 1 and 2 form a dense network of islands and elongated stripes (Ichinohe et al., 2003) that extends across the whole visual cortex (Fig. 5.6A). Retrosplenial granular cortex shows a pattern of a large number of small acetylcholinesterase positive islands of various shapes in deep layer 1 (Fig. 5.6B; Wyss et al., 1990). Immunohistochemical staining for M2 receptors shows a strikingly similar pattern (Fig. 5.6C). Towards more superficial layer 1 the sizes of the islands increase until they join to form a grid and finally a continuous

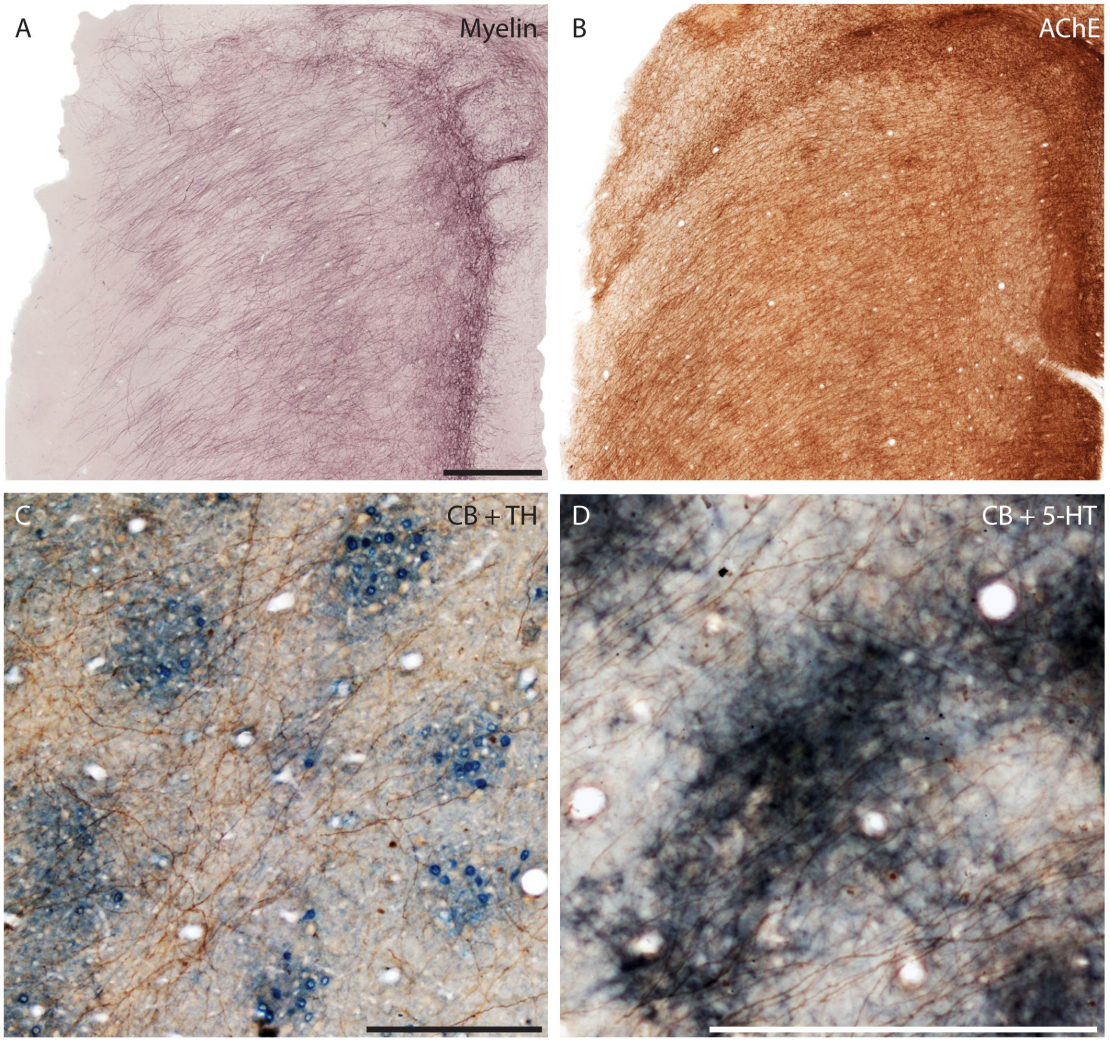

FIGURE 5.5: Axonal architecture in layer 1 of medial entorhinal cortex. A, Tangential section stained for myelinated axons. Myelin density is highest at the border of medial entorhinal cortex and parasubiculum and in between parasubicular modules. B, Tangential section stained for acetylcholinesterase activity. Clusters of acetylcholinesterase activity are only faintly visible in layer 1 compared with sections at the layer 1 / 2 border. C, Higher magnification view of a tangential section stained for calbindin (blue-black) and tyrosine hydroxylase (red-brown). D, Higher magnification view of a tangential section stained for calbindin (blue-black) and serotonin (5-HT, red-brown). Scale bars: A = 500 μm (also for B); C = 250 μm; D = 250 μm.

densely stained region at the surface of layer 1 (Wyss et al., 1990; Ichinohe, 2012). The presubiculum is organized into different cellular modules from early development on (Nishikawa et al., 2002) and contains clear cytochrome modules in adult animals (Gonzalez-Lima & Cada, 1998). These patches also stain for acetylcholinesterase (Fig. 5.6D) and NADPH diaphorase (Fig. 5.6E). They are surrounded by calbindin positive cells (Fig. 5.6F; Fujise et al., 1995) and in general contain very few neurons (Figs. 5.6G, 5.6H). As in retrosplenial granular cortex, M2 receptor neuropil staining in the presubiculum closely matched the modular distribution of acetylcholinesterase (data not shown). The border between parasubiculum and medial entorhinal cortex is marked by a semicircle of calbindin patches (Fig. 5.6I). This calbindin semicircle is located medial to intense staining for several markers such as acetylcholinesterase, zinc ions and cytochrome oxidase which have been classically used to define the border of the parasubiculum (Mathisen & Blackstad, 1964; Slomianka, 1992; Burgalossi et al., 2011). The "patch free zone" between the outer semicircle of calbindin cells and the medial calbindin patches described in Chapter 4 consists of two parts. In the more lateral part calretinin positive cells in layer 3 and layer 2 and their dendrites form discrete clusters along the dorso-ventral axis (Fig. 5.6J; Fujimaru & Kosaka, 1996; Miettinen et al., 1997). The more medial part consists of densely packed neurons and contains an increased density of parvalbumin positive cells and neuropil (Fig. 5.6K). Burgalossi et al. (2011) estimated that there are 25 parasubicular patches. The discrete structure of parasubicular patches is evident in superficial sections stained for cytochrome oxidase (Burgalossi et al., 2011), myelin showing the septae of the patches (Fig. 5.5A; Burgalossi et al., 2011) or parvalbumin (Figs. 5.6K). Figure 5.6L shows an overlay of Figures 5.6I, 5.6J, 5.6K illustrating the transition from medial entorhinal cortex calbindin patches (lateral), calretinin patches, increased density of parvalbumin neuropil, again calbindin patches and finally parvalbumin positive parasubicular patches (medial).

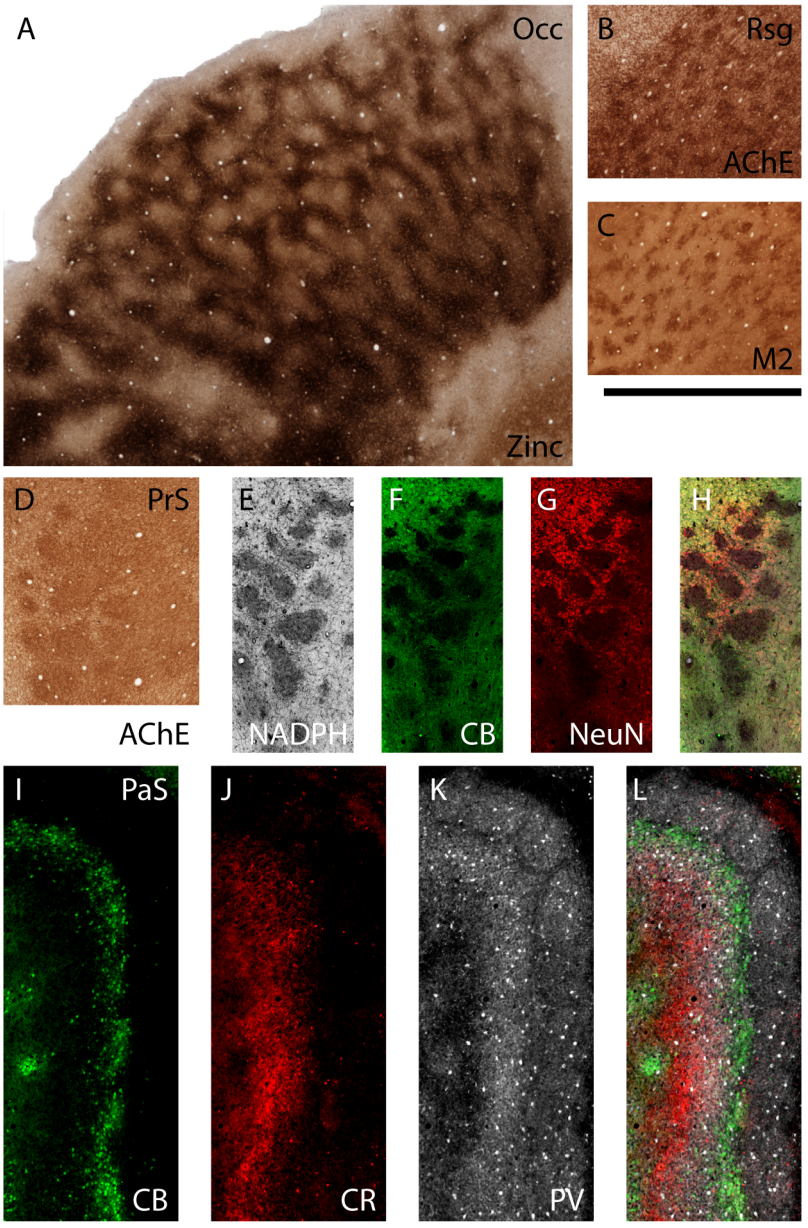

FIGURE 5.6: Overview of modular structures adjacent to entorhinal cortex. A, Tangential section at the layer 1/2 border of occipital (visual) cortex stained for synaptic zinc. B, Tangential section at the layer 1/2 border of retrosplenial granular cortex stained for acetylcholinesterase activity. C, Tangential section at the layer 1/2 border of retrosplenial granular cortex stained for M2 acetylcholine receptor immunoreactivity. D, Tangential section at the layer 1/2 border of presubiculum stained for acetylcholinesterase activity. E, Tangential section at the layer 1/2 border of presubiculum stained for NADPH diaphorase activity. F, Tangential section at the layer 1/2 border of presubiculum stained for calbindin. G, Tangential section at the layer 1/2 border of presubiculum stained for NeuN. H, Overlay of E, F, G. I, Tangential section at the layer 1/2 border of parasubiculum stained for calbindin. J, Tangential section at the layer 1/2 border of parasubiculum stained for calretinin. K, Tangential section at the layer 1/2 border of parasubiculum stained for parvalbumin. L, Overlay of I, J, K. Scale bars: C = 1 mm (also for A, B, D, E, F, G, H, I, J, K, L).

5.4 Discussion

Understanding the functional anatomy of medial entorhinal cortex requires integrating information at the level of microcircuits, modular structures and interareal connectivity. Figure 5.7 summarizes current knowledge about microcircuits (Burgalossi & Brecht, 2014). Reelin positive stellate cells and calbindin positive pyramidal cells are the major principal cells of layer 2 of medial entorhinal cortex (Varga et al., 2010). They differ in their innervation by basket cells: parvalbumin positive processes surround both calbindin positive and reelin positive cells whereas cholecystokinin positive processes only surround calbindin positive cells (Varga et al., 2010; Armstrong & Soltesz, 2012). Cholecystokinin and parvalbumin positive presynaptic processes form opposing density gradients along the dorso-ventral axis (Köhler & Chan-Palay, 1982; Beed et al., 2013), which may correlate with the constant overall density of GABAergic preterminal elements (Beed et al., 2013). Stellate cells excite inhibitory cells which in turn inhibit other stellate cells (Couey et al., 2013). The interneurons are likely to be parvalbumin positive due to the high density of parvalbumin positive cells compared to other inhibitory cells and the matching high probability of connections (Couey et al., 2013). Both pyramidal and stellate cells receive excitatory intralaminar input (Kumar et al., 2007; Beed et al., 2010). Stellate cells do not form excitatory connections to other stellate cells (Dhillon & Jones, 2000; Pastoll et al., 2013; Couey et al., 2013) but may form excitatory connections to pyramidal cells (Pastoll et al., 2013; Couey et al., 2013), whereas pyramidal cells are the likely source of excitatory input to stellate cells and other pyramidal cells (Beed et al., 2010; Couey et al., 2013). This is a likely scenario, since isocortical pyramidal cell microcircuits have recurrent excitatory connections (DeFelipe & Jones, 2010), although these circuits have not been described quantitatively. Also, direct evidence for connectivity among calbindin positive pyramidal cells of layer 2 of medial entorhinal cortex is lacking. In addition, a third non-GABAergic cell type has been described: calretinin positive neurons. These cells are few in number in the medial entorhinal cortex and although calretinin has been described as an interneuron marker, most of them are excitatory (Wouterlood et al., 2000; Wouterlood et al., 2008). The morphology and physiology has not yet been studied in detail.

5.4.1 Cholinergic and zincergic input to superficial layers of medial entorhinal cortex

Previous descriptions of modular distribution of histochemical markers in superficial layers of medial entorhinal cortex of rodents include clusters of calbindin positive cells (Fujimaru & Kosaka, 1996), zinc positive terminals (Slomianka & Geneser, 1997) and

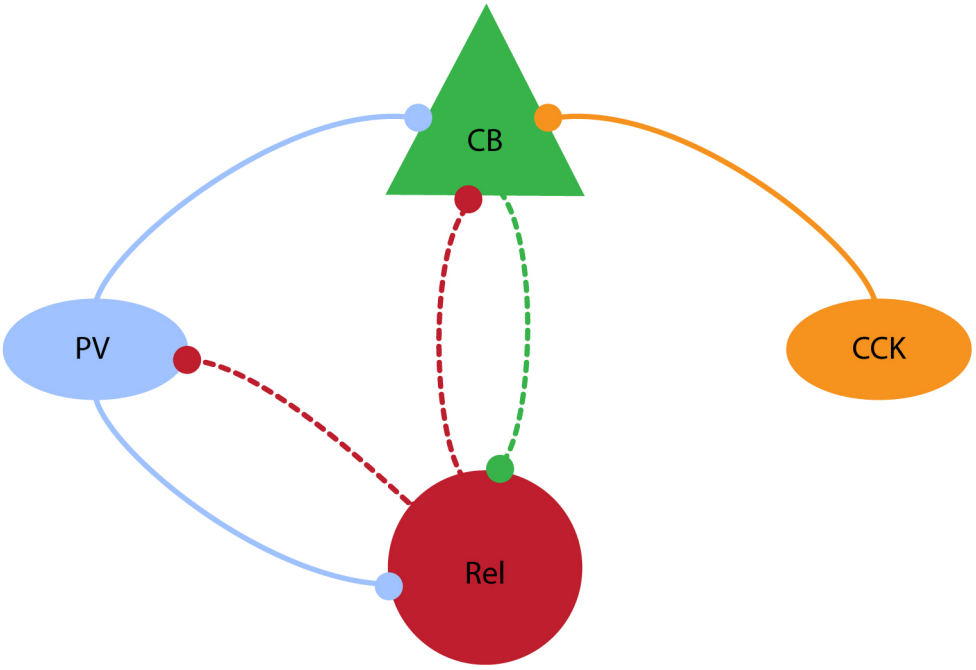

FIGURE 5.7: Schematic microcircuit of layer 2 in medial entorhinal cortex. Parvalbumin (PV, blue connections) positive neurons innervate both reelin (Rel) positive and calbindin (CB) positive neurons whereas cholecystokinin (CCK, orange connection) positive neurons only innervate calbindin positive neurons. Putative reelin positive stellate cells do not excite other stellate cells but may excite parvalbumin and calbindin positive cells (dashed red connections). Putative calbindin positive pyramidal cells may excite other stellate and pyramidal cells (dashed green connection).

acetylcholinesterase patches (Slomianka & Geneser, 1991), yet the interrelation of these different markers was unknown. These techniques employ conventional light microscopy which does not allow visualization of synaptic contacts. Still, it is possible to infer connectivity by staining specific presynaptic and postsynaptic elements. High densities of such dendrites and axons in a given region imply a high probability of connections between these elements. This is known as "Peters' rule" and is based on the assumption that axons target dendrites locally in a random fashion (Peters & Feldman, 1976; Braitenberg & Schüz, 1991; Helmstaedter & Feldmeyer, 2010). Exceptions to Peters' rule are common, for example some retrohippocampal afferents have a selective terminal distribution in superficial layers of medial entorhinal cortex but still contact cells from all layers monosynaptically (Canto et al., 2012). Since calbindin positive dendritic bundles overlap with markers of cholinergic axon terminals we would predict a high probability of connections. Cholinergic activation slightly modulates stellate cell activity but dramatically changes pyramidal cell firing properties from regular tonic firing into a slow repetitive bursting mode (Klink & Alonso, 1997). We found that calbindin positive cells are more theta modulated than calbindin negative cells which may correlate with the increased density of cholinergic terminals surrounding calbindin positive cells. We have shown an alternative pathway through medial entorhinal cortex which could be

mediated by zinc positive axon terminals. They are preferentially concentrated outside of calbindin patches and overlap with a fraction of the reelin positive cells. Yet reelin positive cells are not known to form dendritic bundles in between calbindin patches and no physiological correlate of zincergic input to medial entorhinal cortex has been discovered.

5.4.2 Relation of reelin and calbindin positive cells to cytochrome oxidase patches

We found that cytochrome oxidase patches in entorhinal cortex (Burgalossi et al., 2011) are overlapping with calbindin patches in medial entorhinal cortex but overlap with calbindin negative patches in lateral entorhinal cortex (Fig. 5.4D, 5.4H). In addition, staining for cytochrome oxidase activity in medial entorhinal cortex usually stains a wider area than that covered by calbindin patches including at least part of the lattice of reelin positive cells. Since calbindin patches also contain calbindin negative cells, further studies are necessary to decide whether calbindin positive or calbindin negative cells have a higher cytochrome oxidase activity.

5.4.3 Overview of modular structures in the parahippocampal region

Cholinergic and zincergic modules are not exclusive to medial entorhinal cortex. In several adjacent areas such as retrosplenial granular cortex and presubiculum acetylcholinesterase staining shows a strikingly modular distribution. Curiously, the same is true for several distant brain regions, such as the superior colliculus (Chevalier & Mana, 2000) or the striatum (Graybiel & Ragsdale, 1978) where acetylcholinesterase is also colocalized with calbindin positive cells (Gerfen et al., 1985). However, it is not known whether these circuit elements would enable similar functions in these different brain regions. In the basal forebrain, where many cholinergic fibres originate, cholinergic cells form hundreds of distinct clusters (Zaborszky, 2002; Nadasdy et al., 2010; Zaborszky et al., 2012), but at present it is not known how they relate to modular terminations of cholinergic fibres in the entorhinal cortex or elsewhere. Staining acetylcholinesterase activity in retrosplenial granular cortex and presubiculum reveals distinct clusters as in medial entorhinal cortex but also reveals a number of differences: 1. Each area has a distinct density and distribution of acetylcholinesterase activity clusters. 2. Medial entorhinal cortex does not show a matching M2 receptor distribution (data not shown; Rouse & Levey 1996; Wang & Burkhalter 2011). 3. Calbindin positive cells in presubiculum form a lattice surrounding acetylcholinesterase activity clusters, whereas there are few calbindin positive cells in superficial layers of retrosplenial granular cortex. Figure

5.8A reviews the areal and modular organization of superficial layers of the entorhinal cortex and adjacent cortical areas. Modular structures in medial entorhinal cortex, parasubiculum, presubiculum, retrosplenial granular cortex and occipital cortex were drawn from sections from Chapter 4 and 5 which were aligned at the entorhinal / parasubicular border. Figure 5.8B shows an idealized scheme of the modular architecture of medial entorhinal cortex and the adjacent parasubiculum adapted from Figure 3 of Witter & Moser (2006). Modular structures in layer 1 and 2 are depicted in a simplified way on the surface and the sides of layer 2. Calretinin cells form translaminar clusters with the highest density of cells in layer 3 (Miettinen et al., 1997). Pyramidal cells in layer 3 and 5 are displayed as in Figure 3 of Witter & Moser (2006); they form dendritic bundles which are assumed to terminate in between calbindin patches (Hamam et al., 2000; van Haeften et al., 2003; Wouterlood et al., 2004; Witter & Moser, 2006).

5.4.4 Modular connectivity

While the area-to-area connectivity is relatively well-known in the entorhinal cortex (Witter et al., 1989; van Strien et al., 2009) and recent progress in serial section electron microscopy (Denk et al., 2012) may soon reveal the entire connectivity within one entorhinal module, very little is known about connectivity at an intermediate scale (Bohland et al., 2009). How are groups of neurons such as calbindin positive cells in entorhinal modules connected to neighbouring modules or to modules in neighbouring cortical areas?

5.4.5 Connections from Presubiculum and Parasubiculum

Köhler (1985) traced inputs from the presubiculum and parasubiculum to the medial entorhinal cortex and found them to terminate in modular alternating clusters (red and blue arrows in Fig. 5.9). Staining projections from presubiculum labels preferentially axons in layer 3 and layer 1 and thin septa in layer 2 while projections from parasubiculum terminate in relatively large clusters in layer 2 (Witter et al., 1989; van Groen & Wyss, 1990). Small injections into the presubiculum do not label the entire medial entorhinal cortex but rather a band in dorsal medial entorhinal cortex orthogonal to the border of medial and lateral entorhinal cortex (Honda & Ishizuka, 2004). Although projections from superficial layers of presubiculum predominantly terminate in superficial layers of medial entorhinal cortex (Köhler, 1985), they also contact apical dendrites of layer 5 pyramidal cells (Wouterlood et al., 2004). Taken together, we hypothesize that the parasubicular afferents preferentially target calbindin patches, whereas presubicular afferents preferentially target the space in between. This is supported at the single cell

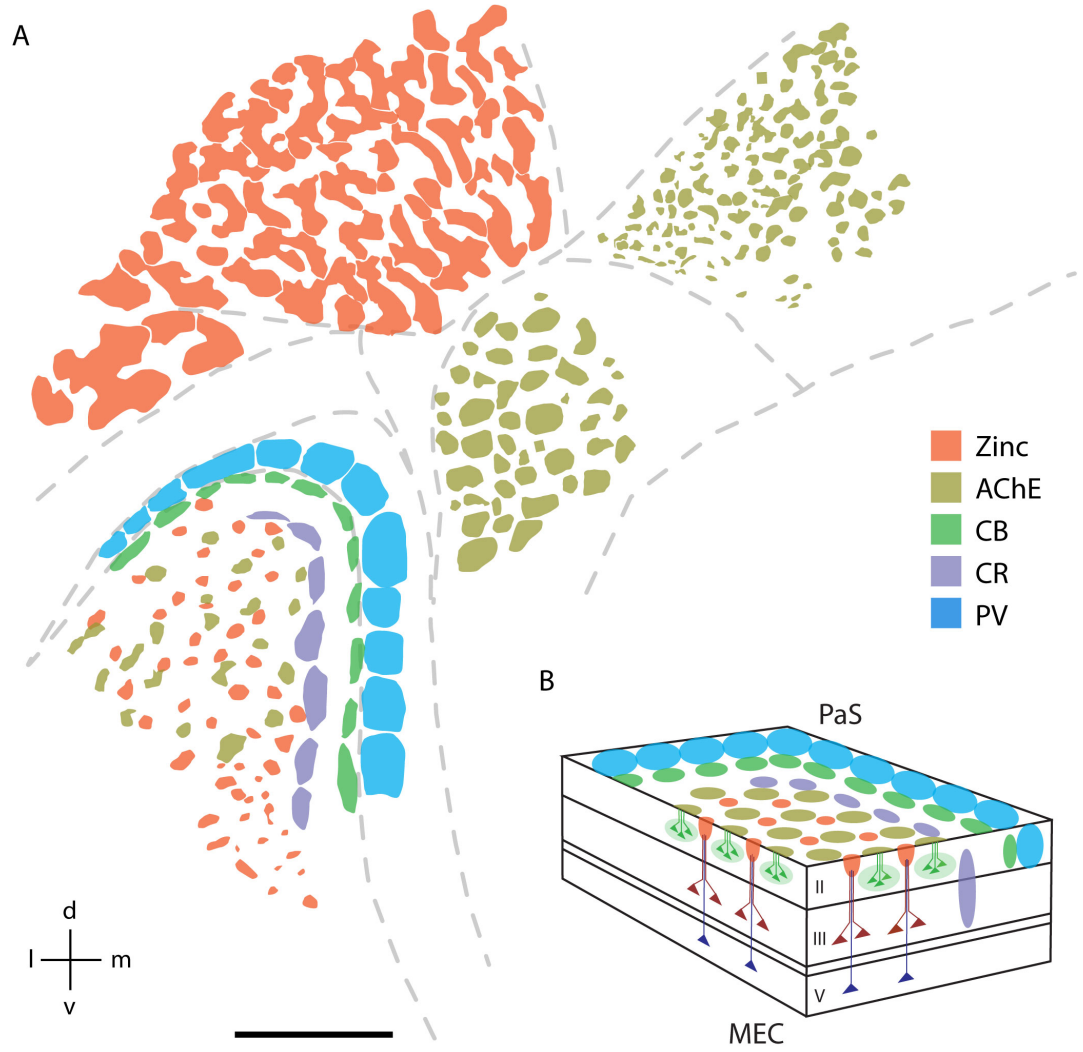

FIGURE 5.8: Overview of modular structures in the superficial layers of medial entorhinal cortex and neighboring regions. A, Overview of modular structures in the superficial layers of medial entorhinal cortex and neighboring regions. Sections stained for different markers were aligned at the entorhinal / parasubicular border and modular structures drawn. B, Schematic illustration of modular structures in the dorsal medial entorhinal cortex and parasubiculum, adapted from Witter & Moser (2006) Scale bars: A = 1 mm.

level by the identification of "centripetal" axons that originate in large parasubicular patches and target medial entorhinal patches (Burgalossi et al., 2011).

5.4.6 Input of diverse transmitter systems to the entorhinal cortex

Several transmitter systems send strong projections to the entorhinal cortex (green arrows in Fig. 5.9). Serotonergic fibres originate in the midbrain raphe nuclei, enter the entorhinal cortex predominantly from a ventral direction and curve towards the parasubiculum (Köhler et al., 1981). Cholinergic fibres originate in the medial septum and

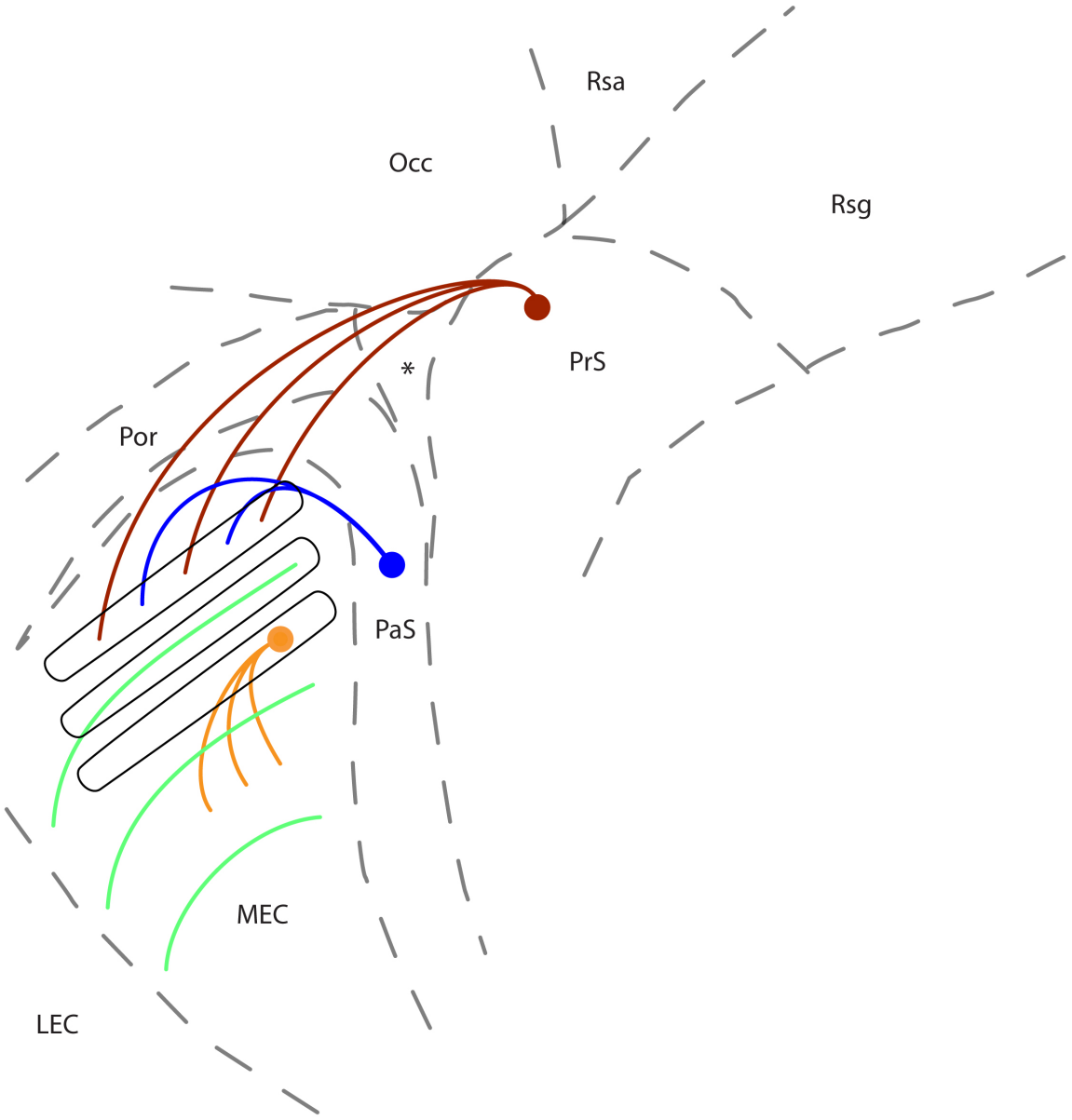

FIGURE 5.9: Modular connectivity of the entorhinal region. A schematic illustration shows connections from superficial layers of presubiculum (red) and parasubiculum (blue) to superficial layers of entorhinal cortex. Injections at one point in presubiculum or parasubiculum label a band of sites in medial entorhinal cortex orthogonal to the lateral / medial entorhinal cortex border. Different fibres in layer 1 of entorhinal cortex such as serotonergic, myelinated, cholinergic or tyrosine hydroxylase positive axons are indicated in green. Intrinsic connections from deep to superficial layers of entorhinal cortex are labeled orange. Three black outlines show putative modules containing grid cells of the same size. They are oriented parallel to one axis of the calbindin patches, the preferred direction of layer 1 fibres and the bands of inputs from presubiculum and parasubiculum.

project to entorhinal cortex (Alonso & Köhler, 1984), but also GABAergic (Köhler et al., 1984) and glutamatergic basal forebrain neurons (Manns et al., 2001) project to entorhinal cortex. Axonal terminals containing cholecystokinin, parvalbumin and zinc have been demonstrated in superficial layers of entorhinal cortex but their origin has not been traced. Cholecystokinin and parvalbumin positive terminals likely originate locally; neurons containing these markers are present in entorhinal cortex (Köhler, 1986 a). Very few zinc-containing neurons have been found in entorhinal cortex; all of them in deep layers (Slomianka, 1992). The zinc positive terminals in layer 2 of entorhinal cortex may originate in the pre - and parasubiculum, because the appearance of zinc staining in superficial layer of entorhinal cortex coincides with the appearance of many zinc-containing cells in the pre- and parasubiculum (Slomianka & Geneser, 1997).

5.4.7 Intraentorhinal modular connectivity

Injections of anterograde tracers in deep layers of MEC reveal an intraentorhinal projection pattern to several modules of superficial entorhinal cortex at a more ventral level (Köhler, 1986 b; orange arrows in Fig. 9). Layer 2 entorhinal stellate and pyramidal cells have axon collaterals projecting to superficial layers (Lorente de No, 1933; Klink & Alonso, 1997). These axon collaterals usually branch off from a descending axon and reenter superficial layers only at a considerable distance (Lorente de No, 1933). In a recent study Burgalossi et al., (2011) found that 15 out of 18 well labeled cells in superficial layers of medial entorhinal cortex had a “centrifugal” axon. These axons travel for a long distance and target a single large patch in the parasubiculum (Burgalossi et al., 2011).

In summary, we propose that several patches aligned along the axis of preferred direction of fibres in layer 1 and with similar inputs from presubiculum and parasubiculum form discrete modules (black outlines in Fig. 9). These modules may correspond to functional modules.

5.5 References

Airaksinen, M. S., Eilers, J., Garaschuk, O., Thoenen, H., Konnerth, A., & Meyer, M. (1997). Ataxia and altered dendritic calcium signaling in mice carrying a targeted null mutation of the calbindin D28k gene. Proceedings of the National Academy of Sciences, 94(4), 1488-1493.

Alonso, A., & Klink, R. (1993). Differential electroresponsiveness of stellate and pyramidal-like cells of medial entorhinal cortex layer II. Journal of Neurophysiology, 70(1), 128-143.

Alonso, A., & Köhler, C. (1984). A study of the reciprocal connections between the septum and the entorhinal area using anterograde and retrograde axonal transport methods in the rat brain. Journal of Comparative Neurology, 225(3), 327-343.

Alonso, A., & Llinás, R. R. (1989). Subthreshold Na+-dependent theta-like rhythmicity in stellate cells of entorhinal cortex layer II. Nature, 342(6246), 175-177.

Armstrong, C., & Soltesz, I. (2012). Basket cell dichotomy in microcircuit function. The Journal of Physiology, 590(4), 683-694.

Barry, C., Hayman, R., Burgess, N., & Jeffery, K. J. (2007). Experience-dependent rescaling of entorhinal grids. Nature neuroscience, 10(6), 682-684.

Beed, P., Gundlfinger, A., Schneiderbauer, S., Song, J., Böhm, C., Burgalossi, A., ... & Schmitz, D. (2013). Inhibitory Gradient along the Dorsoventral Axis in the Medial Entorhinal Cortex. Neuron, 79(6), 1197-1207.

Blackstad, T. W. (1956). Commissural connections of the hippocampal region in the rat, with special reference to their mode of termination. Journal of Comparative Neurology, 105(3), 417-537.

Bohland, J. W., Wu, C., Barbas, H., Bokil, H., Bota, M., Breiter, H. C., ... & Mitra, P. P. (2009). A proposal for a coordinated effort for the determination of brainwide neuroanatomical connectivity in model organisms at a mesoscopic scale. PLoS computational biology, 5(3), e1000334.

Bombardi, C., Grandis, A., Nenzi, A., Giurisato, M., & Cozzi, B. (2010). Immunohistochemical localization of substance P And cholecystokinin in the dorsal root ganglia and spinal cord of the bottlenose dolphin (Tursiops truncatus). The Anatomical Record, 293(3), 477-484

Braitenberg V, Schüz A (1991) Peters' Rule and White's Exceptions. In: Anatomy of the Cortex, pp 109-112. Berlin: Springer.

Brun, V. H., Solstad, T., Kjelstrup, K. B., Fyhn, M., Witter, M. P., Moser, E. I., & Moser, M. B. (2008). Progressive increase in grid scale from dorsal to ventral medial entorhinal cortex. Hippocampus, 18(12), 1200-1212.

Burgalossi, A., Herfst, L., von Heimendahl, M., Förste, H., Haskic, K., Schmidt, M., & Brecht, M. 2011 Microcircuits of functionally identified neurons in the rat medial entorhinal cortex. Neuron 70, 773-786.

Burgalossi, A., & Brecht, M. (2014). Cellular, columnar and modular organization of spatial representations in medial entorhinal cortex. Current Opinion in Neurobiology, 24, 47-54.

Canto, C. B., Koganezawa, N., Beed, P., Moser, E. I., & Witter, M. P. (2012). All Layers of Medial Entorhinal Cortex Receive Presubicular and Parasubicular Inputs. The Journal of Neuroscience, 32(49), 17620-17631.

Canto, C. B., & Witter, M. P. (2012). Cellular properties of principal neurons in the rat entorhinal cortex. II. The medial entorhinal cortex. Hippocampus, 22(6), 1277-1299.

Celio, M. R., Baier, W., Schärer, L., Gregersen, H. J., De Viragh, P. A., & Norman, A. W. (1990). Monoclonal antibodies directed against the calcium binding protein Calbindin D-28k. Cell Calcium, 11(9), 599-602.

Chevalier, G., & Mana, S. (2000). Honeycomb-like structure of the intermediate layers of the rat superior colliculus, with additional observations in several other mammals: AChE patterning. Journal of Comparative Neurology, 419(2), 137-153.

Couey, J. J., Witoelar, A., Zhang, S. J., Zheng, K., Ye, J., Dunn, B., ... & Witter, M. P. (2013). Recurrent inhibitory circuitry as a mechanism for grid formation. Nature neuroscience.

Croft, B. G., Fortin, G. D., Corera, A. T., Edwards, R. H., Beaudet, A., Trudeau, L. E., & Fon, E. A. (2005). Normal biogenesis and cycling of empty synaptic vesicles in dopamine neurons of vesicular monoamine transporter 2 knockout mice. Molecular biology of the cell, 16(1), 306-315

da Costa, N. M., & Martin, K. A. (2010). Whose cortical column would that be?. Frontiers in neuroanatomy, 4.

Danscher G. 1981. Histochemical demonstration of heavy metals. A revised version of the sulphide silver method suitable for both light and electron microscopy. Histochemistry. 71: 1-16.

DeFelipe, J. (1997). Types of neurons, synaptic connections and chemical characteristics of cells immunoreactive for calbindin-D28K, parvalbumin and calretinin in the neocortex. Journal of chemical neuroanatomy, 14(1), 1-19.

DeFelipe, J., & Jones, E. G. (2010). Neocortical microcircuits. Handbook of Brain Microcircuits, 5-14.

Denk, W., Briggman, K. L., & Helmstaedter, M. (2012). Structural neurobiology: missing link to a mechanistic understanding of neural computation. Nature Reviews Neuroscience, 13(5), 351-358.

Dhillon, A., & Jones, R. S. (2000). Laminar differences in recurrent excitatory transmission in the rat entorhinal cortex in vitro. Neuroscience, 99(3), 413-422.

Fujimaru, Y. & Kosaka, T. 1996 The distribution of two calcium binding proteins, calbindin D-28K and parvalbumin, in the entorhinal cortex of the adult mouse. Neurosci Res. 24, 329-43.

Fujise, N., Hunziker, W., Heizmann, C. W., & Kosaka, T. (1995). Distribution of the calcium binding proteins, calbindin D-28K and parvalbumin, in the subicular complex of the adult mouse. Neuroscience research, 22(1), 89-107.

Geffard, M., Dulluc, J., & Rock, A. M. (1985). Antisera Against the Indolealkylamines: Tryptophan, 5-Hydroxytryptophan, 5-Hydroxytryptamine, 5-Methoxytryptophan, and 5-Methoxytryptamine Tested by an Enzyme-Linked Immunosorbent Assay Method. Journal of neurochemistry, 44(4), 1221-1228

Gerfen, C. R., Baimbridge, K. G., & Miller, J. J. (1985). The neostriatal mosaic: compartmental distribution of calcium-binding protein and parvalbumin in the basal ganglia of the rat and monkey. Proceedings of the National Academy of Sciences, 82(24), 8780-8784.

Gonzalez-Lima & Cada, 1998. Quantative histochemistry of cytochrome oxidase. In: Cytochrome Oxidase in Neuronal Metabolism and Alzheimer's Disease. Gonzalez-Lima ed. Springer.

Graybiel, A. M., & Ragsdale, C. W. (1978). Histochemically distinct compartments in the striatum of human, monkeys, and cat demonstrated by acetylthiocholinesterase staining. Proceedings of the National Academy of Sciences, 75(11), 5723-5726.

Hafting, T., Fyhn, M., Molden, S., Moser, M.B. & Moser, E.I. 2005 Microstructure of a spatial map in the entorhinal cortex. Nature 436, 801-6.

Hamam, B. N., Kennedy, T. E., Alonso, A., & Amaral, D. G. (2000). Morphological and electrophysiological characteristics of layer V neurons of the rat medial entorhinal cortex. Journal of Comparative Neurology, 418(4), 457-472.

Haug, F. M. S. (1973). Heavy metals in the brain. A light microscope study of the rat with Timm's sulphide silver method. Methodological considerations and cytological and regional staining patterns. Advances in anatomy, embryology, and cell biology, 47(4):1-71.

Hayes, T. L., & Lewis, D. A. (1992). Nonphosphorylated neurofilament protein and calbindin immunoreactivity in layer III pyramidal neurons of human neocortex. Cerebral cortex, 2(1), 56-67.

Helmstaedter, M., & Feldmeyer, D. (2010). Axons predict neuronal connectivity within and between cortical columns and serve as primary classifiers of interneurons in a cortical column. In New Aspects of Axonal Structure and Function (pp. 141-155). Springer.

Honda, Y., & Ishizuka, N. (2004). Organization of connectivity of the rat presubiculum: I. Efferent projections to the medial entorhinal cortex. Journal of Comparative Neurology, 473(4), 463-484.

Horton, J. C., & Adams, D. L. (2005). The cortical column: a structure without a function. Philosophical Transactions of the Royal Society B: Biological Sciences, 360(1456), 837-862.

Ichinohe, N. 2012 Small-scale module of the rat granular retrosplenial cortex: an example of the minicolumn-like structure of the cerebral cortex. Front Neuroanat. 5, 69. doi: 10.3389/fnana.2011.00069.

Ichinohe, N., Fujiyama, F., Kaneko, T., & Rockland, K. S. (2003). Honeycomb-like mosaic at the border of layers 1 and 2 in the cerebral cortex. The Journal of neuroscience, 23(4), 1372-1382.

Ichinohe N., Knight A., Ogawa M., Ohshima T., Mikoshiba K., Yoshihara Y., Terashima T., Rockland K. S. (2008). Unusual patch-matrix organization in the retrosplenial cortex of the reeler mouse and shaking rat Kawasaki. Cereb. Cortex 18, 1125-1138. doi: 10.1093/cercor/bhm148.

Ichinohe, N., & Rockland, K. S. (2004). Region specific micromodularity in the uppermost layers in primate cerebral cortex. Cerebral Cortex, 14(11), 1173-1184.

Klink, R., & Alonso, A. (1997). Morphological characteristics of layer II projection neurons in the rat medial entorhinal cortex. Hippocampus, 7(5), 571-583.

Köhler, C. (1985). Intrinsic projections of the retrohippocampal region in the rat brain. I. The subicular complex. Journal of Comparative Neurology, 236(4), 504-522.

Köhler, C. (1986 a). Cytochemical architecture of the entorhinal area. Excitatory Amino Acids and Epilepsy. Advances in Experimental Medicine and Biology Volume 203, 1986, pp 83-98 Springer.

Köhler, C. (1986 b). Intrinsic connections of the retrohippocampal region in the rat brain. II. The medial entorhinal area. Journal of Comparative Neurology, 246(2), 149-169.

Köhler, C., Chan-Palay, V., & Steinbusch, H. (1981). The distribution and orientation of serotonin fibers in the entorhinal and other retrohippocampal areas. Anatomy and embryology, 161(3), 237-264.

Köhler, C., & Chan-Palay, V. (1982). The distribution of cholecystokinin-like immunoreactive neurons and nerve terminals in the retrohippocampal region in the rat and guinea pig. Journal of Comparative Neurology, 210(2), 136-146.

Köhler, C., Chan-Palay, V., & Wu, J. Y. (1984). Septal neurons containing glutamic acid decarboxylase immunoreactivity project to the hippocampal region in the rat brain. Anatomy and embryology, 169(1), 41-44.

Kubota, Y., Hattori, R., & Yui, Y. (1994). Three distinct subpopulations of GABAergic neurons in rat frontal agranular cortex. Brain research, 649(1), 159-173.

Levey, A. I., Edmunds, S. M., Hersch, S. M., Wiley, R. G., & Heilman, C. J. (1995). Light and electron microscopic study of m2 muscarinic acetylcholine receptor in the basal forebrain of the rat. Journal of Comparative Neurology, 351(3), 339-356

Lorente de No, R., Studies on the structure of the cerebral cortex. I. The area entorhinalis, J. Psychol. Neurol., 45 (1933) 381-438.

Lu, J., Jhou, T. C., & Saper, C. B. (2006). Identification of wake-active dopaminergic neurons in the ventral periaqueductal gray matter. The Journal of neuroscience, 26(1), 193-202

Manns, I. D., Mainville, L., & Jones, B. E. (2001). Evidence for glutamate, in addition to acetylcholine and GABA, neurotransmitter synthesis in basal forebrain neurons projecting to the entorhinal cortex. Neuroscience, 107(2), 249-263.

Mathisen, J. S. Blackstad Th.W. (1964). Cholinesterase in the hippocampal region. Cells Tissues Organs, 56(3), 216-253.

Miettinen, M., Pitkänen, A., & Miettinen, R. (1997). Distribution of calretinin-immunoreactivity in the rat entorhinal cortex: Coexistence with GABA. Journal of Comparative Neurology, 378(3), 363-378.

Mullen, R. J., Buck, C. R., & Smith, A. M. (1992). NeuN, a neuronal specific nuclear protein in vertebrates. Development, 116(1), 201-211

Nadasdy, Z., Varsanyi, P., & Zaborszky, L. (2010). Clustering of large cell populations: method and application to the basal forebrain cholinergic system. Journal of neuroscience methods, 194(1), 46-55.

Nishikawa, S., Goto, S., Hamasaki, T., Yamada, K., & Ushio, Y. (2002). Involvement of reelin and Cajal-Retzius cells in the developmental formation of vertical columnar structures in the cerebral cortex: evidence from the study of mouse presubicular cortex. Cerebral Cortex, 12(10), 1024-1030.

Pastoll, H., Solanka, L., van Rossum, M. C. & Nolan, M. F. 2013 Feedback inhibition enables ?-nested ? oscillations and grid firing fields. Neuron. 77, 141-54. doi: 10.1016/j.neuron.2012.11.032.

Paxinos G., Watson C., Carrive P., Kirkcaldie M., Ashwell K. (2009). Chemoarchitectonic Atlas of the Rat Brain, 2nd Edn San Diego, Elsevier Academic Press.

Peters A, Feldman ML (1976) The projection of the lateral geniculate nucleus to area 17 of the rat cerebral cortex. I. General description. J Neurocytol 5:63-84.

Peterson, D. A., Lucidi-Phillipi, C. A., Murphy, D. P., Ray, J., & Gage, F. H. (1996). Fibroblast growth factor-2 protects entorhinal layer II glutamatergic neurons from axotomy-induced death. Journal of Neuroscience, 16(3), 886-898.

Rouse, S. T., & Levey, A. L. (1996). Expression of m1-m4 muscarinic acetylcholine receptor immunoreactivity in septohippocampal neurons and other identified hippocampal afferents. Journal of Comparative Neurology, 375(3), 406-416.

Schmued LC. 1990. A rapid, sensitive histochemical stain for myelin in frozen brain sections. J. Histochem. Cytochem. 38: 717-720.

Schwaller, B., Dick, J., Dhoot, G., Carroll, S., Vrbova, G., Nicotera, P., ... & Celio, M. R. (1999). Prolonged contraction-relaxation cycle of fast-twitch muscles in parvalbumin knockout mice. American Journal of Physiology-Cell Physiology, 276(2), C395-C403.

Slomianka, L. (1992). Neurons of origin of zinc-containing pathways and the distribution of zinc-containing boutons in the hippocampal region of the rat. Neuroscience, 48(2), 325-352.

Slomianka, L., & Geneser, F. A. (1991). Distribution of acetylcholinesterase in the hippocampal region of the mouse: I. Entorhinal area, parasubiculum, retrosplenial area, and presubiculum. Journal of comparative neurology, 303(3), 339-354.

Slomianka, L., & Geneser, F. A. (1997). Postnatal development of zinc-containing cells and neuropil in the hippocampal region of the mouse. Hippocampus, 7(3), 321-340.

Somogyi, J., Baude, A., Omori, Y., Shimizu, H., Mestikawy, S. E., Fukaya, M., ... & Somogyi, P. (2004). GABAergic basket cells expressing cholecystokinin contain vesicular glutamate transporter type 3 (VGLUT3) in their synaptic terminals in hippocampus and isocortex of the rat. European Journal of Neuroscience, 19(3), 552-569.

Stensola, H., Stensola, T., Solstad, T., Frland, K., Moser, M. B., & Moser, E. I. (2012). The entorhinal grid map is discretized. Nature, 492(7427), 72-78.

Tsuji S. (1998) Electron microscopic localization of acetylcholinesterase activity in the central nervous system: chemical basis of a catalytic activity of Hatchett's brown (cupric ferrocyanide) precipitate revealed by 3,3?-diaminobenzidine. Folia Histochem Cytobiol. 36:67-70.

van Haeften, T., Baks-te-Bulte, L., Goede, P. H., Wouterlood, F. G., & Witter, M. P. (2003). Morphological and numerical analysis of synaptic interactions between neurons in deep and superficial layers of the entorhinal cortex of the rat. Hippocampus, 13(8), 943-952.

van Groen, T., & Wyss, J. M. (1990). The connections of presubiculum and parasubiculum in the rat. Brain research, 518(1), 227-243.

Van Strien, N. M., Cappaert, N. L. M., & Witter, M. P. (2009). The anatomy of memory: an interactive overview of the parahippocampal-hippocampal network. Nature Reviews Neuroscience, 10(4), 272-282.

Varga, C., Lee, S.Y. & Soltesz, I. 2010. Target-selective GABAergic control of entorhinal cortex output. Nat Neurosci. 13, 822-824.

Wang, Q., Gao, E., & Burkhalter, A. (2011). Gateways of ventral and dorsal streams in mouse visual cortex. The Journal of Neuroscience, 31(5), 1905-1918.

Witter, M. P., Groenewegen, H. J., Lopes da Silva, F. H., & Lohman, A. H. M. (1989). Functional organization of the extrinsic and intrinsic circuitry of the parahippocampal region. Progress in neurobiology, 33(3), 161-253.

Witter, M. P., & Moser, E. I. (2006). Spatial representation and the architecture of the entorhinal cortex. Trends in neurosciences, 29(12), 671-678.

Wong-Riley, M. (1979). Changes in the visual system of monocularly sutured or enucleated cats demonstrable with cytochrome oxidase histochemistry. Brain research, 171(1), 11-28.

Wouterlood, F. G., van Denderen, J., van Haeften, T., & Witter, M. P. (2000). Calretinin in the entorhinal cortex of the rat: Distribution, morphology, ultrastructure of neurons, and co-localization with ?-aminobutyric acid and parvalbumin. Journal of Comparative Neurology, 425(2), 177-192.

Wouterlood, F. G. 2002. "Spotlight on the neurones (I): cell types, local connectivity, microcircuits and distribution of markers," in The Parahippocampal Region: Organization and Role in cognitive Function, M. P. Witter and F. G. Wouterlood, Eds., pp. 61-88, Oxford University Press, Oxford, UK.

Wouterlood, F. G., van Haeften, T., Eijkhoudt, M., Baks-te-Bulte, L., Goede, P. H., & Witter, M. P. (2004). Input from the presubiculum to dendrites of layer-V neurons of the medial entorhinal cortex of the rat. Brain research, 1013(1), 1-12.

Wouterlood, F. G., Aliane, V., Boekel, A. J., Hur, E. E., Zaborszky, L., Barroso-Chinea, P., ... & Witter, M. P. (2008). Origin of calretinin-containing, vesicular glutamate transporter 2-coexpressing fiber terminals in the entorhinal cortex of the rat. Journal of Comparative Neurology, 506(2), 359-370.

Wyss, J. M., van Groen, T. & Sripanidkulchai K. 1990 Dendritic bundling in layer I of granular retrosplenial cortex: intracellular labeling and selectivity of innervation. J Comp Neurol. 295, 33-42.

Zaborszky, L. (2002). The modular organization of brain systems. Basal forebrain: the last frontier. Progress in brain research, 136, 359-372.

Zaborszky, L., van den Pol, A., & Gyengesi, E. (2012). The basal forebrain cholinergic projection system in mice. The Mouse Nervous System, 684-714. Watson, C., Paxinos, G., & Puelles, L. (Eds.). Elsevier.

Zimmermann, L. and Schwaller B (2002) Monoclonal antibodies recognizes epitopes of calretinin. Cell Calcium 31: 13-25

Chapter 6

General Discussion

Neurons are the fundamental building elements of the cerebral cortex. They are collectively organized into microcircuits, modules and cortical areas. Much of what we know about cortical function comes from studies at the single cell-level, where elementary (Hubel & Wiesel, 1959) and highly derived features (Gross et al., 1977; Quiroga et al., 2005) are encoded. At the same time the function of anatomically defined cortical modules or even entire cortical areas has remained elusive (Horton & Adams, 2005; da Costa & Martin, 2010). This may be due to the large number of possible interactions between cortical cells (Koch, 2012) and the lack of knowledge about cellular-level cortical connectivity (Denk et al., 2012). These obstacles may be overcome by studying simpler model animals and by developing novel technology to observe brain function at a large scale and with high resolving power (Laurent, 2006; Alivisatos et al., 2012).

In my doctoral thesis I studied the neurobiology and cortical structure of the Etruscan shrew - a new model animal for neurobiological research. In addition, I studied the modular structure of the entorhinal cortex of the rat as an example of cortical modular architecture. Both studies were initiated to provide an anatomical basis for studying structure-function relationships in the cerebral cortex. The small size of the Etruscan shrew's brain offers particular advantages for understanding cortical activity at the multi-cell level, both due to its small number of cortical neurons and its intrinsic advantages for optical imaging approaches. The entorhinal cortex contains both well-defined functional and anatomical modules and provides a unique opportunity for studying their interrelation.

In Chapter 2 we reviewed the behavior and neurobiology of the Etruscan shrew, *Suncus etruscus*, one of the smallest mammals and together with the star-nosed mole (Catania & Remple, 2005) also one of the fastest and most tactile hunters. Etruscan shrews show a wide range of fascinating social, exploratory and sophisticated prey-capture behaviors

(Anjum, 2010; Anjum & Brecht, 2012). When hunting, shrews tackle a complex task: in darkness they detect, overwhelm and kill their insect prey, a fast moving target that is almost as big as the shrew itself. A general characteristic of shrews is their elongated snout covered by a large array of whiskers which are rhythmically moved to explore the environment by touch. Removal experiments indicate that whiskers are required for hunting, and particularly for attack targeting (Anjum et al., 2006). Experiments with dummy prey objects showed that shrews attacked a plastic replica of a cricket but other similarly sized objects were ignored. Thus, tactile shape cues are both necessary and sufficient for evoking attacks and the visual and auditory sense are unlikely to play a major role in prey recognition. Several cortical areas comprising collectively about a third of the cortical volume respond to vibrissal touch which corresponds with the Etruscan shrews' behavioral specialization. One reason for their behavioral specialization may be their extraordinarily high energy turnover. The Etruscan shrews' large surface to volume ratio translates into the highest mass-specific oxygen consumption and metabolic rate of all mammals (Jürgens, 2007), a heart rate of over 1000 min^{-1} at rest and a breathing rate of 300 min^{-1} (Weibel et al., 1980). Etruscan shrews can enter a torpid state and reduce their body temperature which can cause an increase in cortical response latencies by two to three times, suggesting that endothermy is important for high-speed sensorimotor performance but cannot be maintained at all times. Only because Etruscan shrews are highly efficient hunters are they able to meet these extreme metabolic demands, which in turn pose important requirements on the organization of their specoes specific sensory world and brain structure. In Chapter 3 we studied the cortical organization of the Etruscan shrew. Because of its small size quantitative analysis of the Etruscan shrew cortex is more tractable than in other animals. One cortical hemisphere contains only about 1 million neurons which is on the order of the number of neurons found in some insect brains. Cytoarchitecture as well as histochemical and immunohistochemical staining revealed 13 cortical regions - a large number considering the small size of the shrew's brain and the possibility of further subdividing some of these regions into discrete cortical areas. Etruscan shrews actively use their whiskers for detecting prey. They are highly tactile animal with a large somatosensory cortex, which contains a barrel field, but barrels are much less clearly defined than in rodents. Barrels are present in a diverse set of species but only a small subset of species with whiskers has barrels and many species with clear cortical barrels do not show whisking behavior (Fox, 2008).

Similar difficulties in relating modular structure and function have been encountered in the rat entorhinal cortex which contains a small number of discrete functional units (Barry et al., 2007; Stensola et al., 2012) and a diversity of anatomical modules. Therefore, we aimed to provide common anatomical framework for medial entorhinal cortex

modularity based on pyramidal cell clusters. To relate the modular architecture to grid cell modules we proposed a model of pyramidal cell connectivity (Brecht et al., 2013). In the model, we suggest that the microcircuits underlying grid cell function are similar to other cortical circuits in two aspects: First, they share the abundant recurrent excitatory connections of most cortical microcircuits (DeFelipe & Jones, 2010). Second, we suggest that external space is topographically mapped onto the entorhinal cortex, much like the somatotopic mapping of the body surface in somatosensory cortex (Woolsey & Van der Loos, 1970; Catania et al., 1993). On the basis of these concepts, we studied in Chapter 4 how cortical modules are organized in layer 2 of medial entorhinal cortex. Microcircuit analysis of medial entorhinal cortex layer 2 has largely focused on stellate cells due to their intrinsic propensity for oscillatory activity (Alonso & Klink, 1993). In addition, stellate cells project to the hippocampus and interfering with their activity disrupts spatial memory formation (Yasuda & Mayford, 2006; Rowland et al., 2013). We focus on non-dentate-projecting, pyramidal cells marked by calbindin immunoreactivity that bundled their dendrites together and formed clusters arranged in regular array aligned to layer 1 axons and the parasubiculum. Clusters of calbindin positive cells showed a high degree of overlap with histochemical and immunohistochemical markers of cholinergic inputs. Cholinergic drive is an important component of theta-rhythmicity which we found to be two-fold stronger in pyramidal than in stellate neurons. Since nearly all grid cells are strongly theta modulated (Sargolini et al., 2006; Boccara et al., 2010) we suggest that pyramidal cells may play an important role in microcircuits for spatial navigation. In Chapter 5 we expand on these finding by showing the complementary distribution of reelin positive cells and differences in innervation by basket cells among principal cells in medial entorhinal cortex. Entorhinal cortex has been implicated as a key area in Alzheimer's disease (Hirano & Zimmerman, 1962; Braak & Braak 1991) with concurrent loss of modularity in the human brain (van Hoesen & Solodkin, 1993; Augustinack et al., 2013). Both cholinergic and zincergic neurotransmission have been implicated in Alzheimer's disease pathology (Coyle et al., 1983; Fredrickson et al., 2005). Therefore, our finding that cholinergic and zincergic inputs to rat medial entorhinal cortex are differentially distributed in relation to pyramidal cell clusters in layer 2 may be of interest for studying animal models of Alzheimer's disease.

In conclusion, we studied the areal architecture of the Etruscan shrew cortex and the modular architecture of the rat medial entorhinal cortex as a contribution towards understanding structure-function relations in the cerebral cortex.

6.1 References

Alivisatos, A. P., Chun, M., Church, G. M., Greenspan, R. J., Roukes, M. L., & Yuste, R. (2012). The brain activity map project and the challenge of functional connectomics. Neuron, 74(6), 970-974.

Alonso, A., & Klink, R. (1993). Differential electroresponsiveness of stellate and pyramidal-like cells of medial entorhinal cortex layer II. Journal of Neurophysiology, 70(1), 128-143.

Anjum, F., Turni, H., Mulder, P. G., van der Burg, J., & Brecht, M. (2006). Tactile guidance of prey capture in Etruscan shrews. Proceedings of the National Academy of Sciences, 103(44), 16544-16549.

Anjum, F. (2010). Tactile object recognition in the Etruscan shrew. Berlin, Humboldt-Univ., Diss.

Anjum, F., & Brecht, M. (2012). Tactile experience shapes prey-capture behavior in Etruscan shrews. Frontiers in behavioral neuroscience, 6.

Augustinack, J. C., Kouwe, A. J., & Fischl, B. (2013). Medial temporal cortices in ex vivo magnetic resonance imaging. Journal of Comparative Neurology, 521(18), 4177-4188.

Barry, C., Hayman, R., Burgess, N., & Jeffery, K. J. (2007). Experience-dependent rescaling of entorhinal grids. Nature neuroscience, 10(6), 682-684.

Boccara, C. N., Sargolini, F., Thoresen, V. H., Solstad, T., Witter, M. P., Moser, E. I., & Moser, M. B. (2010). Grid cells in pre-and parasubiculum. Nature neuroscience, 13(8), 987-994.

Braak, H., & Braak, E. (1991). Neuropathological stageing of Alzheimer-related changes. Acta neuropathologica, 82(4), 239-259.

Brecht M., Ray S., Burgalossi A., Tang Q., Schmidt H., & Naumann R., (2013). An isomorphic mapping hypothesis of the grid representation. Phil. Trans. R. Soc. B.

Catania, K. C., Northcutt, R. G., Kaas, J. H., & Beck, P. D. (1993). Nose stars and brain stripes. Nature, 364(6437), 493.

Catania, K. C., & Remple, F. E. (2005). Asymptotic prey profitability drives star-nosed moles to the foraging speed limit. Nature, 433(7025), 519-522.

Coyle, J. T., Price, D. L., & DeLong, M. R. (1983). Alzheimer's disease: a disorder of cortical cholinergic innervation. Science, 219(4589), 1184-1190.

da Costa, N. M., & Martin, K. A. (2010). Whose cortical column would that be?. Frontiers in neuroanatomy, 4.

DeFelipe, J., & Jones, E. G. (2010). Neocortical microcircuits. Handbook of Brain Microcircuits, 5-14.

Denk, W., Briggman, K. L., & Helmstaedter, M. (2012). Structural neurobiology: missing link to a mechanistic understanding of neural computation. Nature Reviews Neuroscience, 13(5), 351-358.

Frederickson, C. J., Koh, J. Y., & Bush, A. I. (2005). The neurobiology of zinc in health and disease. Nature Reviews Neuroscience, 6(6), 449-462.

Fox, K. (2008). Barrel Cortex. Cambridge University Press, Cambridge.

Gross, C. G., Bender, D. B., & Mishkin, M. (1977). Contributions of the corpus callosum and the anterior commissure to visual activation of inferior temporal neurons. Brain Research, 131(2), 227-239.

Hirano, A., & Zimmerman, H. M. (1962). Alzheimer's Neurofibrillary ChangesA Topographic Study. Archives of Neurology, 7(3), 227-242.

Horton, J. C., & Adams, D. L. (2005). The cortical column: a structure without a function. Philosophical Transactions of the Royal Society B: Biological Sciences, 360(1456), 837-862.

Hubel, D. H., & Wiesel, T. N. (1959). Receptive fields of single neurones in the cat's striate cortex. The Journal of physiology, 148(3), 574-591.

Jürgens K. D. (2007). Energy turnover and oxygen transport in the smallest mammal, the Etruscan shrew Suncus etruscus. In: Endothelial Biomedicine, 107-111. W.C. Aird (Ed.). Cambridge University Press.

Koch, C. (2012). Modular biological complexity. Science, 337(6094), 531-532.

Laurent, G. (2006). Shall we even understand the flys brain? In: 23 Problems in Systems Neuroscience, 3-21. van Hemmen, J. L., & Sejnowski, T. J. (Eds.). New York: Oxford University Press.

Quiroga, R. Q., Reddy, L., Kreiman, G., Koch, C., & Fried, I. (2005). Invariant visual representation by single neurons in the human brain. Nature, 435(7045), 1102-1107.

Rowland, D. C., Weible, A. P., Wickersham, I. R., Wu, H., Mayford, M., Witter, M. P., & Kentros, C. G. (2013). Transgenically Targeted Rabies Virus Demonstrates a Major

Monosynaptic Projection from Hippocampal Area CA2 to Medial Entorhinal Layer II Neurons. The Journal of Neuroscience, 33(37), 14889-14898.

Sargolini, F., Fyhn, M., Hafting, T., McNaughton, B. L., Witter, M. P., Moser, M. B., & Moser, E. I. (2006). Conjunctive representation of position, direction, and velocity in entorhinal cortex. Science, 312(5774), 758-762.

Stensola, H., Stensola, T., Solstad, T., Frland, K., Moser, M. B., & Moser, E. I. (2012). The entorhinal grid map is discretized. Nature, 492(7427), 72-78.

Van Hoesen, G. W., & Solodkin, A. (1993). Some modular features of temporal cortex in humans as revealed by pathological changes in Alzheimer's disease. Cerebral Cortex, 3(5), 465-475.

Weibel, E. R., Claassen, H., Gehr, P., Sehovic, S., & Burri, P. (1980). The respiratory system of the smallest mammal. In: Comparative physiology of primitive mammals, 181-191. Schmidt-Nielsen, K., Bolis, L. & Taylor, C. R. (Eds.). Cambridge University Press, Cambridge.

Woolsey, T. A., & Van der Loos, H. (1970). The structural organization of layer IV in the somatosensory region (SI) of mouse cerebral cortex: the description of a cortical field composed of discrete cytoarchitectonic units. Brain research, 17(2), 205-242.

Yasuda, M., & Mayford, M. R. (2006). CaMKII activation in the entorhinal cortex disrupts previously encoded spatial memory. Neuron, 50(2), 309-318.

Acknowledgements

First, I would like to thank my supervisor, Prof. Dr. Michael Brecht, for guiding me in my thesis work while at the same time allowing me to follow up on my own ideas. Thanks to his constant encouragement and critical discussions of my work I have learned about scientific inquiry as a creative and enjoyable process.

Special thanks go to Dr. Claudia Roth-Alpermann and Dr. Farzana Anjum with whom I was working together on the Etruscan shrew in my first years in the lab and to Susanne Grübel and Indra-Domenique Wrobel who kept a colony of hundreds of shrews alive and well. Brigitte Geue, Undine Schneeweiß and Juliane Steger provided excellent technical assistance and tolerated even the most arcane mixtures that I concocted in the lab.

Together with Helene Schmidt, Saikat Ray, Qiusong Tang and Dr. Andrea Burgalossi I worked on a number of projects in the second part of my thesis work. Working together in a large team was an enjoyable and rewarding experience. I would also like to thank everyone in the Brecht lab for valuable discussions and for help and advice in many situations.

During the course of my thesis I was fortunate to collaborate with a number of outstanding scientists. First, I would like to thank Dr. Jason Kerr (MPI Tübingen) for hosting me in his laboratory and giving me the opportunity to learn more about in-vivo calcium imaging. Also, I thank Dr. Paul Heppenstall (EMBL Monterotondo) for hosting me in his laboratory where I learned in-situ hybridization. I am grateful to Dr. Ruth Benavides-Piccione, Prof. Dr. Javier DeFelipe (both Instituto Cajal, Madrid) and Prof. Dr. Helmut Bartels (MH Hannover) who are working on understanding the ultrastructure of Etruscan shrew tissue. I would like to express my thanks to Dr. Liora Las and Prof. Dr. Nachum Ulanovsky (both Weizmann Institute) as well as Dr. Stephan Prokop and Prof. Dr. Frank Heppner (both Charité Berlin) for providing tissue samples.

Finally, I would like to thank the most important people in my life: my wife Dr. Hong Wang as well as my parents Dr. Jutta Naumann and Prof. Dr. Dr. Klaus-Dieter

Naumann for their constant support, patience and for always having time and interest in critically discussing my work.

Statement of Contribution

Some parts of my doctoral thesis have been conducted in a collaborative approach. In the following, please find a statement of the relative contributions to the data presented.

Chapter 2: I performed experiments on the peripheral anatomy of the Etruscan shrew and contributed to microelectrode mapping of the cerebral cortex.

Chapter 3: I performed all experiments and analysed the data.

Chapter 4: I contributed to experiments on anatomy of the entorhinal cortex and analysed the respective data.

Chapter 5: I performed all experiments and analysed the data.

In addition, and referring to all the chapters above, I designed experiments and contributed to writing the respective manuscripts.

Publications

Roth-Alpermann C, Anjum F, **Naumann R**, and Brecht M. *Cortical Organization in the Etruscan Shrew (Suncus etruscus).* J Neurophysiol. 2010 Nov;104(5):2389-406.

Brecht M, **Naumann R**, Anjum F, Wolfe J, Munz M, Mende C, and Roth-Alpermann C. *The neurobiology of Etruscan shrew active touch.* Philos Trans R Soc Lond B Biol Sci. 2011 Nov 12;366(1581):3026-36.

Naumann RK, Anjum F, Roth-Alpermann C, and Brecht M. *Cytoarchitecture, areas, and neuron numbers of the Etruscan shrew cortex.* J Comp. Neurol. 2012 Aug 1;520(11):2512-30. doi: 10.1002/cne.23053.

Brecht M, Ray S, Burgalossi A, Tang Q, Schmidt H and **Naumann R**. *An isomorphic mapping hypothesis of the grid representation.* 2013. Philos Trans R Soc Lond B Biol Sci.

Ray S*, **Naumann R***, Burgalossi A*, Tang Q*, Schmidt H and Brecht M. *Grid-like arrangement and theta-modulation of a pyramidal cell microcircuit in layer 2 of medial entorhinal cortex.* `(under review)`. * equal contribution

Naumann R*, Ray S*, Prokop S, Las L, Heppner F and Brecht M. *Conserved Size and Geometry of Pyramidal Patches in Layer 2 of Medial/Caudal Entorhinal Cortex.* `(in preparation)`. * equal contribution

Conference Contributions

Poster presentations

Naumann R, Anjum F, Roth-Alpermann C, and Brecht M. *Cytoarchitectonic mapping and quantitative anatomy of the Etruscan shrew cortex.* SfN Abstract, 2008.

Naumann RK, Kerr JND, Roth-Alpermann C, and Brecht M. *Translaminar imaging of calcium signals evoked by sensory stimuli in Etruscan shrew somatosensory cortex.* SfN Abstract, 2011.

Invited Talks

The neurobiology of Etruscan shrew active touch. Invited talk at conference: Think Alternative: Insights from Unconventional Model Organisms. Vienna Biocenter, Austria, 2011.

Translaminar imaging of calcium signals evoked by sensory stimuli in Etruscan shrew somatosensory cortex. Invited talk at conference: Cellular Mechanisms of Sensory Processing. MPI Gttingen, Germany, 2012.

Modular Organization of Layer II in the Medial Entorhinal Cortex. Invited talk at: NeuroCure CCO Seminar Series. Charité Berlin, Germany, 2013.

English summary

Neurons of the cerebral cortex are collectively organized into microcircuits, modules and cortical areas. In my doctoral thesis I studied the neurobiology and cortical structure of the Etruscan shrew - a new model animal for neurobiological research - and the modular structure of the entorhinal cortex of the rat. The small size of the Etruscan shrew's brain offers particular advantages for understanding cortical activity at the multi-cell level, both due to its small number of cortical neurons and its intrinsic advantages for optical imaging approaches. The entorhinal cortex contains both well-defined functional and anatomical modules and provides a unique opportunity for studying their interrelation.

In Chapter 2 study the behavior and neurobiology of the Etruscan shrew, *Suncus etruscus*, one of the smallest and fastest mammals. When hunting, shrews need to detect, overwhelm and kill their insect prey, a fast moving target that is almost as big as the shrew itself. Shrews have an elongated snout covered by a large array of whiskers which are rhythmically moved to explore the environment by touch. Behavioral experiments have shown that tactile shape cues are both necessary and sufficient for evoking attacks and the visual and auditory sense are unlikely to play a major role in prey recognition. We show in Chapter 3, that the organization of the cerebral cortex of the Etruscan shrew reflects this behavioral specialization. Several cortical areas comprising collectively about a third of the cortical volume respond to vibrissal touch. One cortical hemisphere contains only about 1 million neurons which is on the order of the number of neurons found in some insect brains. Cytoarchitecture as well as histochemical and immunohistochemical staining revealed 13 cortical regions - a large number considering the small size of the shrew's brain and the possibility of further subdividing some of these regions into discrete cortical areas.

Pyramidal cell clusters in layer 2 of medial entorhinal are easy and reliably identifiable and thus provide common anatomical framework for medial entorhinal cortex modularity. In Chapter 4 we study how cortical modules are organized in layer 2 of medial entorhinal cortex, in particular we focus on non-dentate-projecting pyramidal cells. These pyramidal cells form geometrically arranged clusters and bundle their dendrites towards

a common point overlapping with presynaptic markers of cholinergic inputs. Cholinergic drive is an important component of theta-rhythmicity which we found to be two-fold stronger in pyramidal than in stellate neurons. Since nearly all grid cells - an important functional cell type for spatial navigation - are strongly theta modulated we suggest that pyramidal cells may play an important role in microcircuits for spatial navigation. In Chapter 5 we investigate the spatial distribution of stellate cells and the differences in innervation by basket cells among the principal cells in medial entorhinal cortex. In this work, we studied the areal architecture of the Etruscan shrew cortex and the modular architecture of the rat medial entorhinal cortex as contributions towards understanding structure-function relations in the cerebral cortex.

Deutsche Zusammenfassung

Die Neurone der Hirnrinde sind in Mikroschaltkreisen, Modulen und Arealen organisiert. In dieser Doktorarbeit habe ich die Neurobiologie und Hirnrindenstruktur der Etruskerspitzmaus - ein neues Modelltier für neurobiologische Forschung - und die modulare Struktur des entorhinalen Cortex der Ratte untersucht. Die geringe Größe des Gehirns der Etruskerspitzmaus bietet besondere Vorteile für das Verständnis kortikaler Aktivität von Zellgruppen, sowohl aufgrund seiner geringen Anzahl von Neuronen als auch aufgrund der Vorteile kleiner Gehirne für mikroskopische Bildgebung. Die entorhinale Kortex enthält sowohl gut definierte funktionelle als auch anatomische Module und bietet daher eine einzigartige Gelegenheit für das Studium ihrer Wechselbeziehungen.

In Kapitel 2 untersuchen wir das Verhalten und die Neurobiologie der Etruskerspitzmaus, *Suncus etruscus*, eines der kleinsten und schnellsten Säugetiere. Bei der Jagd mussen Etruskerspitzmäuse Beuteinsekten überwältigen die fast ebenso groß wie die Spitzmause selbst sind. Spitzmäuse haben eine längliche Schnauze mit einer großen Anzahl Tasthaaren (Vibrissen), die rhythmisch bewegt werden, um die Umgebung zu erkunden. Verhaltensexperimente haben gezeigt, daß taktile Reize notwendig und hinreichend sind, um Beutefangverhalten auszulösen, während visuelle und auditorische Reize eine untergeordnete Rolle spielen. Wie in Kapitel 3 dargelegt, reflektiert Organisation der Hirnrinde diese Spezialisierung im Verhalten. Mehrere kortikale Regionen, die zusammen etwa ein Drittel des kortikalen Volumens ausmachen, reagieren auf taktile Reize. Eine kortikale Hemisphäre enthält nur etwa eine Million Neuronen, eine ähnliche Größenordnung wie die Anzahl von Neuronen im Gehirn einiger Insekten. Basierend auf der Zellarchitektur sowie histochemischen und immunhistochemischen Färbungen haben wir 13 kortikale Regionen definiert - eine große Zahl angesichts der geringen Größe des Spitzmausgehirns und der Möglichkeit einer weiteren Unterteilung einiger dieser Regionen in weitere kortikale Areale.

Pyramidenzellnester in Schicht 2 des medialen entorhinalen Kortex eignen sich als Bezugssystem für die verschiedenen anatomischen Module, da sie leicht und zuverlässig zu identifizieren sind. In Kapitel 4 wird die moduläre Struktur der Schicht 2 des medialen

entorhinalen Kortex untersucht, insbesondere die Pyramidenzellen in Schicht 2 des medialen entorhinalen Kortex, die nicht zum Hippocampus projizieren. Diese Pyramidenzellen formen geometrisch angeordnete Nester und bündeln ihre Dendritenbäume hin zu einem Punkt, der sich genau mit erhöhten Konzentrationen von präsynaptischen cholinergen Markern überschneidet. Cholinerge Transmission ist ein wichtiger Bestandteil des Theta-Rhythmus und unsere Ergebnisse zeigen, daß Pyramidenzellen im Vergleich zu Sternzellen doppelt so stark Theta-moduliert sind. Da fast alle Gitterzellen - ein wichtiger funktioneller Zelltyp für räumliche Navigation - stark Theta-moduliert sind, ist anzunehmen dass Pyramidenzellen eine wichtige Rolle in den Mikroschaltkreisen für räumlichen Navigation spielen. In Kapitel 5 untersuchen wir die räumliche Verteilung der Sternzellen im entorhinalen Kortex sowie die Unterschiede zwischen Pyramidenzellen und Sternzellen in ihrer Verschaltung mit Korbzellen. In dieser Arbeit wurden an der Hirnrinde der Etruskerspitzmaus sowie der entorhinalen Hirnrinde der Ratte modellhaft Struktur-Funktions-Beziehungen in der Großhirnrinde aufgeklärt.

Eigenständigkeitserklärung

Hiermit versichere ich, dass ich die vorliegende Arbeit selbständig verfasst und keine anderen als die angegebenen Quellen und Hilfsmittel verwendet habe. Ich erkläre, dass ich sämtliche in der oben genannten Arbeit verwendeten fremden Quellen als solche kenntlich gemacht habe und gemäß den mir bekannten gängigen wissenschaftlichen Regeln korrekt zitiert habe. Ich bestätige, daß ich bei wörtlich übernommenen Aussagen bzw. bei unverändert übernommenen Grafiken als auch bei in eigenen Worten wiedergegebenen Aussagen bzw. von mir abgewandelten Grafiken anderer Autoren die Quelle angegeben habe. Ein Teil der beschriebenen Ergebnisse wurde in Kooperation mit anderen Mitarbeitern der Arbeitsgruppe von Prof. Dr. Brecht erzielt und ist als solches gekennzeichnet. Ich habe diese Arbeit nicht anderwertig zu Prüfungszwecken vorgelegt. Die dem Promotionsverfahren zugrunde liegende Promotionsordnung ist mir bekannt.

Unterschrift: _____

Datum: _____